STUDIA UNIVERSITATIS
BABEŞ-BOLYAI

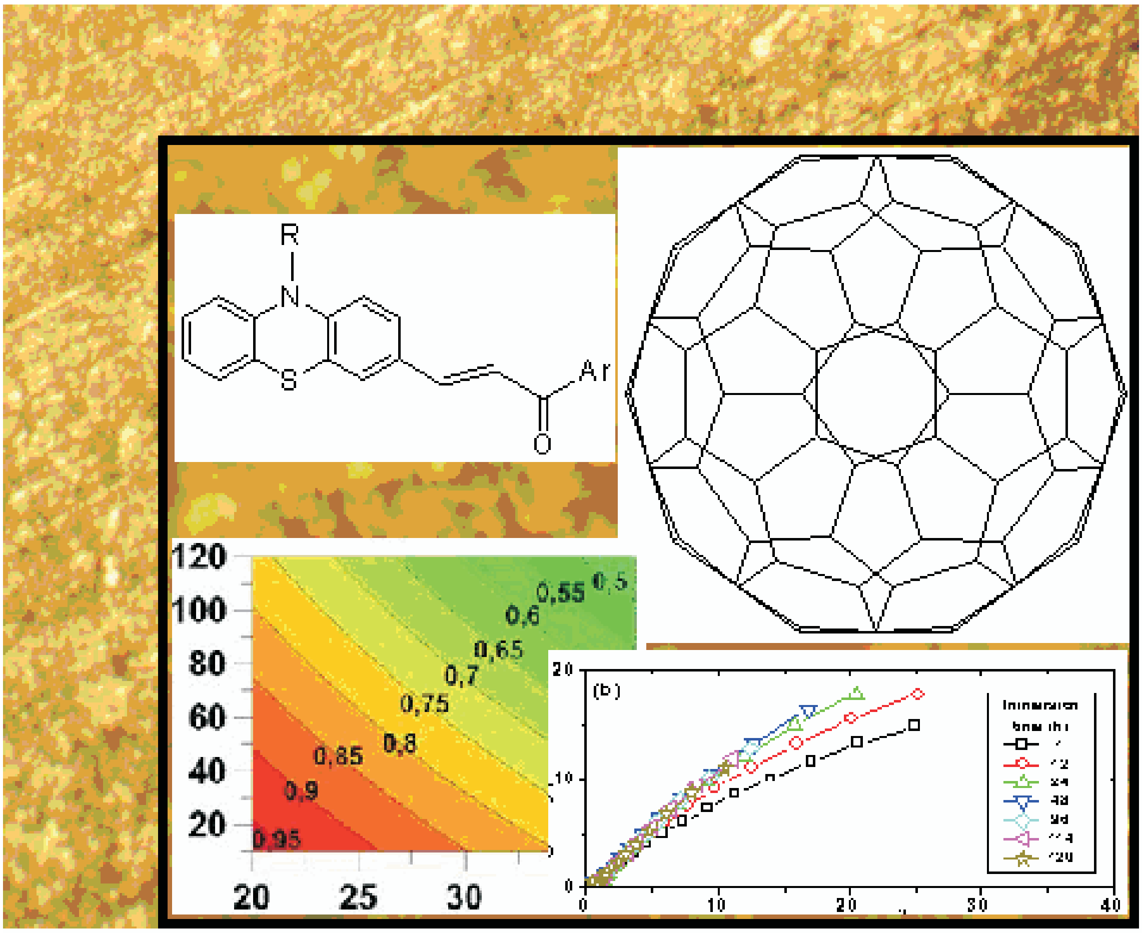

CHEMIA

2/2009

ANUL LIV 2009

STUDIA

UNIVERSITATIS BABEŞ-BOLYAI

CHEMIA

2

Desktop Editing Office: 51ST B.P. Hasdeu Street, Cluj-Napoca, Romania, Phone + 40 264-405352

CUPRINS – CONTENT – SOMMAIRE – INHALT

JOSEPH SHERMA, Bioluminescence Detection in Thin Layer Chromatography......... 5

IOAN PANEA, MIRELA PELEA, MARIA COROŞ, LUMINIȚA SILAGHI-DUMITRESCU, IOAN BÂLDEA, The Comparative Study of the Influences of the External Factors on the UV-Vis Absorption Spectra of Some Potentially Tautomeric Azocoupling Products 15

ADRIAN-RAUL TOMŞA, DANIELA CIOLOBOC, ANA-MARIA TODEA, LAURA MUREŞAN, VIOLETA PAŞCALĂU, MARIANA RUSU, Synthesis and Characterization of a Sandwich-Type Cerium (iv) Complex Derived from Monolacunary Dawson 2-molybdo-15-tungsto-2-phosphate 33

LAURIAN VLASE, DANA MUNTEAN, SORIN E. LEUCUȚA, IOAN BÂLDEA, High-Throughput Determination of Ivabradine from Human Plasma by LC/MS/MS and its Application to Pharmacokinetic Studies....................................43

D. MANCIULA, S. GRÄTER, T. BUREK, I.O. MARIAN, B.R.H. MIŞCA, Nano- and Microparticle Distribution on Solid and Flexible Substrates – Part II............. 53

STEFANIA TOTOS, IOAN OPREAN, MONICA BUCSA, Application of the Ruthenium-Catalyzed Oxidative Cleavage of Olefins to the Aldehides in the Syntheis of (S)-14-methyl-1-octadecene, the Sex Pheromone of *Lyonetia clerkella*... 61

LUIZA GĂINĂ, MIHAI SURDUCAN, CASTELIA CRISTEA, LUMINIȚA SILAGHI-DUMITRESCU, Microwave-Assisted Synthesis of Phenothiazine Sulfoxide Derivatives 65

SIMONA VARVARA, MARIA POPA, GABRIEL RUSTOIU, ROXANA BOSTAN, LIANA MUREŞAN, Evaluation of some Amino Acids as Bronze Corrosion Inhibitors in Aqueous Solution 73

RADU BANICA, NICOLAE VASZILCSIN, TEREZIA NYARI, GEZA BANDUR, Study on the Electrodeposition of Molybdenum Oxides on Copper Support 87

CERASELLA INDOLEAN, LUIZA GĂINĂ, MAJDIK CORNELIA, *N*-alkylation of Acridone by Means of Microwave Irradiations Without Solvent 95

LILIANA TEODOROF, CRISTINA NASTASE, IRINA ANUTI, The Study of Heavy Metals Transfer Factors on Different Types of Aquatic Vegetation 99

ELEONORA MARIA RUS, CRISTIAN CALIN, IOAN BALDEA, Investigation of Underground Gas Pipelines Corrosion by Optical and X-rays Diffraction Methods 111

ANTON A. KISS, ALEXANDRE C. DIMIAN, PIET D. IEDEMA, Don’t Gamble with Physical Properties of Polymers 121

MARIUS SEBASTIAN SECULA, RODICA DIACONESCU, STELIAN PETRESCU, Screening and Response Surface Modeling of Water Vapor Adsorption from Wet Air in Packed Bed of Silica Gel Using D-Optimal Design 133

MARYAM JALALI, MODJTABA GHORBANI, Counting Numbers of Permutational Isomers of an Infinite Family of Fullerenes 145

Studia Universitatis Babes-Bolyai Chemia has been selected for coverage in Thomson Reuters products and custom information services. Beginning with V. 53 (1) 2008, this publication is indexed and abstracted in the following:

- Science Citation Index Expanded (also known as SciSearch®)
- Chemistry Citation Index®
- Journal Citation Reports/Science Edition

STUDIA UNIVERSITATIS BABEŞ-BOLYAI, CHEMIA, LIV, 2, 2009

BIOLUMINESCENCE DETECTION IN THIN LAYER CHROMATOGRAPHY

JOSEPH SHERMA[a]

ABSTRACT. The principles, techniques, advantages, and applications of toxicity screening of complex mixtures using bioluminescent bacteria such as *Vibrio fischeri* following separation on a thin layer chromatography or high performance thin layer chromatograpy plate are described. A commercial kit, Bioluminex, and detection device, BioLuminex, are available for the method.

Keywords: *thin layer chromatography, TLC, bioluminescence detection, Vibrio fisheri, Bioluminex, BioLuminizer*

INTRODUCTION

Physical, chemical, and biological or bioactivity-based methods are used to detect zones in thin layer chromatography (TLC) after development of the plate with the mobile phase [1]. Advantages of TLC combined with a bioassay are high specificity and reduced interference of the matrix, leading to less need for sample cleanup [2]; high sensitivity, with detection limits typically in the sub-ng to pg range; identification of separated toxic compounds, degradation products, and metabolites based on chromatographic retention (R_f values), physical detection, and specific biological activity related to the test system; and opportunity for quantitative analysis.

Biological detection methods for microbiologically active compounds have been classified as diffusion methods, dilution methods, and bioautography [3]. The principle of direct bioautography is that a suspension of a microorganism growing in a suitable medium is applied to a developed TLC plate after drying; incubation of the plate with the microbes at optimum humidity and temperature allows growth of the bacteria and, by use of a specific dye, live cells can be visualized because, e.g., dehydrogenases from living microorganisms convert a tetrazolium salt into intensely colored formazan [4]. This article will be limited to a description of TLC in combination with bioluminescence detection, in which antibacterial compounds are detected as dark zones against a luminescent layer background instead of as colorless zones against a colored layer

---

[a] *Department of Chemistry, Lafayette College, Easton, PA 18042-1782, shermaj@lafayette.edu*

background in bioautography. Bioluminescence-TLC is being increasingly used because of the commercial availability of a reagent kit, detection device, and supporting accessory instruments to standardize the method and provide the optimum results.

PRINCIPLES OF TLC-BIOLUMINESCENCE COUPLING

The technology for bioactivity screening by TLC-bioluminescence direct coupling was developed by Bayer AG (Leverkusen, Germany) and published in 1996 [5]. The method is based on the change in emission by luminescent microorganisms in the presence of bioactive substances, which provides an effective way to detect toxic compounds on a TLC plate. The combination of TLC separation technology with the biospecific sensing ability of living cells represents a novel screening tool for targeting bioactive compounds in complex samples. In the published study [5], the TLC-bioluminescence technique proved to be superior to a high performance column liquid chromatography (HPLC)-bioluminescence method.

After TLC separation and evaporation of the mobile phase, the plate is coated with a bioluminescent solution of the nonpathogenic marine organism *Vibrio fischeri* by dipping. *V. fischeri* emits light as a product of cellular respiration. As *V. fischeri* cells reach a critical cellular density, the bioluminescence catalyst, luciferase, is expressed. Luciferase, in the presence of oxygen, catalyzes an oxidation reaction that releases excess energy in the form of light. Toxic substances on the layer are selectively identified as dark zones (inhibited bacteria) on a luminescent background (viable bacteria). The degree of toxicity is proportional to the luminescence inhibition. The results occur within seconds and last until the plate dries. Results can be documented by imaging with a charge coupled device (CCD) camera inside of a dark box or by X-ray film. The detection result of bioluminescence is similar to classical fluorescence quenching detection in which compounds that contain aromatic rings or multiple bonds absorb 254 nm light from an ultraviolet (UV) source and appear as dark zones against a bright background when layers impregnated with a fluorescent phosphor (F_{254} layers) are used. Because a TLC plate is used only once, less purified samples can be tolerated compared with column chromatography, in which strongly retained impurities from a previous sample can be eluted and interfere with later samples injected onto the column.

HPTLC- BIOLUMINESCENCE WITH THE BIOLUMINIZER

In modern TLC-bioluminescence analysis, a high performance TLC (HPTLC) plate is used instead of a TLC plate in order to achieve greater resolution and speed. The sample is separated by HPTLC, and the plate is subsequently immersed in the luminescent bacterial suspension (*V. fischeri*; Bioluminex assay kit from ChromaDex, Irvine, CA). After an incubation time for completion of the reaction, all zones with inhibitory or toxic effects appear black and those with stimulatory effect as lighter zones in the chromatograms on the plate, which is photographed by the Camag (Muttenz, Switzerland) BioLuminizer (Figure 1), a light-tight dark box imaging system employing a high resolution cooled CCD camera with 16 bit data acquisition carried out for a specified time period. The BioLuminizer was developed specifically to accumulate the light signal from HPTLC plates for bioluminescent-based effect-directed analysis (EDA); there is no lighting system in the BioLuminizer, and the image is only acquired from the luminescence zones on the plate. The camera is optimized for long exposure times and very little light (high efficiency, low readout noise, and low dark current due to active cooling). Digital chromatogram images produced with the BioLuminizer can be quantitatively evaluated by VideoScan software. The BioLuminizer has a holder that enables exact plate positioning (to 0.1 mm) and an optimized compartment that resists plate dryout and keeps the bacteria moist and luminescent for several hours, leading to predictable bioluminescence activity for consistent results. High quantum efficiency up to 65% allows short exposure times.

Figure 1. Bioluminizer detection system for bioactive compounds. Photograph supplied by Camag, Muttenz, Switzerland

EDA combining HPTLC with direct bioluminescence is a practical alternative to complex target analysis and provides a fast, low cost means of demonstrating biological activity in cases where many unknown substances are present, such as environmental samples. The time and effort required to examine structures or isolate substances can be restricted to a few relevant substances. By using HPTLC to separate the test sample into individual substances, the possibility of antagonistic effects or interferences leading to false results that can occur with classic cuvet tests (DIN 38412 L34) are eliminated. Detection levels are typically in the picomole range. Inhibition values can be determined by special software for quantification of luminescence inhibition. In addition to bioluminescent bacteria, HPTLC-EDA has been proven effective for other types of bioassays, such as acetylcholinesterase inhibition, penicillin, and *Bacillus subtilis*, as well as genotoxicity tests such as umu (*Salmonella thyphimurium*) and yeast estrogen screen (YES).

The plate is typically dipped for 2 s into the luminescent bacteria in the Bioluminex assay. Instead of manual dipping, this step can be carried out more reproducibly using the Camag Chromatogram Immersion Device or Desaga TLC Dip-Fix (Desaga products are supplied by Sarstedt, Inc., Newton, NC) [6], which offer uniform vertical speed of immersion and withdrawal for selectable time periods. The dipping devices are also useful for prewashing the HPTLC plates to remove layer impurities before sample application. For highest resolution, samples can be applied bandwise with an automated instrument such as the Camag Linomat 5, Camag Automatic TLC Sampler, or Desaga HPTLC-Applicator AS 30 [7]. Ascending chromatogram development is usually carried out in a traditional rectangular glass chamber (N-chamber) or Camag twin trough chamber with a wedge shaped ridge along the bottom [8], but improved reproducibility can be obtained by using the Camag Automatic Developing Chamber ADC2 or Desaga TLC-MAT automatic chamber [6], which control chromatographic conditions such as saturation, layer activity, and drying. The highest resolution separations can be performed by automated multiple development (AMD) with the Camag AMD2 using a mobile phase gradient of decreasing elution strength over increasingly longer development distances with drying between steps [9]. Chromatograms can be photographed under white light (colored zones detected), 254 nm (fluorescence quenched zones), or 366 nm UV light (fluorescent zones) using a Desaga Digital Documentation System DD 50, ChromaDoc-IT Imaging System (Analtech, Newark, DE), or Camag Digistore-2 Documentation System (now replaced by the TLC Visualizer) [6]. The zones on plates can be quantified based on their scan areas compared to standard zones measured with a slit scanning densitometer (Camag TLC Scanner 3 or Desaga CD 60) [6, 10] or a diode array scanner (Tidas TLC 2010; J&M, Aalen, Germany), or by using image analysis software available with a Camag videodensitometer, the three documentation systems mentioned above, or a flatbed scanner densitometer (Chromimage; AR2i, Le Plessis Robinson, France). These accessory instruments improve the methodology and complement the analytical information generated by the BioLuminizer.

APPLICATIONS OF TLC- BIOLUMINESCENCE ANALYSIS

Application areas suggested by ChromaDex on its website [11] are natural biological and chemical toxins, chemical contaminants and pollutants, identification of potential biological activity (antimicrobiological screening), raw material identity testing, simultaneous chemical and biological profiling, simultaneous parallel processing of up to 22 samples, and qualitative and quantitative analysis. Specific applications offered on the ChromaDex website are mycotoxin in corn; strychnine in infant formula; carbaryl insecticide in wine; fingerprint of *Capsicum annum* in cayenne; and steroid, As(III), and the herbicide metolachlor in tap water. For these applications, images of chromatograms are presented by ChromaDex.

Applications of the Bioluminex assay in a published article by scientists at the ChromaDex laboratories [12] include detection of the illicit bulking agent melamine in pet food; fingerprint comparison of fresh versus cured tobacco [methanol extraction of tobacco products and silica gel TLC with chloroform-methanol-ammonium hydroxide (9:1:0.05) mobile phase]; screening for compounds with biological activity in methanol extracts of Asian red yeast rice [chloroform-ethyl formate-formic acid-methanol (5:5:2:2) mobile phase]; structure-activity relationship (SAR) analysis of the structurally similar compounds quercetin, isoquercetin, and quercetin-3-rutinoside; and detection of ochratoxin in canned corn, aflatoxin B1 in honey, digoxin in milk, benzopyrine in celery seed, capsaicin in cayenne pepper, strychnine or monofluoroacetic acid in various drinks, domoic acid in soda, and patulin in apple juice.

Applications of TLC-bioluminescence described on the Bayer website [13] are toxicity profiling of wastewater over a 15 day period, analysis of natural products extracts, detection of tea seed oil residual, quantification of toxicity by toxicity equivalents based on calibration with 4-nitrophenol, United States Pharmacopeia (USP) method for *Matricaria chamomilla* using bioluminescence and anisaldehyde/366 nm detection, analysis of kava kava, and toxicity in process water.

Specific applications for the HPTLC-BioLuminizer method offered on the Camag website [14] are the following: analysis of wastewater containing X-ray contrast media for oxidation products produced by irradiation with UV light; toxicity screening for environmental applications; risk assessment and monitoring of drinking water, wastewater, and natural attenuation processes; detection of toxins and chemical adulterants in foodstuffs, beverages, and cosmetics; identification of biological activity in natural product extracts; determination of pesticides, heavy metals, organic pollutants, pharmaceuticals, and mycotoxins in a variety of complex matrices; and bioactivity-based analysis of irradiated sunscreens.

The determination of berberine containing drugs in methanol extracts of powdered raw material is illustrated in Figure 2 and 3. Additional compounds are detected after HPTLC by bioluminescence compared to fluorescence under 366 nm UV light.

Luminographic detection of toxins and pollutants in raw water and drinking water was performed with the Bioluminex-Bioluminizer system [15]. Analytes were recovered from water samples using Isolute ENV+ solid phase extraction (SPE) with methanol eluent, 20 x 10 cm silica gel $60F_{254}$ HPTLC plates, application of samples as bands with an Automatic TLC Sampler, and chromatography with an AMD2 using a 25 step gradient based on acetonitrile-formic acid-dichloromethane with a maximum developing distance of 80 mm.

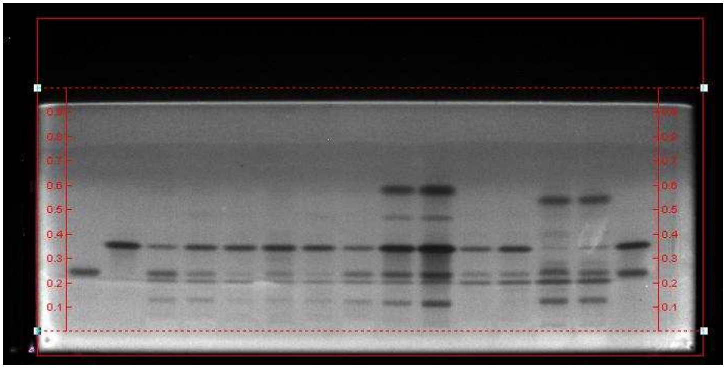

Figure 2. Detection of berberine alkaloids by their green to yellow fluorescence under 366 nm UV light using a Digistore-2 Documentation System and by the BioLuminex assay. Lane numbers: 1, palmatine; 2, berberine; 3-8, Mahonia sp.; 9-10, Coptis chinensis; 11-12, Phellodendron chinensis; 13-14, tinospora sp.; 15, palmatine plus berberine. Chromatographic conditions: HPTLC silica gel 60F254 Merck plate, toluene-ethyl acetate-methanol-isopropanol-water (60:30:20:15:3) mobile phase, 1 uL test and standard solutions applied as 8 mm bands, development in a twin trough chamber saturated with ammonia vapor. Photograph supplied by Camag, Muttenz, Switzerland

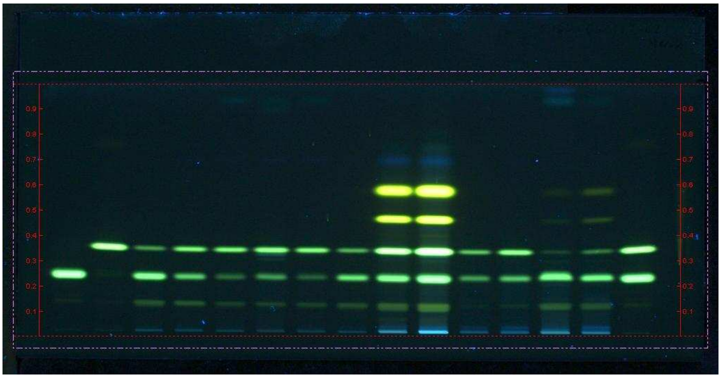

Figure 3. HPTLC bioluminescence image of the same plate as in Figure 2. Note the different numbers of zones in the chromatograms detected in some of the lanes by the two methods to provide complementary information on the samples. Photograph supplied by Camag, Muttenz, Switzerland

Similar methods were used to compare the bioactivity of several types of sports field granules and of expressway wastewater and landfill leachate [16]. In this study, the AMD gradient had 13 steps based on methanol (containing 5% ammonia), dichloromethane, and *n*-hexane.

HPTLC was coupled with bioluminescence and mass spectrometry (MS) for bioactivity based analysis of secondary metabolites in marine sponges [17]. Lyophilized and ground sponge tissue was extracted overnight with methanol, and the extract was evaporated and redissolved for analysis. HPTLC silica gel $60F_{254}$ plates and bandwise application of samples using an Automatic TLC Sampler were used. A 15 step gradient, with 3 mm increments, based on methanol, dichloromethane, and *n*-hexane was used for development. Optional derivatization with sulfuric acid reagent and Bioluminex detection with *V. fischeri* were done using a Chromatogram Immersion Device III, and documentation was with a DigiStore 2. Zones of interest were identified by online Fourier transform (FT) MS.

For analysis of sunscreens irradiated with either artificial light or sunlight, samples were applied with a Linomat 5 onto a LiChrospher Si $60F_{254}$ HPTLC plate; separated by AMD (six steps with diisopropyl ether-*n*-hexane, drying time between steps 2-3 min, migration distance 50 mm); documented under 254 and 366 nm UV light; scanned at 200-400 nm with a TLC Scanner 3 and WinCats software; and detected with *V. fischeri*. Zones of special interest were scratched out of the layer and reanalyzed by HPLC with a diode array detector and HPLC/MS [18]. Bioluminescence detection allowed location of zones of compounds undetected by physical or chemical methods and identified bioactive photodegradation products that need further toxicological evaluation.

Adulteration of black cohosh (Actaea racemosa) was determined by HPTLC-bioluminescence performed as follows: sonication extraction of powdered plant material with methanol, application of samples with an Automated TLC Sampler 4 as bands to a silica gel $60F_{254}$ HPTLC plate, plate development with toluene-ethyl formate-formic acid (5:3:3) in a saturated ridged bottom glass chamber, zone detection under 254 and 366 nm UV light and by spraying with sulfuric acid-anisaldehyde reagent and heating (125^{o}C, 5 min), and bioactivity detection with the Bioluminex/BioLuminizer system. Yellow cohosh and other common adulterants were readily differentiated from black cohosh [19].

Additional biologically active compounds and samples that have been analyzed by TLC-*V. fischeri* bioluminescence coupling include 3,5-dichlorophenol [20]; 4-nitrophenol in urine, and garlic and curry food ingredients [21]; the cytostatic agent avarone, with subsequent confirmation by MS [22]; toxic methylmercury and the banned pesticide *o*,*p*-dichlorodiphenyldichloroethane (DDD) [23]; organic compounds in tannery effluent and molasses wastewaters

(AMD-TLC fractionation) [24]; and pentachlorophenol (graph of inhibition versus concentration was nearly linear in the range of 20-80 ng with densitometer and videodensitometer measurement) [25].

CONCLUSIONS

TLC or HPTLC combined with bioluminescence detection is an important method for effect directed analysis of bioactive zones on the layer. Bioluminescent bacteria can be used, or other types of bioassays can be carried out [26]. A system incorporating *V. fischeri*, HPTLC, and detection with a CCD camera in a dark box (BioLuminizer) is available from Camag. Various accessory HPTLC instruments can be incorporated to obtain improved results and additional analytical information. Key advantages are that tedious single compound screening is avoided, rapid response time and fast results, no false results due to antagonistic effects/interferences, detection in the picomole range, high sample throughput due to parallel analysis of multiple samples on one plate, low cost, and possibility of further investigation of bioactive zones, e.g., by MS. Use of online HPTLC/MS to obtain information about bioactive unknowns is now greatly facilitated by the availability of a commercial interface that can be connected to any HPLC-coupled mass spectrometer and gives direct extraction of zones from the plate into the ion source [27].

REFERENCES

1. J. Sherma, “Encyclopedia of Chromatography”, 01 June 2005, DOI:10.1081/E-ECHR-120039952.
2. J. Sherma, “Encyclopedia of Chromatography”, 23 April 2007, DOI:10.1081/E-ECHR-120042973.
3. L. Botz, S. Nagy, B. Kocsis, “Planar Chromatography-A Retrospective for the Third Millennium”, Springer Scientific Publisher, Budapest, Hungary, **2001**, chapter: Detection of microbiologically active compounds.
4. E. Tyihak, E. Mincsovics, G. Katay, Z. Kiraly-Veghely, A. M. Moricz, P. G. Ott, *J. Planar Chromatogr.-Mod. TLC*, **2008**, *21*, 15.
5. G. Eberz, H. G. Rast, K. Burger, W. Kreiss, C. Weisemann, *Chromatographia*, **1996**, *43*, 5.
6. J. Sherma, *J. AOAC Int*., **2008**, *91*, 51A.

7. J. Sherma, “Encyclopedia of Chromatography”, 15 August 2006, DOI:10.1081/E-ECHR-120042942.
8. S. M. Verbitski, G. T. Gourdin, L. M. Ikenouye, J. D. McChesney, *Amer. Biotechnol. Lab*. **2006** *24*(9), 40.
9. J. Sherma, *J. AOAC Int*. **1992**, *75*, 15.
10. J. Sherma, “Encyclopedia of Chromatography”, 01 June 2005, DOI:10.1081/E-ECHR-120040068.
11. <http://www.chromadex.com>
12. L. Ikenouye, S. Hickey, S. Verbitski, G. Gourdin, *Camag Bibliography Service (CBS)*, **2007**, *99*, 11.
13. <http://www.hptlc.com/berlin/2006pdf/pdf11am/HPTLC_2006_kreiss.pdf>
14. <http://www.camag.ch>
15. W. Weber, W. Seitz, A. Aichinger, R. Albert, *Camag Bibliography Service (CBS)*, **2005**, *94*, 1.
16. W. Schulz, W. Seitz, S. C. Weiss, W. H. Weber, M. Boehm, D. Flottmann, *J. Planar Chromatogr.-Mod. TLC*, **2008**, *21*, 427.
17. A. Kloeppel, W. Grasse, F. Bruemmer, G. E. Morlock, *J. Planar Chromatogr.-Mod. TLC*, **2008**, *21*, 431.
18. U. Hauri, V. Baumgartner, C. Hohl, *Camag Bibliography Service (CBS)*, **2008**, *100*, 2.
19. S. Verbitski, G.T. Gourdin, L. M. Ikenouye, J. D.McChesney, J. Hildreth, *J. AOAC Int*. **2008**, *91*, 268.
20. G. Eberz, H. G. Rast, K. Burger, W. Kreiss, *Biolog. Abwasser*., **1997**, *8*, 45.
21. F. G. Kern, *Bioforum*, **1997**, *20*, 18.
22. G. E. Morlock, W. Schwack, *LabCiencia con Noticias Technicas del Laboratorio*, **2008**, *16*, 7.
23. S. M. Verbitski, G. Gourdin, L. Ikenoye, J. McChesney, *Preprints of Extended Abstracts presented at the ACS National Meeting*, American Chemical Society, Environmental Chemistry, **2005**, *45*, 180.
24. T. Reemtsma, A. Putschew, M. Jekel, *Vom Wasser*, **1999**, *92*, 243.
25. C. Weins, H. Jork, *J. Chromatogr. A*, **1996**, *750*, 403.
26. S. Weins, *J. Planar Chromatogr.-Mod. TLC*, **2008**, *21*, 405.
27. <http://www.camag.com/tlc-ms>

STUDIA UNIVERSITATIS BABEŞ-BOLYAI, CHEMIA, LIV, 2, 2009

THE COMPARATIVE STUDY OF THE INFLUENCES OF THE EXTERNAL FACTORS ON THE UV-VIS ABSORPTION SPECTRA OF SOME POTENTIALLY TAUTOMERIC AZOCOUPLING PRODUCTS

IOAN PANEA, MIRELA PELEA, MARIA COROŞ,
LUMINIȚA SILAGHI-DUMITRESCU, IOAN BÂLDEA[a]

ABSTRACT. The influences of the pH', water content, sample concentration, temperature and time on the UV-Vis absorption spectra of four potentially tautomeric azocoupling products **1**- **4** have been comparatively studied in ethanol-water mixtures. The pH' influence can be explained by the involvement in two steps deprotonation equilibria of each dye **1**- **4**. These equilibria are characterized by the $pK_a^{'}$ values. The three species involved in the two deprotonation steps of each dye **1**- **4** exhibit different visible absorption maxima. The hydrazone structures **1b**- **4b** of the initial neutral species of the dyes are supported by IR and ^{1}H-NMR data. The presence of other tautomeric forms (*e.g.* **1a- 4a**) has been not proved. The comparative study of the effect of other external factors on the spectra with that of pH' has shown that: i)- the influence of either water content, sample concentration or temperature, which is characterized by the presence of isosbestic points, may be explained by the involvement of the dyes in the first step acid ionization; ii)- the influence of either water content, sample concentration, temperature or time, when isosbestic points do not appear, might be explained by the superposition of the acid ionization equilibrium of the dyes with other phenomena. Thus, to account for the effect of water content and time on the spectra of the dye **1,** the superposition of a disaggregation process and acid ionization equilibrium has been assumed.

Keywords: *azacoupling products, UV-Vis spectra of azacoupling products*

INTRODUCTION

The azocoupling products having hydroxyl groups conjugated with the azo linkage from their potentially azo tautomer might be involved in azo-hydrazone [1a, 2-11], acid-base [1a, 2, 8, 9, 11-19] or/and aggregation [1b, 3, 9-11, 14, 20-30] equilibria. All these equilibria are influenced by the structure

---

[a] *Department of Chemistry and Chemical Engineering, "Babeş-Bolyai" University of Cluj. 11 Arany Janos Str., Cluj-Napoca, RO-400028, Romania*

of the azocoupling products [1a, 2, 8, 9, 11-13, 16-19, 22, 27, 28, 31-34] and by external factors [1a-c, 2, 3, 6, 8-28, 30-45]. Because the forms involved in the possible equilibria have different chemical structures they might differ also in colour [1a, 1c, 2, 3, 12a, 30]. Therefore the factors that influence the equilibria might change the colour. Such a colour change has consequence on the application possibilities of the azocoupling products [1a, 1c, 2]. Therefore the study of the influence of different factors on the UV-Vis absorption spectra of the azocoupling products has a practical significance [1a-c, 2, 12a, 31, 32, 37-39]. On the other hand, it has been studied the influences of the various factors on the UV-Vis spectra of the azocoupling products in order to establish the nature of the equilibria exhibited by dyes [1b, 2, 3, 6, 8-26, 28-37, 40-45]. In a study using UV-Vis spectrophotometry, the certain criterion for the existence of an equilibrium is the occurrence of isosbestic points on the recorded spectra under various values of investigated factor [1b, 2, 8, 9, 11-14, 17-19, 22-26, 41-45]. In exchange, the criterion to find out the nature of the equilibrium involved is more or less certain. Thus, the criterion for the acid-base nature of the equilibrium is the occurrence of isosbestic points on the UV-Vis absorption spectra recorded with several isomolar solutions of the dye at different pH values [9-14, 17-19, 25, 28, 41, 42]. The certainty of acid- base nature of the equilibrium relies on sigmoidal shape of the plot of absorbance at analytical wavelength against pH [1b, 9, 17, 18, 41, 42]. The criterion for the azo-hydrazone nature of the equilibrium is usually considered the presence of isosbestic points on the superposed spectra of isomolar solutions of azocoupling product in binary mixtures of the same solvents with different mixture composition [2, 18, 45]. Also, as a rule, the criterion for aggregation nature of the equilibrium is the occurrence of isosbestic points on the spectra obtained at different dye concentrations but keeping a constant value of $C_{Di} \cdot l_i$ [1b, 23, 24, 26, 28b].C_D stands for molar concentration of dye and l for optical path length of the cell. However, the presence of isosbestic points as the solvent or concentration of the azocoupling products is changed was interpreted by other authors by involvement of acid-base equilibrium [8, 9, 12b, 13]. Contradictory interpretation was also given in the analysis of temperature [3, 9b, 12b, 13, 18, 22, 24, 29, 32, 35] or time [9, 10, 20, 30] dependence of the spectra. The nature of the exhibited equilibrium is even more difficult to ascertain for azocoupling products that may be involved in several types of equilibria [8-10, 14, 22-25]. Our investigating products **1-4** belong to this category. Therefore, the aim of this work is to evaluate the criteria of the UV-Vis spectrophotometry for establishment the nature of the equilibria exhibited under the influence of various factors by each azocoupling products **1-4**. With this aim in view a comparative study of the effects of various factors on the spectra of azocoupling products has been undertaken using ethanol- water mixtures. Spectra were recorded at several pH values (Fig 1, 2a, 3, 4a, 5a, 6), water content (Figure 2b, 5c, 7), sample concentration (Figure 4b, 5b, 8c, 9), temperature (Figure 8b, 10) and various periods of time after the preparation of solutions (Figure 11a, b). Also an absorption spectrum in solid state (Figure 12) was recorded. The products **1**-**4** belong to the 4-arylhydrazono-3-methyl-1-(6-methyl-5R-4-X-pyrimidin-2-yl)-pyrazolin-5-ones, that are studied by our group for some time [6, 9, 33, 40-42, 46, 47]. The dyes **1**-**4** were obtained from 1-(4-hydroxy-6- methylpyrimidin-2-yl) pyrazolin 5-one (**5)** and nitrobenzenediazonium salts (**6)** (Scheme 1)

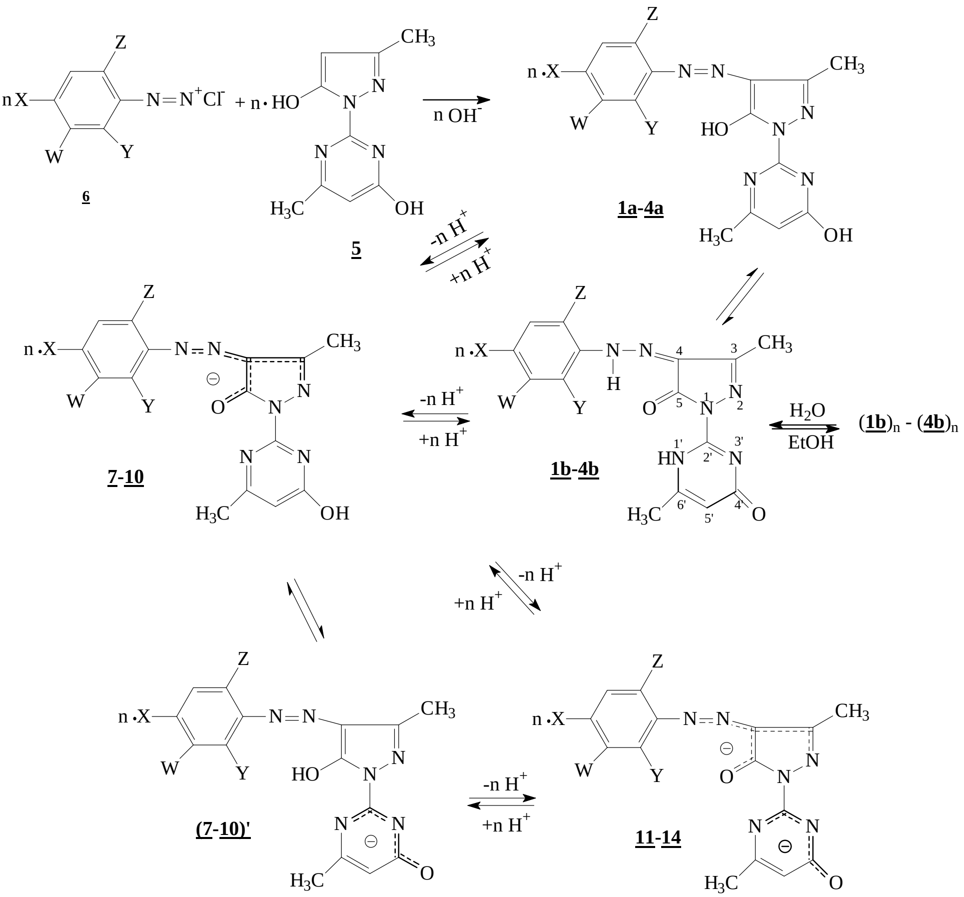

1; **7**; **11**; X =NO$_2$; Y=Z=W=H

2; **8**; **12**; X =NO$_2$; Y=Z=Cl; W=H

3; **9**; **13**; X=Z=W=H; Y=NO$_2$

4;**10**; **14**; X=Y=Z=H; W=NO$_2$

Scheme 1

RESULTS AND DISCUSSION

Preliminary remarks

The azocoupling products **1**-**4** may exist potentially in several tautomeric forms (*e.g.* **1a**-**4a**; **1b**-**4b** Scheme 1) [33, 40-42, 46, 47]. Since these tautomeric forms have two mobile hydrogen atoms (HO- or NH-), they may be involved [41, 42] in two-steps ionization equilibria to form **7**-**10** (**7**-**10**)' and **11**-**14** respectively [9, 14, 19]. Also, similar to other azocoupling products [1b, 3, 10, 14, 20-30], the dyes **1**-**4** might be involved in aggregation equilibria to form $(\mathbf{1b})_n$-$(\mathbf{4b})_n$. In spite of all these, UV-Vis absorption spectra in some aprotic solvents as benzene, chloroform, dimethyl sulfoxid, as well as IR spectra in solid state and the NMR-spectra in $CDCl_3$ (Table 1), have detected the presence of a single chemical species [33, 40-42] for each dye **1**-**4**. The same result was also found in the case of other similar pyrazolin-5-one azocoupling products [2, 4-6, 9, 33, 40, 41]. The structure of this species has been assigned to the hydrazone tautomer (*e.g.* **1b**-**4b**), especially on the basis of NMR data [2, 4-6, 9, 33, 40-42]. The undoubted proof for this form is considered the appearance on the ^{1}H-NMR spectra of the pyrazolin-5-one azocoupling products of a singlet signal in the range 13-15 ppm (cf. Table 1), that has been demonstrated to be characteristic for the hydrazone-hydrogen atom (-HN-N=C<) from such compounds [2, 4-6, 9, 33, 40, 41].

Table 1. Some I.R. and ^{1}H-RMN data of the azocoupling products **1**-**4**.

Dye	I.R. data (υ [cm^{-1}] in KBr pellets				^{1}H-RMN data (δ[ppm]) in $CDCl_3$		
	$\upsilon_{C=O}$ (pyrazolin-5-one)	$\upsilon_{C=O}$ (pyrimidin-4'-one)	υ_{NO2}		δ $H_{5'}$ singlet	δ NH or OH (pyrimidin-4'-one) singlet	δ NH (hydrazone) singlet
			antisym	sym			
1	1696	1673	1556	1344	6.15	10.93	13.17
2	1690	1680	1556	1340	6.15	10.73	13.19
3	1711	1674	1543	1333	6.14	11.15	14.63
4	1697	1672	1535	1352	6.04	11.0	13.09

However, the UV-Vis absorption spectra of the dyes **1**-**4** in other solvents, particularly in ethanol –water or methanol solutions by the increase of acid, base or water content (Figure 2a, 3, 5a, 6), are compatible with the existence of an equilibrium between at least two species, one of them has been established to be the hydrazone tautomer **1b**-**4b** [33, 40-42].

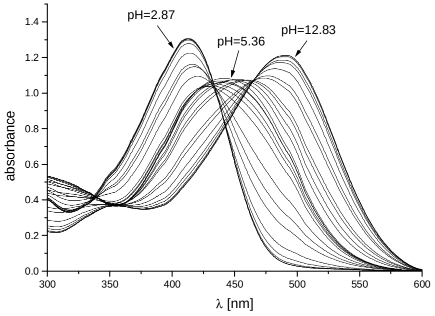

Figure 1. The pH' dependence of the UV-VIS absorption spectra of the isomolar solutions of **1** ($2.25\cdot10^{-5}$ mol·L^{-1}, 5 cm cells) in the pH' range 2.87-12.8.

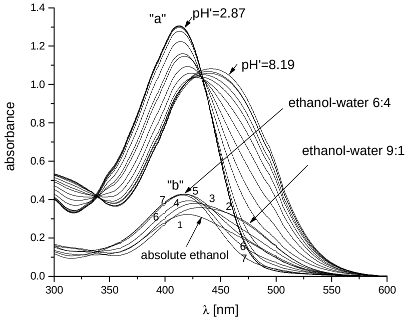

Figure 2. a) The pH' dependence of the UV-VIS absorption spectra of the isomolar solutions of **1** ($2.25\cdot10^{-5}$ mol·L^{-1}, 5 cm cells) in the pH' range 2.87-8.19.

b) The water content dependence of the UV-VIS spectra of the isomolar solutions of **1** ($2.68\cdot10^{-5}$ mol·L^{-1}, 2 cm cells) in ethanol/ water mixtures **1**-10v/0v; **2**- 9v/1v; **3**-8v/2v; **4-**7v/3v; **5**-6v/4v; **6**-5v/5v; **7**-4v/6v.

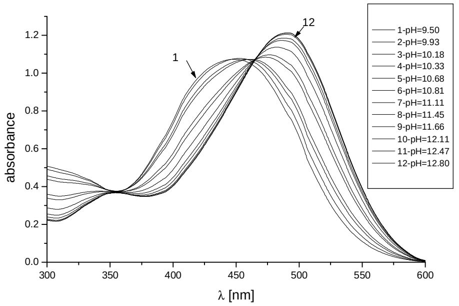

Figure 3. The pH' dependence of the UV-VIS spectra of the isomolar solutions of **1** ($2.25\cdot10^{-5}$ mol·L^{-1},5 cm cells) in the pH' range 9.5-12.8.

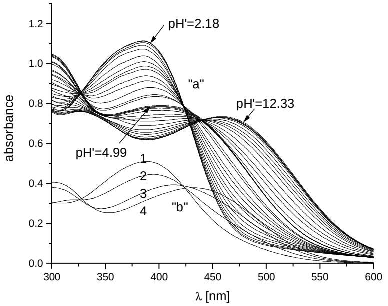

Figure 4. a) The pH' dependence of the UV-VIS spectra of the isomolar solutions of **2** ($2.35\cdot10^{-5}$ mol·L^{-1}, 2 cm cells) in the pH' range 2.18-12.33. b) The concentration dependence of the UV-Vis spectra of **2** at 25^{0}C. The dye concentration and path length of the cell are given: **1)**-$7.06\cdot10^{-5}$; 0.5, **2)**-$3.53\cdot10^{-5}$; 1, **3)**-$1.76\cdot10^{-5}$; 2, **4)**-$7.07\cdot10^{-6}$; 5.

Similar behaviour of other azocoupling products have been considered to indicate azo-hydrazone- [2, 6, 18, 33, 40, 43-45], acid-base- [9, 11, 12, 16, 17, 42] or aggregation- [3, 30] equilibria, possible interconnected [8, 13, 14]. Therefore in the next sections we try to establish which of the equilibria in Scheme 1 are in fact involved.

The pH' influence. Determination of the pK$_a$' values

Since the azocoupling products **1**-**4** are insoluble in water the pH influence on the UV-Vis absorption spectra of these was investigated in ethanol-water (1v/1v) solutions. For this reason we use the notations pH' and pK$_a$'.

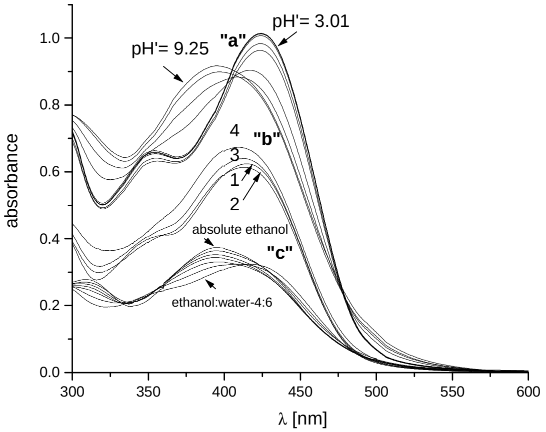

Figure 5. a) The pH' dependence of the UV-VIS spectra of the isomolar solutions of **3** ($3.52 \cdot 10^{-5}$ mol·L^{-1}, 2 cm cells) in the pH' range 3.01-9.25. b) The concentration dependence of the UV-Vis spectra of **3** at 25^{0}C. The dye concentration and the path length of the cells are given: **1)**-$9.0 \cdot 10^{-5}$; 0.5, **2)**-$4.5 \cdot 10^{-5}$; 1, **3)**-$2.25 \cdot 10^{-5}$; 2, **4)**-$9.0 \cdot 10^{-6}$; 5. c) The water content dependence of the UV-VIS spectra of **3** ($1.22 \cdot 10^{-5}$ mol·L^{-1}, 2 cm cells) in ethanol-water mixtures. **1)**-absolute ethanol; **2)**-ethanol-water (9v/1v); **3)**-ethanol-water (8v/2v); **4)**-ethanol-water (7v/3v); **5)**-ethanol-water (6v/4v); **6)**-ethanol-water (5v/5v); **7)**-ethanol-water (4v/6v) (2 cm path length cell).

The different pH' values in the range 2-13 were obtained by addition of either HCl or KOH- solution, having the concentration 10^{-2}-10^{-1}mol·L^{-1}, to discourage dye aggregation [9, 11]. As can be observed in Figure 1, 2a, 3, 4a, 5a, 6, the spectra recorded at different pH' values differ usually both by the position (λ_{max}) and intensity (ε_{max}) of the longest wavelength absorption maximum. Regards the spectra of the isomolar dye solutions over the whole range of pH', one can observe that isosbestic points do not appear with all these recordings (Figure1, 4a). On the other hand, if the solution pH' is modified either in alkaline (Figure 3), or acid to weak alkaline (Figure 2a, 5a, 6) domain, spectra corresponding to each of the two pH' regions exhibit isosbestic points.

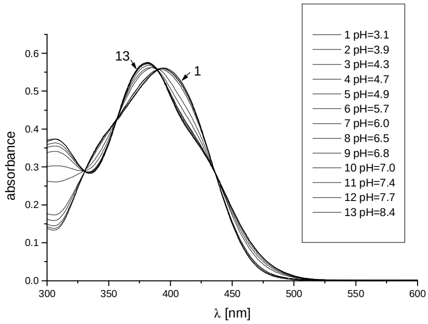

Figure 6. The pH' dependence of the UV-VIS absorption spectra of the isomolar solutions of **4** ($3.66\cdot10^{-5}$ mol·L^{-1}) in the pH' range 3.1-8.4.

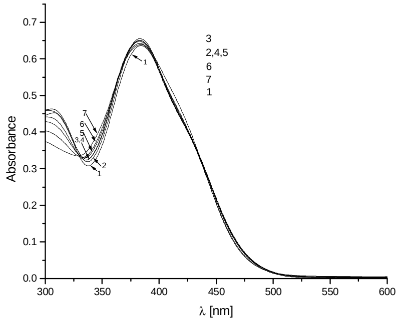

Figure 7. The water content dependence of the UV-VIS absorption spectra of the isomolar solutions of **4** (c $=2.44\cdot10^{-5}$ mol·L^{-1}) in ethanol: water mixtures:**1)**- 10v/0v; **2)**-9v/1v; **3)**-8v/2v; **4)**-7v/3v; **5)**-6v/4v; **6)-**5v/5v; **7)**-4v/6v.

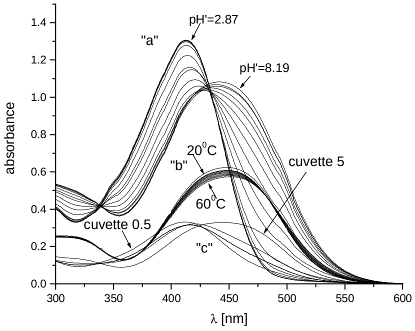

Figure 8. a) Identical with Figure 2a; b) The temperature dependence of the UV-VIS spectra of **1** (c $=3.09\cdot10^{-5}$ mol·L^{-1}) The concentration dependence of the UV-Vis spectra of **1** at 25^{0}C. c) The dye concentration and the length of the cells are given. **1)**-$3.09\cdot10^{-5}$; 0.5, **2)**-$1.54\cdot10^{-5}$; 1, **3)**-$7.7\cdot10^{-6}$; 2, **4)**-$3.09\cdot10^{-6}$; 5.

For example, in the case of the dye **1** the two pH' range, in which the spectra exhibit isosbestic points, are: 9.5 - 12.83 (Figure 3), and 2.87 - 8.19 (Figure 2a), respectively. By plotting the peak absorbance *vs*. pH' for each of the two pH' regions a sigmoidal curve has resulted, as exemplified by Figure 13 for the pH' region 2.87- 8.19 in case of dye **1**. The two sigmoidal curves obtained for each dye prove the involvement of the dyes into two acid-base equilibria that account for the pH' influence on the UV-Vis absorption spectra. Based on the fact that the compounds **1**-**4** are potentially AH_2 acids, the above described behaviour should correspond to the two-step acid ionization equilibria of the type: $AH_2 \leftrightarrows AH^- + H^+$ and $AH^- \leftrightarrows A^{2-} + H^+$. The species: AH_2, AH^-, A^{2-} involved could be identified by characteristic visible absorption bands for each dye. The position and the intensity of the corresponding maxima are presented in Table 2. For example, in the case of dye **1** these maxima have λ_{max} at 412.5 (AH_2 = **1b**), 441.5 (AH^- = **7** or **7'**) and 490.5 nm (A^{2-} = **11**), respectively (Figure 1). The structures of the unionized species AH_2, for the dyes **1**-**4**, correspond to the hydrazone tautomers **1b**-**4b,** while the ionized species AH^- and A^{2-}, as for other azocoupling products [2, 9, 11, 12, 28b, 33, 40-42], should have structures that are predominantly azo in character, corresponding to **7**-**10** or (**7**-**10**)' for the anion (AH^-), and to **11**-**14** for the anion (A^{2-}) (Scheme 1).

Table 2. The UV-VIS spectra data {λ_{max}[nm]; (ε_{max} [L mol^{-1} cm^{-1}])} and the denotation of the species (of type AH_2, AH^-, A^{2-}) involved in the deprotonation equilibria of the azocoupling products **1**-**4** and the corresponding pK_a' values, in ethanol-water (1v/1v).

Dye	The type of species involved			the pK_a' values	
	AH_2	AH^-	A^{2-}	pK_{a1}'	pK_{a2}'
1	412.5 (29038) pH′=2.87 **1b**	441.5 (24046) pH′=8.19 **7**	490.5 (26928) pH′=12.8 **11**	5.84	10.56
2	386 (23705) pH′=2.18 **2b**	415 (16121) pH′=6.56 **8**	461 (15482) pH′=12.4 **12**	3.87	10.34
3	424 (14408) pH′=3.01 **3b**	394.5 (13027) pH′=9.25 **9**	430 (12551) pH′=12.74 **13**	6.88	10.88
4	394 (30638) pH′=3.1 **4b**	381.5 (31378) pH′=8.4 **10**	397 (27034) pH′=12.5 **14**	5.63	11.0

Moreover the sigmoidal curves enable us to determine the pK_a' values of the two-step ionization equilibria of the dyes by means of the inflection points. These are precisely determined by means of the first derivative of each curve as shown in Figure 14 [9, 41,42]. The pK_{a1}' and pK_{a2}' values for each dye **1**-**4** are presented in Table 2.

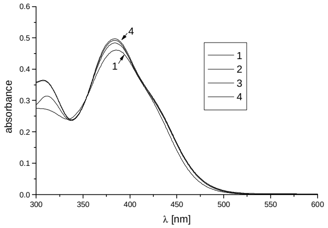

Figure 9. The concentration dependence of the UV-VIS spectra of **4** at 25^{0}C. The dye concentration and the path length of the cells in cm are given. **1)**-1.07·10^{-4}; 0.5, **2)**-5.35·10^{-5}; 1, **3)**-2.67·10^{-5}; 2, **4)**-1.07·10^{-5}; 5.

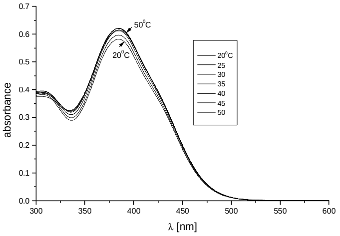

Figure 10. The temperature dependence of the UV-VIS spectra of **4** (5.35·10^{-5} mol·L^{-1}).

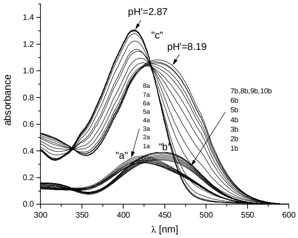

Figure 11. a) The time dependence of the UV-VIS spectra of **1** (2.81·10^{-5} mol·L^{-1}, 1 cm cells) in absolute ethanol (Chimopar). The time delay in minutes. **1)**-0 ; **2)**-1; **3)**-6; **4)**-24; **5)**-36; **6)**-79; **7)**-168; **8)**-255. **b)** The time dependence of the UV-VIS spectra of **1** (2.11·10^{-5} mol·L^{-1}, 1 cm cells) in absolute ethanol (Chimopar: Cristal 3v/1v).). The time delay in hours. **1)**-0; **2)**-0.016; **3)**-0.083; **4)**-0.116; **5)**-0.3; **6)**-1; **7)**-1.83; **8)**-3.56; **9)**-24; **10)**-48; **11)**-72. (1 cm path length cell). **C)** Identical with Figure 2a.

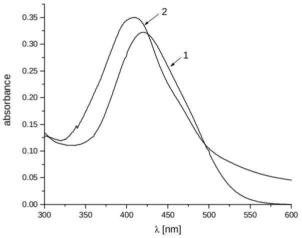

Figure 12. The UV-VIS absorption spectra of **1.** **1)** in absolute ethanol solution; **2)** in solid state.

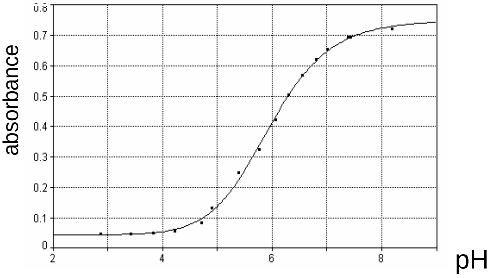

Figure 13. The plot of absorbance *vs.* pH` corresponding to the absorption curves from Figure 2a, at analytical wavelength of 490 nm.

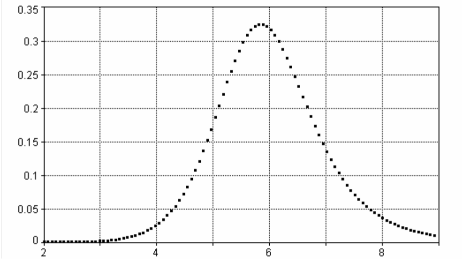

Figure 14. The first derivative of the plot from Figure13, that yields the pK$_{a1}$' value for **1.**

Interesting structural effects were observed from the manner of pH' influence on the spectra. The increase of pH' in the range of first step ionization causes a bathochromic shift of the longest wavelength band in the case of azocoupling products **1**, **2** (Figure 2a; 4a) having the nitro group in *para* position on their benzene ring relative to N-N bridge, even if there are other subtituents present[9a]. On the contrary, the same pH' increase determines a hypsochromic shift of the maximum in the case of the azocoupling products having the nitro group in *ortho* (**3**) (Figure 5a) or *meta* (**4**) (Figure 6) position. It should be noted that this last behaviour is similar to that observed in the case of other azocoupling products that do not have nitro group, obtained also from **5** or its derivatives [6, 9, 33, 40, 41]. The exception caused by the nitro group in *para*-position in the manner of pH' influence on spectra is probably determined by the possibility of a very strong conjugation between this group and the negatively charged oxygen atom bound in position 5 of the pyrazole ring of the corresponding de-protonated species **7**, **8** [40]. Such strong conjugation is favoured by the known planarisation effect caused by a nitro group located at one end of an extended delocalized π-electron system through which it is able to conjugate directly with a strong electron donating group from the other end of the mentioned system [48].

Concerning the pKa values, it is worth mentioning that pKa_1' values are much more influenced by the nature and position of the substituent as compared to the pKa_2' values. The pKa_1' value of *ortho* substituted derivative (**3**) is greater than the pKa_1' value of the corresponding *meta*- (**4**) or *para*- (**1**) substituted-derivative as found with other azocoupling products [1a,11,12a] (cf. Table 2). The *ortho*-effect [40] accounts for larger pKa_1' value of the *ortho* substituted derivative.

The influence of water content in ethanol - water mixtures

The UV-Vis absorption spectra of the isomolar solutions of the dyes **1**-**4** in ethanol - water mixtures depend on the water content (Figure 2b, 5c, 7) in a different manner. Thus, the spectra of dyes **1**, **2** recorded at different water content in ethanol - water mixtures, do not exhibit isosbestic points (Figure 2b). The corresponding spectra of **3** and **4** (Figure 5c, 7) exhibit isosbestic points even if these are more or less distorted. Therefore, it may be admitted that water content dependence of the spectra of the dyes **3** and **4** indicates the presence of an equilibrium. The similarity of this dependence with the pH' dependence corresponding to the first ionisation step (Figure 5a, 6) infers that water content effect implies the same type of ionization equilibrium, namely **3b**$\leftrightarrows$**9** and **4b**$\leftrightarrows$**10** respectively. A similar reasoning was given also by other authors for the solvent effect in the case of other azocoupling products [9, 12b, 13, 41]. In accordance with the above assumption, the progressive increase of water content of the mixture (Figure 5c) has a similar effect on the spectra as that of acidity increase in the range of first acid ionisation of **3** (Figure 5a) It consists in a bathochromic shift, corresponding to the change of equilibrium **3b⇆9** towards hydrazone form **3b**, that has λ_{max} at 424 nm, while the anion **9** has λ_{max} at 394.5 nm. This shift caused by the increase in water content of solution is in agreement with the fact that the water is a stronger acid than ethanol[9, 13]. It is however worth mentioning that such a shift of the observed equilibrium in the case of dye **3** towards **3b** by the water content increase is compatible with azo-hydrazone nature of this equilibrium, taking into account the assessment that water displaces the azo-hydrazone equilibrium towards hydrazone tautomer [2, 28, 43-45]. Nevertheless, because the presence of the azo tautomer **3a** is not proved, the probability that water content dependence observed in Figure 5c to be caused by azo-hydrazone equilibrium is correspondingly very low. But the possibility to explain the observed effect of the water content either on the basis of ionization or azo-hydrazone equilibrium shows that the usual criterion to assess the azo-hydrazone nature of the equilibrium exhibited by a potentially tautomeric azocoupling product is somehow in doubt.

On the other hand, the appearance of distorted isosbestic points, when water content effect on the spectra of the dye **3** (Figure 5c) was examined, may be caused by the superposition of the acid-base equilibrium with other phenomena, including other equilibria [9, 14]. Such a superposition rather occurs with the dyes **1**, **2**, where water content dependence of the spectra does not exhibit isosbestic points (Figure 2b). The last assumption is confirmed by a comparative study of the water content dependence of dye **1** spectra with the corresponding pH' dependence in the range of first acid ionization (pKa_1', Figure 2a). The simple comparison of the Figure 2a and 2b shows that apparently the species involved in both dependences are the same. This situation is compatible with the possibility that also for the dye **1** one of the reason of the water content dependence of the spectra to be an acid- base equilibrium. A strong support for that is the hypsochromic shift observed by the stepwise increase of water content of solutions of the dye **1** in ethanol- water mixtures from the composition 9v/1v (curve 2 in Figure 2b) up to composition 4v/6v (curve 7). This shift is in perfect agreement with the similar shift caused by the increase of acidity in the range of first acid ionisation (**1b⇆7**, Fig, 2a). In fact, the discussed hypsochromic shift is brought about by the protonation of the HA^- species **7** (λ_{max} = 441.5 nm), to the neutral hydrazone H_2A species **1b** (λ_{max} = 412.5 nm). However, similar to the dye **3,** the water content dependence of the spectra illustrated by the curves 2-7 from figure 2b is also compatible with azo-hydrazone equilibrium. But the probability that the water content dependence illustrated by curves 2-7, to be mainly determined by the azo-hydrazone equilibrium is very low, since the presence of the azo tautomer **1a** is not proved.

On the contrary, the bathochromic shift noticed when compare the spectrum of dye **1** in absolute ethanol with that of the ethanol-water solution in the ratio 9v/1v, cannot be rationalized only on basis of the involvement of an acid-base equilibrium. As shown above, the water addition should cause a hypsochromic shift (Figure 2b). Also, the bathochromic shift observed by the passing from curve 1 (λ_{max} at 420 nm) to curve 2 (λ_{max} at 435 nm) is not compatible with azo-hydrazone equilibrium, because it is considered that water shifts equilibrium towards hydrazone form [2, 28, 43-45]. This form of dye **1** exhibits an absorption maximum located at 412.5 nm (a hypsochromic shift). Consequently the bathochromic shift found should be caused by the involvement of other phenomena along with acid-base equilibrium by changing the water content. Such a phenomenon might be a disaggregating process of an aggregate (**1b**)$_n$ formed from molecules of hydrazone **1b**. Such an aggregate is expected to have the visible absorption band superposed on that of the hydrazone **1b,** as occurs with other aggregates of azocoupling products [21,23,24].

The aggregate is somehow stable in absolute ethanol. It disintegrates easily at water addition. Further, the hydrazone **1b** is involved simultaneously with its formation from the aggregate, in ionization equilibrium **1b** ⇆ **7** (Scheme 1). The position of this equilibrium in the ethanol-water (9v/1v) solution correspond to a partial ionization to **7** (100% **7** has λ_{max} = 441.5 nm, Table 2). Thus, the bathochromic shift observed comparing curves 1 and 2 (Figure2b) is in agreement with a partial disaggregating process (**1b**)$_n$ → n **1b**, accompanied by the establishing the acid-base equilibrium **1b** ⇆ **7**. Due to the presence of the anion **7** in this solution, the absorption maximum is bathochromically shifted relative to the absorption maximum of the aggregate and of the hydrazone form **1b** (~ 412 nm). The possible existence of the aggregate (**1b**)$_n$ is also argued in Sections 3.6 and 3.7.

The influence of the sample concentration

The UV-Vis absorption spectra of the dyes **1**-**4** in ethanol solutions, modifying the dye concentration in the range 10^{-6} - 10^{-4}mol·L^{-1} and keeping constant the product $c_D^i \cdot l^i$, exhibit isosbestic points in most cases (Figure 4b; 8c; 9), even if some are distorted (Figure 4b, 8c). An exception was found where isosbestic points do not appear (Figure 5b). When isosbestic points appear (dyes **1**, **2**, and **4**) by concentration change, an equilibrium should be present. The decrease of the dye concentration has an effect on UV-Vis absorption spectra (Figure 4b, 8c, 9) similar to the effect caused by the increase of the pH' in the region of first acid ionization step (Figure 4a, 8a, 6). Based on these findings the most reasonable cause for the dye concentration effect in the case of dyes **1**, **2** or **4** should be the equilibrium corresponding to the first acid ionization step. This is supported by the known fact that the ionization of an acid (e.g. $AH_2 \leftrightarrows AH^- + H^+$) is promoted by the pH' increase and by dilution. A similar interpretation has been given previously in the case pf other azocoupling products [9, 12b, 13].

The above given explanation shows however that the usual criterion to establish the aggregation nature of the equilibrium, namely the occurrence of isosbestic points by the dependence on concentration of the spectra, seems to be invalid in the case of the dyes **1**, **2**, **4**. Consequently, this criterion appears to be uncertain.

On the other hand, also the observed shift of the longest wavelength absorption maximum as a result of dye concentration decrease for all dyes (Figure 8c, 4b, 5b, 9) does not appear to be due to aggregation equilibrium, as main reason for dye concentration dependence. As shown in aggregation equilibrium of potentially tautomeric azocoupling products, the decrease of dye concentration should displace it towards the non-aggregated form [1b, 26, 28b]. Such a form, in the case of the dye **1**, *e.g.*, should correspond to the hydrazone **1b** that should lead to a shift towards 412.5 nm. In fact, we have noticed a reverse shift up to 442 nm (Figure 8c). Such a bathochromic shift (from 388 to 435 nm) is also observed with the dye **2**. If **2** would be involved in aggregation equilibrium, the band position shift should be a hypsochromic one, towards 388 nm. In reverse, the dyes **3** and **4** exhibit hypsochromic displacement of the bands as their concentration decrease (Figure 5b, 9). If the dyes **3** and **4** would be involved in aggregation, the shifts should be bathochromic. These displacements (**1**, **2**-bathochromic; **3**, **4**-hypsochromic) are rather compatible with the involvement of all dyes in acid-base equilibrium, corresponding to the first ionization step (Figure 8a, 4a, 5a, 6).

The influence of the temperature

The change of temperature within the range 20-60℃ influences slightly and differently the UV-Vis absorption spectra of the dyes **1**-**4** in ethanol solutions (*e.g.* Fig 8b, 10). In the case of dye **1** (Figure 8b), the absorption curves recorded at various temperatures exhibit isosbestic points and changes of the spectra by the temperature increase are reversible. This behaviour is characteristic to the presence of an equilibrium, which seems to correspond to acid ionization equilibrium **1b** ⇆ **7** since the absorption curves shown in Figure 8b are similar to some absorption curves recorded in pH' region of the first ionization step (Figure 8a).

On the other hand, the temperature dependence of the spectra of the dyes **2**-**4** do not exhibit isosbestic points and the change determined by the temperature increase is more or less regular and apparently not reversible (*e.g.* Figure 10). These experimental results show clearly that the temperature dependence of the spectra of the dyes **2**-**4** cannot be rationalized only by involvement of an acid-base equilibrium.

The influence of the time

The time dependence has been investigated by the recording of the UV-Vis absorption spectra of the dye **1** at various time intervals after preparation of the solution in absolute ethanol (Figure 11b, c). As a function of the ethanol used as solvent, purchased from two commercial sources, different sets of absorption curves have been obtained. The two sets differentiate by the position (Figure 11b, c; $\Delta\lambda_{max}$ = 22 nm) and shape of the visible absorption band that is characteristic for all the spectra belonging to a certain series of measurements. The spectra recorded with different sorts of ethanol differ among them as they were recorded at two different pH values (Figure 11a). The difference of the two series consist of the shift brought about by the different pH' values of the two sorts of ethanol [9b].

On the other hand, the set of absorption curves of dye **1** as a function of time in each experiment does not exhibit isosbestic points. A gradual increase of the absorbance by time since preparation of the solution takes place. The absorbance increase ceases within several hours and is apparently irreversible. These findings cannot be rationalized by the involvement of an acid-base equilibrium only. Other phenomena should cause this behaviour, namely some processes taking place more slowly than proton transfer [49]. The slow process in solution of an azocoupling product might be either aggregation or azo-hydrazone equilibrium, as asserted by nearly all the papers that describe the time dependence of the spectra of other azocoupling products [10, 20, 29, 30, 36].

Taking into account all the data presented in this work, the most reasonable cause for the time change of the UV-Vis absorption spectrum of the dye **1** in absolute ethanol is a slow disaggregating process $(\mathbf{1b})_n \rightarrow n\cdot\mathbf{1b}$. This explanation supposes that the absorption bands of the aggregate $(\mathbf{1b})_n$ and of hydrazone **1b** are superposed, and the absorption coefficient of the aggregate is lower than that of the hydrazone **1b**. Situation like that has been described previously in several aggregation studies of other azocoupling products [21, 23, 24]. In addition, the hydrazone **1b** released from the aggregate undergoes a rapid deprotonation $\mathbf{1b} \leftrightarrows \mathbf{7}$**.** A deprotonation of aggregate itself is not excluded. Consequently, the aggregate, hydrazone **1b** and the anion **7** co-exist in ethanol solution of **1**. The proportion depends upon time and pH' of the sort of ethanol used. Due to the presence of the anion **7** (λ_{max} = 441.5 nm), the ethanol solution maximum is shifted bathochromically as compared to that of the aggregate and the hydrazone **1b** (λ_{max} = 412.5 nm). Such a disaggregating process can also justify the bathochromic shift by passing from a solution in absolute ethanol to that of ethanol- water mixture in the volumetric ratio 9:1.

Comparison of dye 1 spectrum in absolute ethanol and in solid state

Several authors consider that the dyes in solid state as crystals [50-52], as powder [1d, 23], adsorbed [1b, 20] or deposited [53] on a substrate, contain aggregates [1b, 1d, 20, 23, 50-53] along with the monomeric species.

This assessment is supported by the similar UV-Vis absorption spectra of a certain dye in solid state and in solution, when the aggregation in solution has been asserted [20, 23, 50, 5]. In fact, because the type of intermolecular interactions involved in the generation of the aggregates in solution [cf. 1b, 1e] and of the solid state are often the same for a certain dye, one expects that the spectra to be similar. In this context, the experimental findings that the UV-Vis absorption spectra of the dye **1** in absolute ethanol and in solid state are quite similar (Figure 12) might be considered [53] an argument for the existence of an aggregate $(\mathbf{1b})_n$ of dye **1** in absolute ethanol along with the forms **1b** and **7**.

CONCLUSIONS

The pH' influence on the UV-Vis absorption spectra of the azocoupling products **1**-**4** in aqueous ethanol is reliable explained by the involvement of each dye in two-steps acid ionization equilibria.

The comparative study of the pH' influence on the UV-Vis absorption spectra of the dyes **1**-**4** with the corresponding influence of other external factors on the spectra has revealed that: i) the water content, dye concentration or temperature dependence, with the occurrence of isosbestic points, may be adequately explain by the involvement of dye in the first-step acid ionization equilibrium; ii) the effect of the same factors and time on the spectra, when isosbestic points do not exist, is apparently due to superposition of the first-step acid ionization equilibrium and other phenomena.

The results of this work lead to the assessment that, when the effect of solvent, of dye concentration, temperature or time on the UV-Vis absorption spectra of potentially tautomeric azocoupling products is studied, the condition to ascertain as accurately as possible the nature of the involved equilibrium needs a comparison with the pH' influence.

EXPERIMENTAL SECTION

The synthesis and purification of the dyes **1**-**4** were performed as previously described [33,40-42,47]. The coupling component **5** and the nitrobenzenediazonium salts **6** were obtained according to our previously reports [40, 41, 47]. Analytical grade reagents and solvents were provided by Merck (Darmstadt), Fluka (Buchs), Chimopar and Cristal (Bucharest). These were used without further purification. The water to prepare the solutions was distilled twice. As a rule, a relative concentrated stock solution (10^{-5}-10^{-4} mol·L^{-1}) of each dye **1-4** in ethanol was prepared. This solution was used as such or diluted with ethanol or water to the concentration requested by the UV-Vis spectrophotometric measurements (10^{-6}-10^{-5}mol·L^{-1}). The ionization constants (pK_a' values) were determined spectrophotometrically at 25^0 C, in the presence of 0.01 mol·L^{-1} KCl, on the basis of correlation between pH' and absorbance (figure 13) at analytical wavelength. [9, 16-19, 25]. The correlation was fitted with the aid of the programme *Table Curve Windows v. 1.10, Table Curve^{TM}, Jandel Scientific, Copyright 1989-1993 AISN Software*. The UV-Vis absorption spectra were performed on *Jasco-V-530 spectrophotometer*. Matched glass or quartz cells of 0.5, 1, 2 and 5 cm path lengths were used. The cells have been tightly sealed during the measurement when temperature or time dependence was followed. The experimental pH' values corresponding to the working conditions were measured by digital *Practronic MV-87 pH meter* equipped with a combined *pH-reference electrode ESHC-02*, produced by Naposenz SRL, Cluj-Napoca. The temperature was controlled by means of an ultra thermostat. The UV-Vis spectrum of **1** in solid state was recorded with a sample deposited as a solid film by application of drops of solution of **1** in chloroform on a quartz plate, followed by the complete evaporation of the solvent at room temperature. The IR spectra were recorded as KBr pellets on a *Jasco 615 ET-IR spectrometer.* The ^{1}HNMR spectra were performed with *FT-Bruker Avance 300 NMR spectrometer.*

Acknowledgements

Financial support from Romanian National University Research Council (CNCSIS), Grant A No. 1347/2007, is gratefully acknowledged by the authors.

REFERENCES

1. H. Zollinger; *Colour Chemistry*; VCH, Basel, 2 nd edn **1991**; a) p. 133-137 b) p. 288-291 c) p. 132, d) p. 299; 300 e) p. 270-272.
2. H. Mustroph; *Z. Chem*; **1987**, *27(8),* 281.
3. M.H. Habibi, A. Hassanzadeh, A. Zeini-Isfahani; *Dyes Pigm.*; **2006**, *69*, 93.
4. J. Elguero, C. Marzin, A.R. Katritzky, P. Linda; *The Tautomerism of Heterocycles*, Academic Press, New York; 1976, p. 336-339
5. A. Lycka, H. Mustroph, *J. Prakt. Chem.*, **1989**, *331(1),* 11.
6. I. Panea, A. Ghirişan, I. Cristea, R. Gropeanu, I.A. Silberg; *Het.Commun*; **2001**, *7*, 363.

7. A. Whitaker, *J. Soc. Dyers Colour*., **1995**, *111*, 66.
8. F. Karci, N. Ertan; *Dyes Pigm.*; **2002**, *55*, 99.
9. I. Panea, M**.** Pelea, I.A. Silberg, *Dyes Pigm.*; a) **2006**, *68*, 165; b) **2007**, *74*, 113.
10. M. Dakiky, K. Kanan, M. Khamis, *Dyes Pigm.*, **1999**, *41*, 199.
11. J. Oakes, P. Gratton; *J. Chem. Soc.,Perkin Trans 2,* **1998,** 1857.
12. Q. Peng, M. Li, K. Gao, L. Cheng; *Dyes Pigm.*; a) **1991,** *15*, 263; b) **1992,** *18*, 271.
13. N. Ertan; *Dyes Pigm.*; **2000**, *44*, 41.
14. M. Dakiky, I. Nemcova; *Dyes Pigm.*, **2000**, *44*, 181.
15. L.dlC. Coo, T.J. Cardwell, R.W. Cattrell, S.D. Kolev; *Analytica Chimica Acta*; **1998,** *360*, 153.
16. G.A. Ibanez, A.C. Olivieri, G.M. Escander, *J. Chem. Soc., Faraday Trans*., **1997**, *93(4)*, 545.
17. N.M. Rageh; *J.Chem. Eng. Data*; **1998**, *43*, 373.; M.M. Ghoneim, H.S. El-Desoky, S.A. Amer, H.F. Rizk, A.D. Habazy *Dyes Pigm.*, **2008** *77***,** 493.
18. N. M. Rageh*; Spectrochimica Acta, Part.A*; **2004**, *60*, 1917.
19. A.M. Khedr, M. Gaber, R.M. Issa, H. Erten; *Dyes Pigm.*; **2005**, *67*, 117.
20. C.H. Giles, S.M.K. Rahman, D. Smith, *J. Chem. Soc.*, **1961,** 1209.
21. A.R. Monahan, N.J. Germano, D.F. Blossey, *J. Phys. Chem*, **1971**, *75*, 1227.
22. M. Nepras, M. Titz, M. Necas, S. Lunak jr., R. Hradina, A. Lycka; *Coll. Chem. Commun*.; **1988**, *53*, 214.
23. B.R. Hsieh, D. Desilets, P. Kazmaier; *Dyes Pigm.*, **1990**, *14*, 165.
24. T. Iijima, E. Jojima, L. Antonov, St. Stoyanov, T. Stoyanova; *Dyes Pigm.*; **1998**, *37*, 81.
25. A. Navarro, F. Sanz, *Dyes Pigm.*; **1999**, *40*, 131.
26. M. Dakiky, I. Nemcova; *Dyes Pigm.*, **1999**, *40*, 141.
27. A.R. Kennedy, M.P. Hughes, M.L. Monaghan, E. Staunton, S.J. Teat, W.E. Smith; *J. Chem. Soc., Dalton Trans*; **2001**, 2199.
28. a) K. Wojciechowski, J. Szadowski, *Dyes Pigm.*, **2000**, *44*, 137; b) K. Wojciechowski, J. Gumulak, *Dyes Pigm*., **2003**, *56*, 195.
29. S. Kunanandam, J.R. Lindsay Smith, J.N. Moore, I.P. Clark, *Central Lasers Facility*, Annual Report **2003/2004**, 121.
30. M.H. Habibi, A. Hassanzadeh, A. Zeini-Isfahani; *Dyes Pigm*.; **2006**, *69*, 111.
31. S. Stoyanov, T. Iijima, T. Stoyanova, L. Antonov; *Dyes Pigm*.; **1995**, *27*, 237.
32. H. Joshi, F.S. Kamounah, G. van der Zwan, C. Gooijer, L. Antonov, *J. Chem. Soc. Perkin Trans 2,* **2001**, 2303.
33. I. Panea, A. Ghirişan, I. Bâldea, I. Silaghi-Dumitrescu, L. Crăciun, I.A. Silberg; *Studia, Univ. "Babeş-Bolyai", Chem*; **2003**, *48(2)*, 67.
34. X.M. Liu, B. Yang, Y.L. Wang, J.Y. Wang; *Biochimica et Biophysica Acta*; **2005**, *1720*, 28.
35. E. Fischer, Y.F. Frei; *J. Chem. Soc.*, **1959**, 3159.
36. P. Jacques; *Dyes Pigm*.; **1988**, 9, 129.

37. H. Xu, O.A. Sadik; *Analyst*, **2000**, 125, 1783.
38. C.J. Ward, P. Patel, P.R. Ashton; T.D. James, *Chem. Commun*.; **2000**, 229.
39. A. Bradford, P.L. Drake, O. Worsfold, I.R. Peterson, D.J. Walton, G.J. Price; *Phys. Chem. Chem. Phys.*, **2001**, 3, 1750.
40. I. Panea, A. Ghirişan, F. Iura, R. Gropeanu, I.A. Silberg; *Studia, Univ. "Babeş-Bolyai", Chemia*; **2003**, *48(2)*, 55.
41. M. Pelea; Ph. D. Thesis, Univ. "Babeş-Bolyai", Cluj-Napoca, România **2007**
42. C. Bâtiu, I. Panea, M. Pelea, A. Marcu, L. David, *Studia Univ. "Babeş-Bolyai" Chem*.; **2007**, *52(4),* 77.
43. A. Burawoy, A.G. Salem, A.R. Thompson; *J. Chem. Soc.*; **1952**, 4793.
44. A. Burawoy, A.R. Thompson; *J. Chem. Soc.*; **1953**, 1443
45. L. Antonov, D. Nedeltcheva; *Chemical Society Reviews*; **2000**, *29*, 217
46. I. Bâldea, A. Ghirişan, I. Panea; *J. Chem. Soc., Perkin Trans 2*; **1992**, 1715.
47. I. Panea, A. Ghirişan, I. Cristea, R. Gropeanu, *Rom. Pat.* 114.797 C_1, **1999**
48. P. Skrabal, J. Steiger, H. Zollinger, *Helv. Chim. Acta*, **1975**, *58*, 800.
49. H. Strelow, *Rapid Reactions in Solutions*, VCH, Weinheim, **1992**, chapter 1
50. R. Steiger, R. Kitzing, R. Hagen, H. Stoeckli-Evans, *J. Photogr. Sci.*, **1974**, *22*, 151.
51. A. Mishra, R.K. Behera, P.K. Behera, B.K. Mishra, G.B. Behera, *Chem. Rev.*, **2000**, *100*, 1973.
52. Y. Onai, M. Mamiya, T. Kiyokawa, K.-I. Okuwa, M. Kobayashi, H. Shinohara, H. Sato; *J. Phys. Chem.*, **1993**, *97*, 9499.
53. I. Panea, M. Tomoaia-Cotişel, O. Horowitz, C.-L. Gaspar, A. Mocanu, Cs. Nagy, *Studia Univ. "Babeş-Bolyai" Chem*.; **2007**, *52*(*3),* 79.

STUDIA UNIVERSITATIS BABEŞ-BOLYAI, CHEMIA, LIV, 2, 2009

SYNTHESIS AND CHARACTERIZATION OF A SANDWICH-TYPE CERIUM (IV) COMPLEX DERIVED FROM MONOLACUNARY DAWSON 2-MOLYBDO-15-TUNGSTO-2-PHOSPHATE

ADRIAN-RAUL TOMŞA[a], DANIELA CIOLOBOC[a],
ANA-MARIA TODEA[a,b], LAURA MUREŞAN[a],
VIOLETA PAŞCALĂU[a], MARIANA RUSU[b]

ABSTRACT. The reaction of monolacunary Dawson 2-molybdo-15-tungsto-2-phosphate, i.e. $[1,2\text{-}P_2Mo_2W_{15}O_{61}]^{10-}$ with $Ce(SO_4)_2$ in aqueous solution results in the formation of a new polyoxometalate complex, with the stoichiometry metal:ligand = 1:2. The new complex was isolated as potassium salt, i.e. $K_{16}[Ce(P_2Mo_2W_{15}O_{61})_2]\cdot 34H_2O$. The molecular formula was determined by elemental and thermogravimetric analysis. UV-Vis, FT-IR and ^{31}P-NMR spectroscopy were used to characterize the new compound. Ion-exchange chromatography provided evidence for covalent, inner-sphere bonding of cerium (IV) to the monolacunary $[1,2\text{-}P_2Mo_2W_{15}O_{61}]^{10-}$ heteropolyoxometalate anion. The investigation results strongly suggest a sandwich-type structure with the cerium atom coordinated by two monolacunary Dawson anions.

Keywords: *polyoxometalate, heteropolyoxometalate, cerium, 2-molybdo-15-tungsto-2-phosphate, ^{31}P-NMR*

INTRODUCTION

Polyoxometalates (POMs) are discrete molecular metal-oxygen clusters with unrivaled versatility and structural variety [1-4], and therefore they show a multitude of properties, which has led to applications, in many fields such as catalysis [5], molecular conduction [7-9], magnetism [10], medicine [11,12], luminescence [13], as well as materials science [14].

The synthesis of POMs is mostly rather simple and straightforward, once the proper reactions conditions have been identified. However, the mechanism of formation of POMs, usually described as self-assembly, is not yet completely understood. Therefore, the design of novel POMs remains a challenge for synthetic chemists.

---

[a] *"Babeş-Bolyai" University, "Raluca Ripan" Institute for Research in Chemistry, 30 Fântânele Str., RO-400294 Cluj-Napoca, Romania, rtomsa@yahoo.com*

[b] *"Babeş-Bolyai" University, Faculty of Chemistry and Chemical Engineering, 11 Arany Janos Str., RO-400028, Cluj-Napoca, Romania, mrusu@chem.ubbcluj.ro*

The most rational approach for the synthesis of POMs involves the use of lacunary species. Reaction of a stable, lacunary POM with transition metal or lanthanide ions leads to a product in which the polyoxometalate framework is not modified.

For instance, under hydrolytic conditions, a cluster such as the well-known α-$[P_2W_{18}O_{62}]^{6-}$ Dawson polyoxotungstate may generate lacunary derivatives with one, three or more lacunary sites (Scheme 1) [15-17].

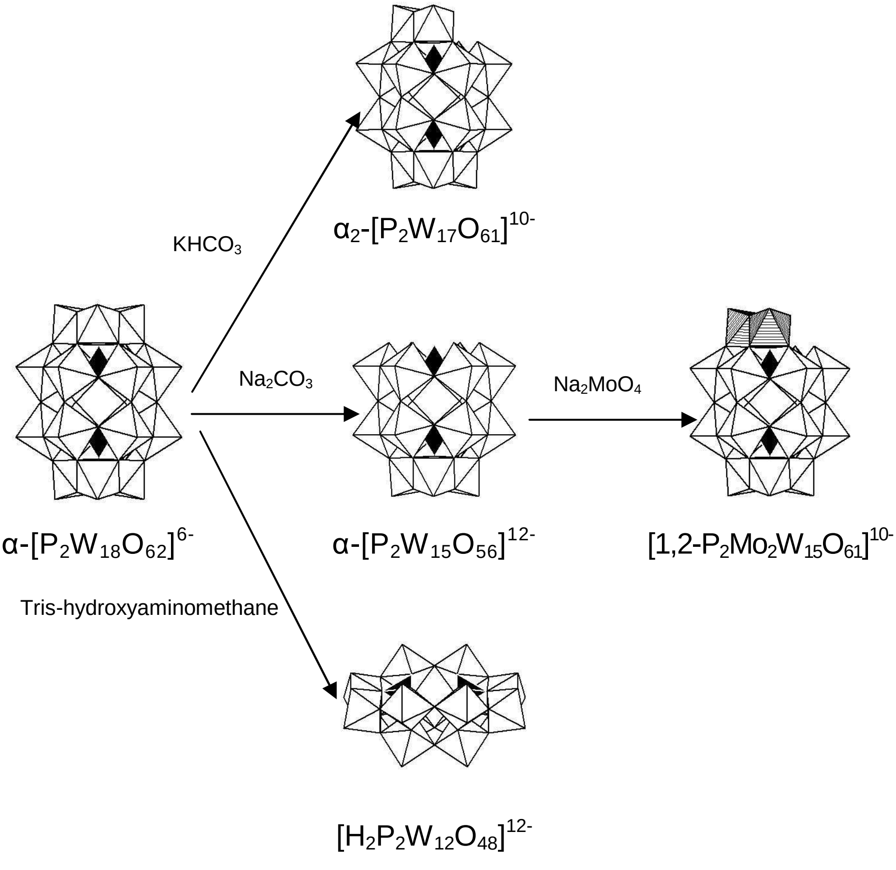

Scheme 1

The reaction of Dawson trilacunary α-pentadecatungsto-diphosphate with molybdate, carried out in mild conditions allows the selective addition of two molybdenum atoms in an apical. It is possible to refill the vacancy of the resulting $[1,2\text{-}P_2Mo_2W_{15}O_{61}]^{10-}$ monolacunary Dawson anion, with transition metal cations. Such complexes with first row transition metal cation exhibit interesting electrocatalytic properties [18-20].

On the other hand, two monolacunary polyoxometalate units may coordinate large central metal ions with high coordination numbers, such as lanthanides or actinides [21-29].

Herein we report the synthesis and characterization of a new complex of Ce(IV) with the $[1,2\text{-}P_2Mo_2W_{15}O_{61}]^{10-}$ monolacunary Dawson polyoxometalate, isolated as aqueous soluble potassium salt $K_{16}[Ce(P_2Mo_2W_{15}O_{61})_2]\cdot 34H_2O$ (**4**). The complex **4** was characterized by elemental and thermogravimetric analysis, UV-Vis, FT-IR and ^{31}P-NMR spectroscopy, as well as by ion-exchange chromatography.

RESULTS AND DISCUSSION

The Ce(IV) complex was synthesized in aqueous solution by reacting the potassium salt of the monolacunary Dawson polyoxometalate $K_{10}[1,2\text{-}P_2Mo_2W_{15}O_{61}]\cdot 18H_2O$ (**3**) with cerium (IV) sulfate. In order to avoid the migration of molybdenum atoms which may give numerous isomers the synthesis must be performed in acidic solution without heating.

Elemental analysis of the cerium (IV) polyoxometalate complex is consistent with the suggested formula.

The thermal stability of **4** was investigated by TG-DTG-DTA. The weight loss in the 25 - 170°C range corresponds to 34 lattice water molecules. The loss of water by heating proceeds in two steps, as observed on the DTG curve. The dehydration process is accompanied by an endothermal process between ~25 - 170°C, as observed on the DTA curve (Figure 1). According to the literature, the first exothermic peak of DTA curve, which usually occurs 20-30°C after the temperature of the polyoxometalate decomposition [30, 31], is regarded as the thermal stability sign of polyoxometalates [32]. For **4**, the first exothermic peak appeared at 489°C, indicating a good thermal stability of the complex. The second exothermic peak at 560°C may be assigned to some phase transitions of the resulting oxides.

When a solution of **4** was loaded onto the sodium form ($P\text{-}SO_3^-Na^+$) of the cation-exchange column, no retention of the Ce(IV) complex was observed. The FT-IR spectrum of the eluant confirmed the integrity of the eluted parent complex, **4**. In a second series of experiments, a sample of **4** was loaded onto an anion-exchange column in its Cl form, $P\text{-}NR_3^+Cl^-$. In this case the Ce(IV) polyoxometalate complex was retained on the column. Control experiments were carried out with aqueous solutions of $Ce(SO_4)_2$. As expected, the cerium cations were retained on the cation-exchange column but passed through the anion-exchange column. Consequently, these simple ion-exchange experiments provide good evidence for inner-sphere bonding of the Ce(IV) cations to **3** [33].

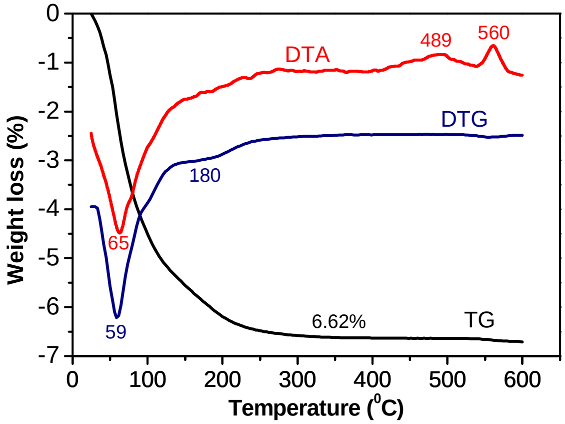

Figure 1. Thermogravimetric and thermodifferential curves of **4**.

UV spectra of the ligand (**3**) and complex (**4**) (Figure 2) show two characteristic absorption bands assigned to the dπ-pπ charge transfer transitions M←O$_t$ (ν$_2$) and M←O$_b$ (ν$_1$) respectively (M is Mo or W; O$_t$ is a terminal oxygen and O$_b$ is a bridging oxygen) [34]. The ν$_1$ band shows a significant red shift in **4** when compared to the monolacunary Dawson ligand. On the other hand, the molar absorption coefficient of the ν$_2$ band, which is proportional to the number of addenda atoms, is almost twice greater in complexes than in the ligand ($\varepsilon \approx 3.46 \times 10^5$ *vs.* 1.76×10^5 L mol^{-1} cm^{-1}), indicating the existence of two monolacunary ligand units in **4** [35].

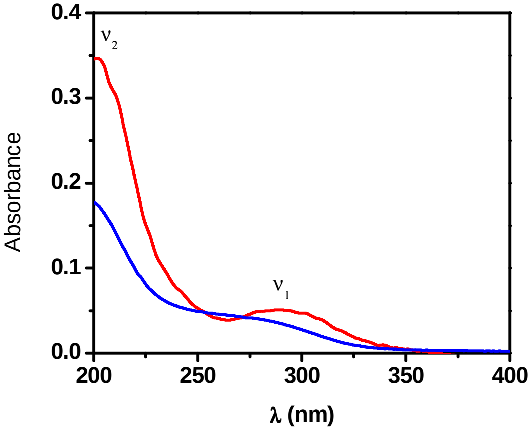

Figure 2. UV electronic spectra of **3** (blue) and **4** (red), recorded in 10^{-6} M aqueous solution.

The ^{31}P NMR spectrum of **4** in D_2O (Figure 3) showed a clean two-line spectrum with signals at -8.27 and -13.22 ppm, confirming its purity and single-product nature. The low-field peak has been assigned to the P(1) phosphorous atom close to the coordination site of Ce(IV) [36-38]. It is easily seen that, the chemical shift of the P2 (remote phosphorus) resonance does not vary greatly in going from the lacunary structure to the Ce(IV) complex. The chemical shift of the P1 (near phosphorus atom) resonance, however, experiences pronounced up field shift upon complexation with Ce(IV).

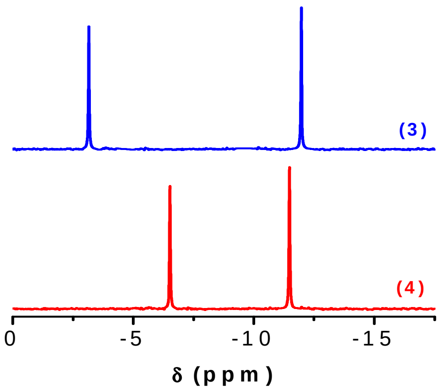

Figure 3. ^{31}P NMR spectrum of **3** and **4** recorded in D_2O

The IR spectrum of **4** (Figure 4) is closely related to that of the parent Dawson monolacunary ligand **3** in the 400-1200 cm^{-1} range, suggesting that the polyoxometalate framework is maintained.

It is well known that the most characteristic changes in the IR spectra of the molybdotungstophosphates, are observed for the P-O stretching vibrations band in the 1000-1200 cm^{-1} range, when comparing the saturated species, lacunary derivatives and their complexes [39]. For instance, when a transition metal cation is added into the vacancy of a monolacunary Dawson polyoxometalate, the whole symmetry of the anion is restored, at least as far as IR spectra are concerned, and the spectra of the transition metal derivatives are very close to the spectrum of complete Dawson anion [36]. A different situation is observed in the case of complexes of monolacunary Dawson polyoxometalate with larger cations (i.e. lanthanides or actinides) which cannot fill the vacancy and therefore coordinate only through the four oxygen atoms that surrounded the addendum vacancy. The IR spectra of such complexes are very close to the spectra of the lacunary Dawson polyoxometalates [27].

As expected, in the spectra of **3** and **4**, the band assigned to P-O asymmetric stretching vibrations is split into three components (1086, 1051 and 1016 cm^{-1}, respectively).

The bands in the 1000-700 cm^{-1} range were assigned to the asymmetric stretching vibrations of the bridges (M-O$_b$-M) and of the terminal bonds (M-O$_t$) [40].

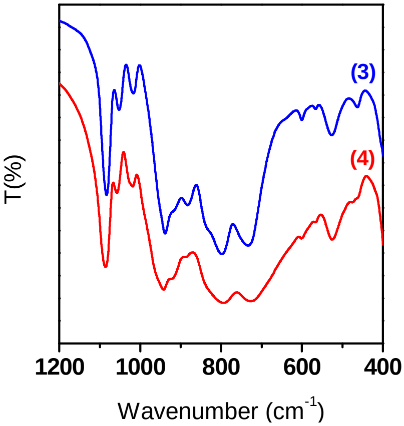

Figure 4. FT-IR spectra of **3** and **4**, recorded in KBr pellets.

On the basis of the analytical and spectral data, a sandwich-type structure is proposed for the Ce(IV) complex **4**. In this structure, the Ce(IV) ion is in a square antiprismatic environment with eight oxygen atoms, four from each of the two monolacunary Dawson ligands, as shown in figure 5.

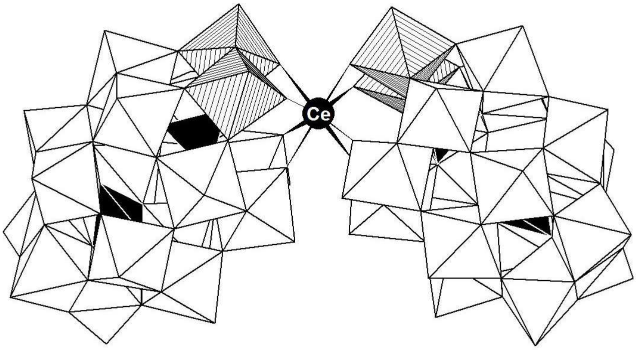

Figure 5. Proposed structure of the polyoxometalate complex **4**.

CONCLUSIONS

A **$K_{16}[Ce(P_2Mo_2W_{15}O_{61})_2]\cdot 34H_2O$** complex was prepared by the reaction of $Ce(SO_4)_2$ with the potassium salt of monolacunary Dawson 2-molybdo-15-tungsto-2-phosphate **$K_{10}[1,2\text{-}P_2Mo_2W_{15}O_{61}]\cdot 18H_2O$** after establishing optimal synthesis conditions. Analytical and spectroscopic data, as well as ion exchange chromatography experiments suggest a sandwich-type structure for the complex, in which the cerium ion is coordinated by four oxygen atoms of the two monolacunary Dawson anions.

EXPERIMENTAL SECTION

Materials

Reagent grade chemicals were used and all syntheses and investigations were carried out in distilled water.

The Dawson precursors $K_6[\alpha\text{-}P_2W_{18}O_{62}]\cdot xH_2O$ (**1**), $Na_{12}[\alpha\text{-}P_2W_{15}O_{56}]\cdot 21H_2O$ (**2**) and $K_{10}[1,2\text{-}P_2Mo_2W_{15}O_{61}]\cdot 18H_2O$ (**3**) were prepared according to the literature [41-43].

Synthesis of $K_{16}[Ce(P_2Mo_2W_{15}O_{61})_2]\cdot 34H_2O$ (4)

A sample of $Ce(SO_4)_2\cdot 4H_2O$ (0.202 g, 0.5 mmol) was dissolved in water (10 mL) and added dropwise, while stirring, to a solution of $K_{10}[1,2\text{-}P_2Mo_2W_{15}O_{61}]\cdot 18H_2O$ (5 g, 1 mmol) dissolved in 110 mL of molar acetic acid – lithium acetate buffer (pH=3.5). The resulting yellow solution was left under stirring for 30 min and then 50 mL saturated solution of KCl was added. A yellow precipitate appeared immediately. After 10 min the resulting yellow precipitate was filtered on a sintered glass frit, washed with ethanol and diethyl ether, and dried in air.

Calcd. for $K_{16}[Ce(P_2Mo_2W_{15}O_{61})_2]\cdot 34H_2O$ P: 1.32; K: 6.69; Mo: 4.10; Ce: 1.50; W: 58.97. H_2O 6.55. Found: P: 1.28; K: 6.72; Mo: 4.02; Ce: 1.44; W: 58,88. H_2O 6.62. FT-IR (polyoxometalate region, cm^{-1}): 1086, 1059, 1018, 943, 924, 889, 796, 725, 602, 565, 526, 474.

Methods

The contents of cerium, phosphorous, molybdenum, and tungsten were determined by inductively coupled plasma atomic emission spectroscopy on a Rigaku Spectro CIROS^{CCD} spectrometer. Potassium was determined by FEP with an Eppendorf flame photometer. The water content was thermogravimetrically determined, by means of a METTLER-TOLEDO TG/SDTA 851 thermogravimeter (Pt crucible, 20 mL/min nitrogen flow, 5ºC/min heating rate).

A JASCO 610 FTIR spectrophotometer was used to record the FTIR absorption spectra in KBr pellets.

UV-Vis spectra were recorded on a Shimadzu UV-3101PC instrument using Teflon-stoppered quartz cells with a path length of 1 cm.

^{31}P-NMR spectra were recorded at 101.2561380 MHz using an ARX 250 spectrometer. Chemical shifts are reported in ppm using D_3PO_4 as external reference.

For the ion-exchange chromathography experiments, degassed water (50 mL) was added to the strongly acidic macroreticular resin (10 g), Vionit CS3 (H~ form; *P*-SO_3H where *P* = macroreticular polymer). The resin was repeatedly washed in water until the aqueous phase was clear and colourless. The resin was then packed into a column (27 cm x 1 cm; length x diameter) and a solution of 4% NaOH was eluted through the column. The resulting *P*-SO_3Na column was washed five times with distilled water (50 ml). A solution of **4** (0.5 g) in H_2O (10 ml), was loaded onto the column. The eluant was collected and the solvent removed by evaporation. The FT-IR spectrum of the collected Ce(IV) complex appeared unchanged when compared with the FT-IR spectrum of the complex before elution. An anion exchange column of identical size was packed with strongly basic resin, Amberlyst A-27 (C1 form; *P*-$NR_3^+Cl^-$). A sample of **4** was loaded onto the column in a manner similar to that described for the cation exchange resin. All samples were retained by the resin, in the upper half of the column.

ACKNOWLEDGMENTS

The authors gratefully acknowledge financial support from the Romanian Program of Research and Development, IDEI (contract No. 329/2007).

REFERENCES

1. M.T. Pope, A. Müller (Eds.), “Polyoxometalates: From Platonic Solid to Antiretroviral Activity”, Kluwer Academic Publishers, Dordrecht, **1994**.
2. M.T. Pope, A. Müller (Eds.), “Polyoxometalate Chemistry: From Topology via Self-Assembly to Applications”, Kluwer Academic Publishers, Dordrecht, **2001**.
3. T. Yamase, M.T. Pope (Eds.), “Polyoxometalate Chemistry for Nano-Composite Design”, Kluwer Academic Publishers, Dordrecht, **2002**.
4. J.J. Borrás-Almenar, E. Coronado, A. Müller, M.T. Pope (Eds.), “Polyoxometalate Molecular Science”, Kluwer Academic Publishers, Dordrecht, **2004**.
5. M. Misono, *Chemical Communications*, **2001**, 1141.
6. I.V. Kozhevnikov, “Catalysts for fine chemical synthesis. Vol. 2. Catalysis by polyoxometalates.”, Wiley & Sons, Chichester, England, **2002**.

7. E. Coronado, C. Giménez-Saiz, C.J. Gómez-García, S.C. Capelli, *Angewandte Chemie, International Edition,* **2004**, *43*, 3022.
8. E. Coronado, P. Day, *Chemical Reviews*, **2004**, *104*, 5419.
9. E. Coronado, C. Giménez-Saiz, C.J. Gómez-García, *Coordination Chemistry Reviews*, **2005**, *249*, 1776.
10. E. Coronado, P. Delhaes, D. Gatteschi, J.S. Miller, “Molecular Magnetism: From Molecular Assemblies to the Devices.”, Kluwer Academic Publishers, vol. E-321, **1996**.
11. J.T. Rhule, C.L. Hill, D.A. Judd, *Chemical Review*, **1998**, *98*, 327.
12. T. Yamase, *Journal of Materials Chemistry*, **2005**, *15*, 4773.
13. T. Yamase, *Chemical Review*, **1998**, *98*, 307.
14. D.E. Katsoulis, *Chemical Review*, **1998**, *98*, 359.
15. J.P. Ciabrini, R. Contant, J.M. Fruchart, *Polyhedron*, **1983**, *2*, 1229.
16. R. Contant, J.P. Ciabrini, *Journal of Chemical Research* (M), **1977**, 2601.
17. R. Contant, *Inorganic Synthesis*, **1990**, *27*, 104.
18. B. Keita, L. Nadjo, R. Contant, *Journal of Electroanalytical Chemistry,* **1998**, *443*, 168.
19. B. Keita, Y. Jean, B. Levy, L. Nadjo, R. Contant, *New Journal of Chemistry* **2002**, *26*, 1314.
20. B. Keita, Y.W. Lu, L. Nadjo, R. Contant, M. Abbessi, J. Canny, M. Richet, *Journal of Electroanalytical Chemistry*, **1999**, *477*, 146.
21. R.D. Peacock, T.J.R. Weakley, *Journal of the Chemical Society A,* **1971**, *A*, 1836.
22. G. Marcu, M. Rusu, A.V. Botar, *Revue Roumaine de Chimie*, **1974**, *19*, 827.
23. G. Marcu, M. Rusu, *Revue Roumaine de Chimie*, **1977**, *22*, 227.
24. G. Marcu, M. Rusu, A. Botar, *Revue Roumaine de Chimie*, **1989**, *34*, 207.
25. J. Bartis,S. Sukal, M. Dankova, E. Kraft, R. Kronzon, M. Blumenstein, L.C. Francesconi, *Journal of the Chemical Society, Dalton Transactions: Inorganic Chemistry*, **1997**, 1937.
26. Q.H. Luo, R.C. Howell, M. Dankova, J. Bartis, C.W. Williams, W.D.Jr. Horrocks, V.G. Young, A.L. Rheingold, L.C. Francesconi, M.R. Antonio, *Inorganic Chemistry*, **2001**, *40*, 1894.
27. A. Ostuni, R.E. Bachman, M.T. Pope, *Journal of Cluster Science*, **2003**, *14*, 431.
28. N. Belai, M.H. Dickman, M.T. Pope, R. Contant, B. Keita, I.M. Mbomekalle, L. Nadjo, *Inorganic Chemistry*, **2005**, *44*, 169
29. C. Zhang, R.C. Howell, Q.H. Luo, H.L. Fieselmann, L.J. Todaro, L.C. Francesconi, *Inorganic Chemistry*, **2005**, *44*, 3569.
30. Q. Wu, E. Wang, J. Liu, *Polyhedron*, **1993**, *12*, 2563.
31. Z.P. Wang, J.Y. Niu, L. Xu, J. Peng, E.B. Wang, *Acta Chimica Sinica*, **1995**, *53*, 757.
32. G. Sun, J. Feng, H. Wu, F. Pei, K. Fang, H. Lei, *Journal of Magnetism and Magnetic Materials*, **2004**, 281, 405.
33. M. Pohl, D.K. Lyon, N. Mizuno, K. Nomiya, R.G. Finke, *Inorganic Chemistry*, **1995**, *34*, 1413.

34. H. So, M.T. Pope, *Inorganic Chemistry*, **1972**, *11*, 1441.
35. D. Rusu, C. Crăciun, M. Rusu, A. Pătruț, L. David, *Revue Roumaine de Chimie*, **2007**, *52*, 817.
36. M. Abbessi, R. Contant, R. Thouvenot, G. Hervé, *Inorganic Chemistry*, **1991**, *30*, 1695.
37. S.P. Harmalker, M.A. Leparulo, M.T. Pope, *Journal of American Chemical Society*, **1983,** *105*, 4286.
38. M.A. Leparulo-Loftus, M.T. Pope, *Inorganic Chemistry*, **1987**, *26*, 2112.
39. J.P. Ciabrini, R. Contant, *Journal of Chemical Research* (M), **1993**, 2720.
40. C. Rocchiccioli-Deltcheff, R. Thouvenot, *Spectrochimica Acta*, **1976**, *32A*, 587
41. C.R. Graham, R.G. Finke, *Inorganic Chemistry*, **2008**, *47*, 3679.
42. B.J. Hornstein, R.G. Finke, *Inorganic Chemistry*, **2002**, *41*, 2720.
43. M. Abbessi, R. Contant, R. Thouvenot, G. Hervé, *Inorganic Chemistry*, **1991**, *30*, 1695.

STUDIA UNIVERSITATIS BABEŞ-BOLYAI, CHEMIA, LIV, 2, 2009

HIGH-THROUGHPUT DETERMINATION OF IVABRADINE FROM HUMAN PLASMA BY LC/MS/MS AND ITS APPLICATION TO PHARMACOKINETIC STUDIES

LAURIAN VLASE[a], DANA MUNTEAN[a],
SORIN E. LEUCUȚA[a], IOAN BÂLDEA[b]

ABSTRACT. A rapid, selective, sensitive and reproducible liquid chromatographic method with mass spectrometric detection (LC-MS/MS) has been developed and validated for the analysis of a bradycardic agent, ivabradine, in human plasma. The samples (0.2 ml) were precipitated using perchloric acid 7% (0.1 ml) and the centrifuged supernatants were injected into HPLC system. Separation and detection of ivabradine were achieved using a C18 column and an MS/MS detector, with a positive electrospray ionization source. The ion transition monitored was 469→(177+262). Ivabradine gave a linear response ranging from 0.49 ng/ml to 49.30 ng/ml. The lower limit of quantification was established at 0.49 ng/ml. The analyte demonstrated good short-term, post-preparative and freeze-thaw stability. The validated method was subsequently applied to a pharmacokinetic study of ivabradine tablets on healthy volunteers.

Keywords: *ivabradine, pharmacokinetics, LC-MS/MS, human plasma*

INTRODUCTION

Ivabradine (3-(3-{[((7S)-3,4-dimethoxi-bicyclo[4.2.0] octa-1,3,5-trien-7-yl) methyl] methylamino} propyl)-1,3,4,5-tetrahydro-7,8-dimethoxy-2H-3-benzazepin-2-one, hydrochloride) (Fig. 1) is a new bradicardic agent. The drug is used for the treatment of myocardial ischemia and supraventricular arrhythmias. Its activity provides pure heart rate reduction at rest and during exercise, which improves myocardial oxygen balance and increases coronary perfusion, without any relevant influence on conduction contractility, ventricular re-polarization and blood pressure [1]. After oral administration, the metabolic clearance of ivabradine accounts for about 80% of its total clearance, with the other 20% corresponding to renal clearance. Only CYP3A4 is involved in invabradine's metabolism, so numerous potential interactions can therefore arise with CYP3A4 inhibitors and inducers [2].

---

[a] *University of Medicine and Pharmacy "Iuliu Hațieganu", Faculty of Pharmacy, Emil Isac 13, RO-400023, Cluj-Napoca, Romania, vlaselaur@yahoo.com*

[b] *"Babeş-Bolyai" University, Faculty of Chemistry and Chemical Engineering, Arany Janos 11, RO-400028, Cluj-Napoca, Romania*

Despite of it's therapeutically benefit, ivabradine has some important side effects, including bradycardia, AV block, ventricular extra systoles and luminous phenomena.

Due to high potential of ivabradine to give adverse reactions on overdosing, but also lack of therapeutic effect on underdosing, it is important to know the way some other substances modify the ivabradine pharmacokinetics [3].

LC-MS has been widely accepted as the main tool in the identification, structure characterization and quantitative analysis of drugs, due to its sensitivity, specificity and efficiency. Ivabradine in plasma was studied by HPLC methods with MS [4] or fluorescence [5] detection, with a sufficient lower limit of quantification for the purpose of study, by applying solid-phase extraction.

The aim of the present study was to develop a fast HPLC-MS/MS method, able to quantify ivabradine in human plasma after oral administration of 10 mg ivabradine, by applying a simple protein precipitation. Finally, the developed and validated method was applied on a pharmacokinetic study on healthy volunteers.

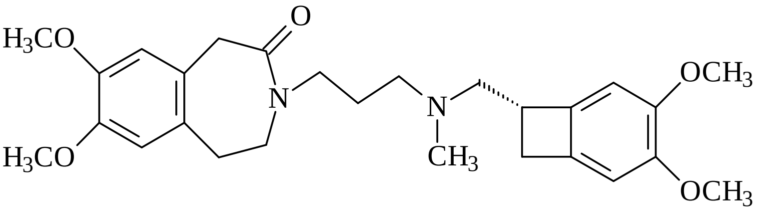

Figure 1. Molecular structure of ivabradine

RESULTS AND DISCUSSION

No significant interference at the retention time of ivabradine (1.5 min) was observed in different plasma blank samples chromatograms (Fig. 2), due to the specificity of the selected signal (Fig. 3)

It is well known that an advantage of the ion trap over the triple quadrupole is the sensibility in the scan mode. This allows adding multiple fragments from an MS spectrum, in order to improve the overall signal. In the case of ivabradine, the sum of ions from MS spectrum (*m/z* 177, 262) was chosen to be quantified, because the detection is more sensitive than in case based only on ion *m/z* 469 (Fig. 3).

The analyte carryover was verified using a blank injection made right after an injection of the most elevated level of concentration from calibration curve. No interference at retention time of analyte due to carryover was observed.

The applied calibration curve model proved to be accurate over the concentration range 0.49 – 49.3 ng/ml, with a correlation coefficient grater than 0.998.

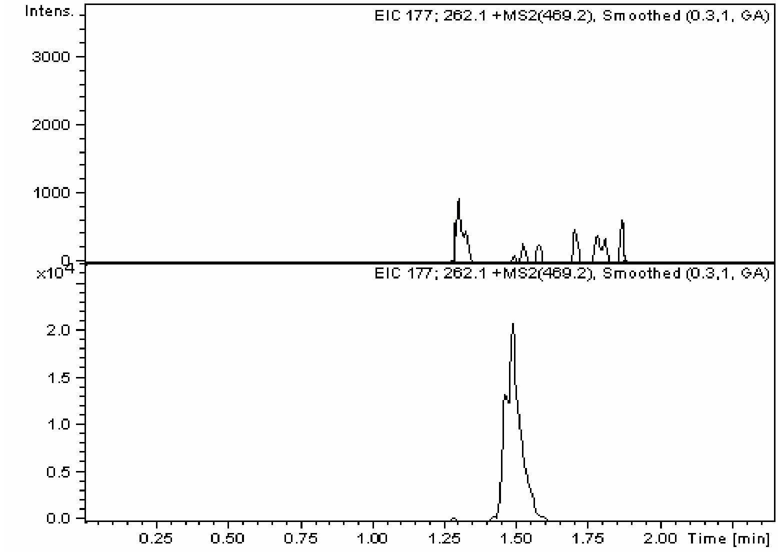

Figure 2. Chromatograms of a plasma blank (up) and LOQ plasma standard with 0.49 ng/ml ivabradine (down)

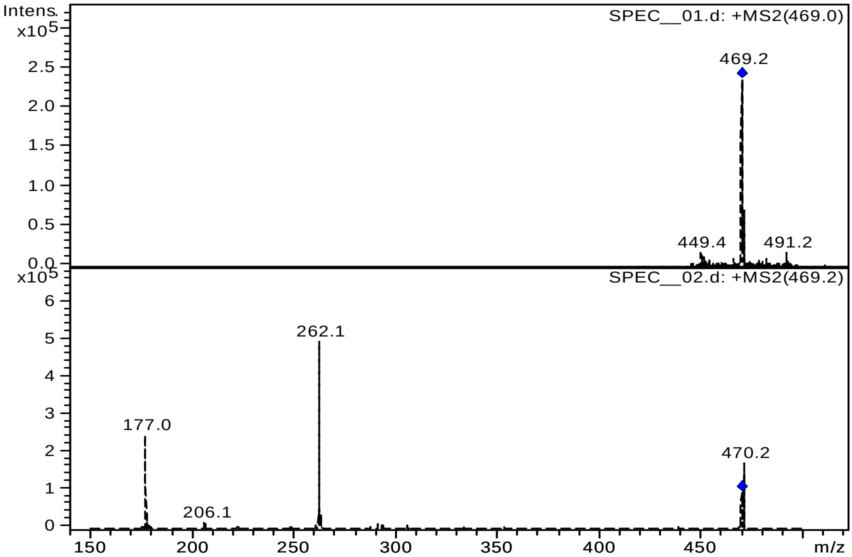

Figure 3. Mass spectra of ivabradine used for its quantification. Full-scan spectrum (up) and MS/MS spectrum (down)

The mean calibration curve y = ax + b, was: y = (76478 ± 4641.3)x – (5217.66 ± 3019.3) N = 8 calibration points, n = 5 determinations for each calibration point. The residuals had no tendency of variation with concentration.

The method had within- and between-run accuracy and precision (Tables 1 and 2), in agreement to the international regulations regarding bioanalytical methods validation [6-8]. The lower limit of quantification (LOQ) was established at 0.49 ng/ml ivabradine, with accuracy and precision less than 20%.

Table 1. Within-run precision, accuracy and recovery for ivabradine (n = 5)

$c_{nominal}$ (ng/ml)	Mean c_{found} (ng/ml) (± S.D.)	C.V. %	Bias %	Recovery % (± S.D.)
0.49	0.45 (0.04)	8	-8.4	92.2 (13.4)
1.48	1.41 (0.08)	5.9	-4.4	99.1 (5.9)
9.86	10.34 (0.36)	3.5	4.9	98.7 (3.5)
29.58	30.78 (2.67)	8.7	4.1	95.9 (8.3)

Table 2. Between-run precision, accuracy and recovery for ivabradine (n = 5)

$c_{nominal}$ (ng/ml)	Mean c_{found} (ng/ml) (± S.D.)	C.V. %	Bias %	Recovery % (± S.D.)
0.49	0.54 (0.05)	9.6	10.1	93.5 (8.8)
1.48	1.47 (0.18)	12.4	-0.3	96.4 (5.0)
9.86	10.38 (0.23)	2.2	5.3	103.0 (7.8)
29.58	30.15 (2.13)	7.1	1.9	98.3 (5.8)

The recovery of the analyte was consistent and reproducible (Table 1). The analyte proved to be stable under various conditions (Table 3), the Bias% of found concentration being less than 15%, the maximum accepted value for method's accuracy.

Table 3. Results of the stability study

	RTS		PPS		FTS	
$c_{nominal}$ (ng/ml)	c_{found} (ng/ml) (± S.D.)	Bias %	c_{found} (ng/ml) (± S.D.)	Bias %	c_{found} (ng/ml) (± S.D.)	Bias %
1.48	1.43	-3.38	1.61	8.78	1.39	-6.08
29.58	30.12	1.83	31.14	5.27	27.21	-8.01

RTS (room temperature stability: 22ºC, 4h); PPS (post-preparative stability: 22ºC, 10 h); FTS (freeze-thaw stability: three freeze thaw cycles)

The validated method was verified during analysis of clinical samples from a study of a medicine containing 10 mg ivabradine. The method continued to perform in terms of accuracy, in each analytical run not more than two out of six QC samples being outside of ±15% nominal value, but not all two at the same concentration. The method was used to analyze about five hundred plasma samples for a pharmacokinetic study. Figure 4 shows concentration profile for ivabradine, after oral administration of a single dose of ivabradine.

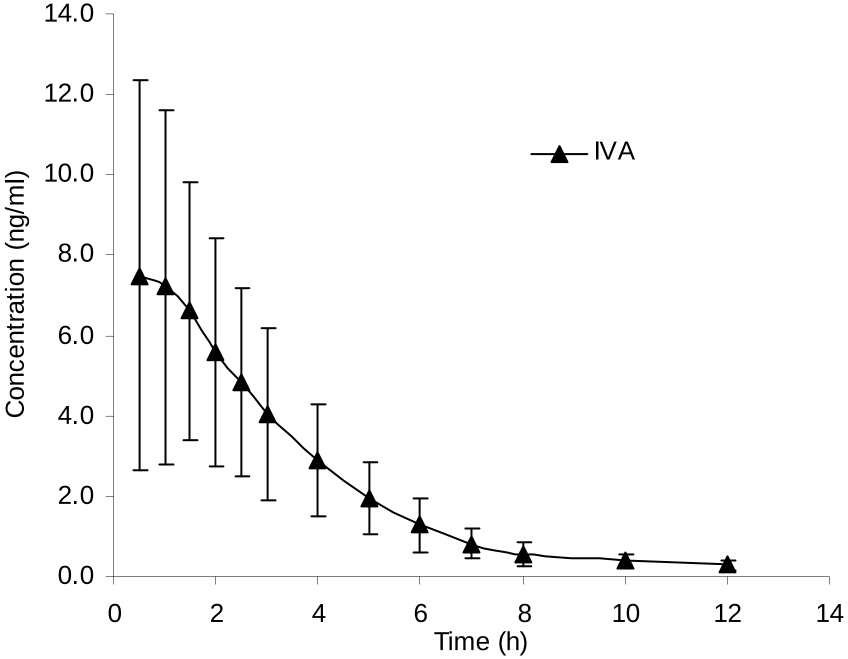

Figure 4. Concentration profile for ivabradine

A comparison to previously published HPLC-MS methods, reveals that the sensitivity of the proposed method (LOQ of 0.49 ng/ml) is quite similar to those in which solid-phase extraction [4,5] was used (Table 4). But the main advantage of our method is the simple sample preparation by protein precipitation, without significant matrix effect. Besides its simplicity makes the method efficient for analysis of a large number of plasma samples (one run is completed within 2 min) and thus it is more productive and cost effective.

CONCLUSIONS

The proposed method provides accuracy and precision for quantitative determination of ivabradine in human plasma, after oral administration of 10 mg ivabradine. The method was validated in accordance with the bioanalytical method validation guidelines and showed good linearity in the studied concentration range. Despite the very simple sample preparation by protein precipitation, the method showed high sensitivity. Another advantage of the method is the short chromatographic runtime of only two minutes. The method was successfully used for ivabradine quantification during a pharmacokinetic study on healthy volunteers.

Table 4. Comparison between analytical characteristics for previously reported HPLC methods used for determination of ivabradine with the proposed method

References	Co-lumn	Detection	Species and matrix	Pretreatment/ extraction	LOQ (ng/ml)	Run Time (min)
A. Portoles et al. [1]	C8	fluorescence	human plasma	SPE	1	?
M. Bouchard et al. [4]	C18	MS/MS	human plasma	SPE	0.1	20
P. Klippert et al. [5]	C8	fluorescence	human plasma	SPE	0.5	20
			dog plasma		0.5	
			rat plasma		0.5	
			human urine		2	
L. Vlase et al.	C18	MS/MS	human plasma	PP	0.49	2

SPE-solid phase extraction; PP-protein precipitation

EXPERIMENTAL SECTION

Reagents

Ivabradine (Fig. 1), methanol, perchloric acid 70% and formic acid were purchased from Merck (Merck KgaA, Darmstadt, Germany). Distilled, deionised water was produced by a Direct Q-5 Millipore (Millipore SA, Molsheim, France) water system. The human blank plasma was supplied by the Local Bleeding Centre Cluj-Napoca, Romania.

Standard solutions

A stock solution of ivabradine with concentration of 0.493 mg/ml was prepared by dissolving the appropriate quantitie of substance (weighted on an Analytical Plus balance from Ohaus, USA) in 10 ml of methanol. A working solution of 49.3 ng/ml was prepared by diluting specific volume of stock solution with plasma. Than this was used to spike different volumes of plasma blank, providing finally eight plasma standards with the concentration ranging between 0.49 and 49.3 ng/ml. Quality control samples (QC) of 1.47, 9.86 and 29.58 ng/ml were prepared by diluting specific volumes of working solution with plasma and were used during clinical samples analysis. A solution of perchloric acid 7% was prepared and used for precipitation of plasma proteins.

Chromatographic and mass spectrometry systems and conditions

The HPLC system was an 1100 series model (Agilent Technologies) consisted in a binary pump, an in-line degasser, an autosampler, a column thermostat and an Ion Trap SL mass spectrometer detector (Bruckner Daltonics GmbH, Germany). Chromatograms were processed using QuantAnalysis Software. The detection of ivabradine was made using an ion trap mass spectrometer with electrospray positive ionisation. The ion transitions monitored was: 469→(177+262). Chromatographic separation was performed at 45ºC on a Zorbax SB-C18 100 mm x 3 mm, 3.5 μm column (Agilent Technologies), protected by an in-line filter.

Mobile phase

The mobile phase consisted of a mixture of water containing 0.2% formic acid and methanol (64:36 v/v), each compartment being degassed before elution for 10 min in an Elma Transsonic 700/H (Singen, Germany) ultrasonic bath. The pump delivered the mobile phase at 1 ml/min.

Sample preparation

Plasma samples were prepared as follows in order to be chromatographically analyzed: in an Eppendorf tube (of max 1.5 ml), 0.2 ml plasma and 0.1 ml perchloric acid solution 7% were added. The tube was vortex mixed for 10 s (Vortex Genie 2, Scientific Industries) and then centrifuged for 6 min at 8000 rpm (2-16 Sigma centrifuge, Osterode am Harz, Germany). The supernatant was transferred to an autosampler vial and 10 μl were injected into the HPLC system.

Validation

As a first step of method validation [6-8], specificity was verified using six different plasma blanks obtained from healthy volunteers who had not previously taken any medication.

The concentration of the analyte was determined automatically by the instrument data system. The calibration curve model was y = ax + b, weight 1/y linear response, where y-peak area and x-concentration. Distribution of the residuals (% difference of the back-calculated concentration from the nominal concentration) was investigated. The calibration model was accepted, if the residuals were within ±20% at the lower limit of quantification (LOQ) and within ±15% at all other calibration levels and at least 2/3 of the standards meet this criterion, including highest and lowest calibration levels.

The lower limit of quantification was established as the lowest calibration standard with an accuracy and precision less than 20%.

The within- and between-run precision (expressed as coefficient of variation, CV%) and accuracy (expressed as relative difference between obtained and theoretical concentration, bias%) of the assay procedure were determined by analysing on the same day five different samples at each of the lower (1.48 ng/ml), medium (9.86 ng/ml) and higher (29.58 ng/ml) levels of the considered concentration range and one different sample of each at five different occasions, respectively.

The recovery of ivabradine was analyzed at each of the three concentration levels mentioned above, e.g. lower, medium and higher level, and also at the quantification limit, by comparing the peack area response of spiked plasma samples with the response of standards prepared in water with the same concentration of ivabradine as the plasma samples, all these prepared as stated in section “Sample preparation”.

The stability of the analyte in human plasma was investigated in three ways, in order to characterize each operation during the process of pharmacokinetic studies: room-temperature stability (RTS), post-preparative stability (PPS) in the autosampler and freeze-thaw stability (FTS). For all stability studies, plasma standards at low (1.48 ng/ml) and high (29.58 ng/ml) concentrations were used. Four plasma standards at each of the two levels were prepared and let at room temperature 4 h before processing (RTS study). Other four pairs were prepared, immediately processed and stored in the autosampler at 25ºC (PPS study). The samples were injected after 10 h, the expected longest storage time of the sample in autosampler before injection. For the freeze-thaw stability, aliquots at the same low and high concentration were prepared. These samples were subjected to three cycles of freeze-thaw operations in three consecutive days. After the third cycle, the samples were analyzed against calibration curve of the day. The requirement for stable analytes was that the difference between mean concentration of the tested samples in various conditions and nominal concentration had to be within ±15% range.

Clinical application and in-study validation

The validated methos was applied in a pharmacokinetic study of tablets containing 10 mg ivabradine. The collected times were: 0, 0.5, 1, 1.5, 2, 2.5, 3, 4, 5, 6, 7, 8, 10, 12 after oral administration of medicine. The accuracy and precision of the validated method was validated to ensure that it continued to perform satisfactorily during analysis of volunteer samples. To achieve this, a number of QC samples prepared at three concentration levels were analyzed in each assay run and the results compared with the corresponding calibration curve. At least 67% (four out of six) of the QC samples should be within 15% of their respective nominal values; 33% of QC (not all at the same concentration) can be outside ±15% of the nominal value.

ACKNOWLEDGMENTS

This work was supported by project PNII-IDEI 462/2007 financed by CNCSIS Romania.

REFERENCES

1. J. A. Portoles, A. Terleira, A. Calvo, I. Martinez, G. Resplandy, *J. Clin. Pharmacol.*, **2006**, *46*, 1188.
2. A. Portoles, A. Calvo, A. Terleira, L. Laredo, G. Resplandy, C. Gorostiaga, A. Moreno, *J. Clin. Pharmacol.*, **2006**, *46*, 1195.
3. Y. M. Di, C. G. Li, C. C. Xue, S. F. Zhou, *Curr. Pharm. Des.*, **2008**, *14(17)*, 1723.
4. M. Francois-Bouchard, G. Simonin, M. J. Bossant, C. Boursier-Neyret, *Journal of Chromatography B*, **2000**, *745*, 261.
5. P. Klippert, J. P. Jeanniot, S. Polve, C. Lefevre, H. Merdjan, *Journal of Chromatography B*, **1988**, *719*, 125.
6. The European Agency for the Evaluation of Medicinal Products. Note for Guidance on the Investigation of Bioavailability and Bioequivalence, London, UK, **2001** (CPMP/EWP/QWP/1401/98).
7. U. S. Department of Health and Human Services, Food and Drug Administration, Center for Drug Evaluation and Research. Guidance for Industry. Bioavailability and Bioequivalence Studies for Orally Administrated Drug Products – General Considerations, Rockville, USA, **2003**, http://www.fda.gov/cder/guidance/index.htm
8. U. S. Department of Health and Human Services, Food and Drug Administration, Guidance for Industry – Bioanalytical Method Validation, **2001**.

STUDIA UNIVERSITATIS BABEŞ-BOLYAI, CHEMIA, LIV, 2, 2009

NANO- AND MICROPARTICLE DISTRIBUTION ON SOLID AND FLEXIBLE SUBSTRATES – PART II

**D. MANCIULA[a, b], S. GRÄTER[c], T. BUREK[d],
I.O. MARIAN[b], B.R.H. MIŞCA[b]**

ABSTRACT. By using the self-assembling process, it is possible to generate a large number of various structural organizations in which individual elements get together into regular patterns under suitable conditions. Two-dimensional self-assembled networks placed on solid and flexible substrates were obtained from solutions containing nano- and micro sized polymer spheres by evaporating the solvent in proper environmental conditions. The entire procedures are uncomplicated and they had been demonstrated as readily reproducible. The parameters used during of the process are as well very easy to control.

Key words: *nanotechnology, self-assembly, nano/microparticles*

INTRODUCTION

Many materials properties change radically at small length scales, because the phenomena, that occur at the nanoscale level can lead to the creation of materials which may display new properties in comparison to the properties they exhibit on a macro scale level. Numerous research fields are able today to study and develop different categories of materials that demonstrate distinctive properties due to their small dimensions. A large interest is focused today on the colloid science, which has given the opportunity to enlarge the number of materials with practical relevance in the field of nanotechnology. Some of the most common nanotechnological applications of different types of nano- and micro scaled materials consist of particle insertion in cosmetics, food products, paints and different categories of plastic materials, which can be used for instance in food packaging, cloth making or for coating various surfaces and furthermore for producing various types

---

[a] *Faculty of Environmental Sciences, Babeş-Bolyai University, Cluj-Napoca, Romania; Fantanele Street, Nr. 30; 400294; Tel.: 0264-307030; Fax: 0264-307032; e-mail: dimro21@googlemail.com*

[b] *Faculty of Chemistry and Chemical Engineering, Babeş-Bolyai, University, Cluj-Napoca, Romania; Arany-Janos Street, No.11,400028; Tel: +40 264-593833; Fax: +40 264-590 818*

[c] *Biophysical Chemistry Department, Combined Faculties for the Natural Sciences and for Mathematics of the Ruperto-Carola University of Heidelberg, Germany*

[d] *New Materials and Biosystems Department, Max-Planck Institute, Stuttgart, Germany*

of surfaces, fuel catalysts and also disinfectants [1, 2]. Within this paper are presented several methods, which were used to obtain two-dimensional self-assembled networks placed on flexible substrates from solutions containing nano- and micro sized polymer spheres.

RESULTS AND DISCUSSION

Self-assembly is considered the basic principle which generates spontaneous and reversible structural organizations, in which fractions or disordered components of a primary system form organized structures or patterns. The colloidal particle integration sequence into defined flexible constructions is also based on the self-assembly approach. The mimicking procedure of molecular self-assemblies and as well the integration of nanoparticles into clusters are based in general on van der Waals forces [6], electrostatic interactions [3], hydrogen bonding [3], dipole–dipole interactions [3] and capillary forces [4].

The transfer of polystyrene microbeads to the PDMS (polydimethylsiloxane) film has generated a non-closely-packed monolayer on the PDMS surface, showing good results for relatively large-sized microspheres (1-3 µm), due to the fact that the spheres sink into the polymer film during the process (Figure 1).

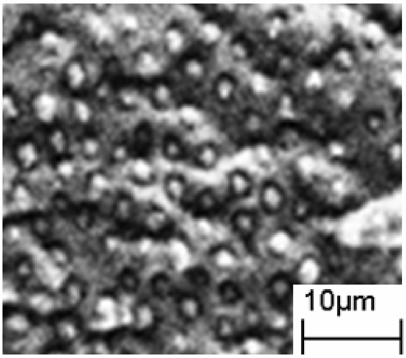

Figure 1. Polystyrene microbeads partially sunk into the PDMS film

This technique however did not yield good results when using small-sized microbeads (200-800 nm), because they do not behave in the same manner. These beads also sink into the PDMS film, but are incapable of maintaining a homogenous plane level (Figure 2).

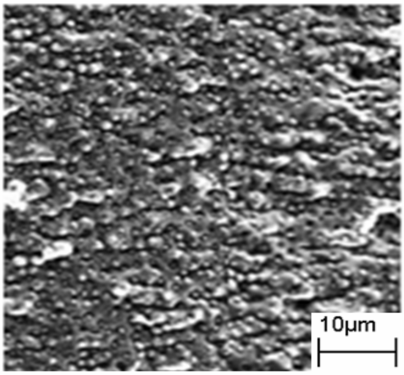

Figure 2. Polystyrene nanospheres transferred onto the PDMS film

A major disadvantage for this approach is that the stability of the spheres is relative, even for large-sized microbeads sunk into the PDMS film. Particularly when the structure is bent, some of the microbeads jump off the film leaving the surface filled with holes (Figure 3).

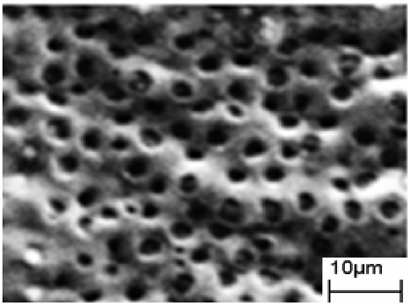

Figure 3. Polymer surface filled with holes after microbeads jumping

Through the dipping technique, a well-distributed monolayer of highly ordered, hexagonal closely-packed microbeads can be generated. The dipping speed has a strong influence over the monolayer formation and as a result a high dipping speed may lead to a multilayer deposition over the substrate, while a lower dipping speed might not be adequate enough for generating a close-packed monolayer. The main disadvantage of this process is that it requires a relatively long time (few hours) to complete for larger flexible probes (40-50 cm foils) and large volumes (depending of the sample characteristics) of suspensions. Another drawback to this technique is that the microspheres will deposit themselves along both sides of the substrate and not only on the substrate itself, as well as on the walls of the beaker, leading to a waste of material, especially problematic for expensive suspensions.

For the situation of particle self-assembling by means of suspension evaporation within the heating oven, the structure of the self-assembled aggregate depends on the rate of solvent evaporation. A slow evaporation of the solvent leads to ordered colloidal crystals. By tilting the substrates, the gravity acts as an additional force affecting the template and influencing the arrangement of the particles. Temperature plays as well a significant role in the monolayer formation process. As temperature decreases, the preference of the surface for the microbeads increases, due to the diminution of the thermal disorder in the forming monolayer. As a result, a cold liquid suspension was used to ensure a good distribution and a proper formation of the monolayer assembly. All substrates free of impurity were used immediately after they were cleaned.

CONCLUSIONS

Two-dimensional self-assembled networks and configurations made of nano- and micron-sized polymer spheres may be simply obtained from a solution which contains the polymer microspheres. Ordered configurations were obtained after the solvent evaporation under proper experimental conditions, or by transferring the spheres onto a thin flexible polymer film. The self-assembly procedure can be easily influenced by several parameters (e.g. temperature, dipping speed, vibrations) and as a consequence the sensitivity to environmental perturbations may lead to visible changes in the final structure or even compromise it. By using small amounts of materials and uncomplicated mechanical setups, these methods are very easy to use and the experimental parameters simple to control without requiring special working conditions. The substrate immersion into the colloidal solution is considered the best technique for generating a well ordered monolayer.

EXPERIMENTAL SECTION

The nano- and microparticle distribution onto flexible substrates was possible by using several experimental techniques. The first method used was the microbead transfer from a solid substrate to a flexible substrate.

1. The microbead transfer technique to a polymer (PDMS) film

For generating a non-closely-packed monolayer, the lift-up soft lithography technique [5] was used, in which a single layer of microspheres was transferred from a normal glass substrate onto the surface of a PDMS (polydimethylsiloxane) polymer film [6] (Figure4).

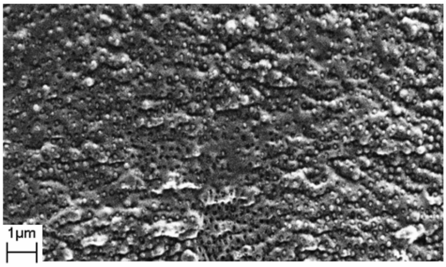

Figure 4. Microbeads transferred to a PDMS film

2. Substrate immersion inside a colloidal solution

Another way to generate the monolayer is to dip the flexible substrate into a colloidal solution and then remove it at a constant speed. In such a case, a perfect, well-distributed monolayer of highly ordered, hexagonally packed microbeads is formed over the surface (Figure 5).

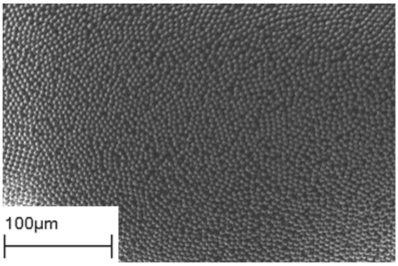

Figure 5. Uniform monolayer of polymer microbeads

3. The microbead deposition to a flexible polymer foil

For generating a two-dimensional monolayer on the flexible substrate (polymer foil), the solvent first was evaporated by using a heating oven (60℃ for 10h). The results can be seen in figure 6.

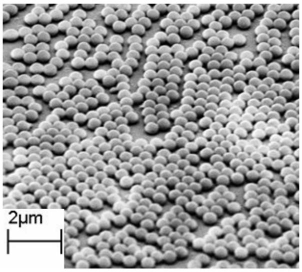

Figure 6. 2-D monolayer on a flexible polymer substrate by evaporating the solvent in a heating oven

Next was applied a solvent evaporation at room temperature (24h) by tilting the flexible substrates at a small angle (2-15°) between the normal surface and to the gravity, to induce particle arrangement (Figure 7). In this case to prevent the foil curving, the flexible material was held on a solid support (glass microscope slide or a polystyrene Petri dish).

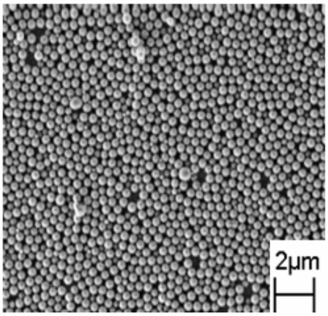

Figure 7. 2-D monolayer on a flexible polymer substrate by evaporating the solvent at room temperature

For the previous mentioned techniques, the following materials were utilized: microscope slides: 76x26 mm; cover-slips: 20x20mm; 24x24mm; 24x50mm; solvent: toluene; polyester (PET) foil; nanobeads and microspheres made of: poly (MMA), 200 nm, poly(styrene-co-MMA), 200 nm with 80% MMA and 20% styrene, polystyrene 1µm and polystyrene microspheres (Polysciences Inc.) with the following dimensions and concentrations presented in the table bellow (Table 1). The glass transition temperature for the polystyrene spheres it is in the temperature range of 95 °C – 105 °C. [7]

Table 1. Polystyrene microspheres used during experiments

Diameter µm	**Concentration %**		
0.202	2.56	2.61	2.67
0.465	2.62	2.65	
0.477	2.69		
0.495	2.66		
0.987	2.54		
0.989	2.60	2.69	
1.091	2.76		
1.826	2.70		
5.658	2.65		

REFERENCES

1. H.M. Peter, B.H. Irene, V.S. Oleg, *J. Nanobiotechnology*, **2004**, *2*, 12.
2. F. Buentello, D. Persad, B. Erin, M. Douglas, S. Abdallah, P. Singer, *PloS Medicine,* **2005**, *2*, 300.
3. Y. Xia, G.M. Whitesides, *Soft lithography, Annual Review of Material Science*, **1998**, *28*, 153.
4. M.J. Madou, Fundamentals of microfabrication, CRC Press, New York, 2nd Ed., **2000**, 20, ISBN: 0849394511.
5. D. Manciula, Nano- and micro-structured polymer surfaces, Combined Faculties for the Natural Sciences and for Mathematics of the Ruperto- Carola University of Heidelberg, Germany, PhD thesis, 4th April, **2007**, 10.
6. J. C. McDonald, D.C. Duffy, J.R. Anderson, D.T. Chiu, H. Wu, O.J. Schueller, G. M. Whitesides, *Electrophoresis*, **2000**, *21*, 27.
7. D. Manciula, I.O. Marian, B.R.H. Mişca, *Studia Universitatis Babeş-Bolyai, Chemia*, **2008**, *1*, 48.

STUDIA UNIVERSITATIS BABEŞ-BOLYAI, CHEMIA, LIV, 2, 2009

APPLICATION OF THE RUTHENIUM-CATALYZED OXIDATIVE CLEAVAGE OF OLEFINS TO THE ALDEHIDES IN THE SYNTHEIS OF (S)-14-METHYL-1-OCTADECENE, THE SEX PHEROMONE OF *Lyonetia clerkella*

STEFANIA TOTOS[a,*], IOAN OPREAN[a], MONICA BUCSA[a]

ABSTRACT. The synthesis of (14S)-methyl-octadec-1-ene, the sex pheromone of peach leafminer moth *Lyonetia clerkella* is described using a new protocol for the oxidative cleavage of the olefin **4**.

Key words: Oxidative cleavage / Ruthenium catalyst / Pheromone

INTRODUCTION

The peach leafminer, *Lyonetia clerkella* (Linaeus), is distributed in Japan, South Korea, Taiwan, China, India, Europe, and Madagascar. Infestation by this insect causes almost complete defoliation of the trees and reduces cropping and fruit production potential for the future, which typically affects to fruit trees such as apple, pear, cherry, plum, quince and peach.

Sugie *et al.* identified the sex pheromone of the moth as 14-methyl-1-octadecene **1**[1]. To establish the absolute configuration of the natural pheromone, Kato and Mori developed two synthetic routes to the enantiomers of **1** starting from the enantiomers of methyl-β-hydroxyisobutyrate[2] and from (R)-citronellic acid[3]. Biological tests with these synthesized compounds showed that the natural pheromone is (S)-14-methyl-1-octadecene, and that there is no antagonistic activity of the (R)-enatiomer.

RESULTS AND DISCUSSIONS

During the last years, various strategies have been developed for the synthesis of **1**[4-7]. In this paper we described a new protocol for the synthesis of (14S)-methyl-1-octadecene **1** starting from (R)-citronellic acid (Scheme 1). Our procedure is based on the known literature method[3], and the key step was the oxidative cleavage of olefin **4** to aldehyde **5**.

---

[a] *"Babes-Bolyai" University, "Raluca Ripan" Institute for Research in Chemistry, 30 Fantanele str., 400294, Cluj-Napoca, Romania*

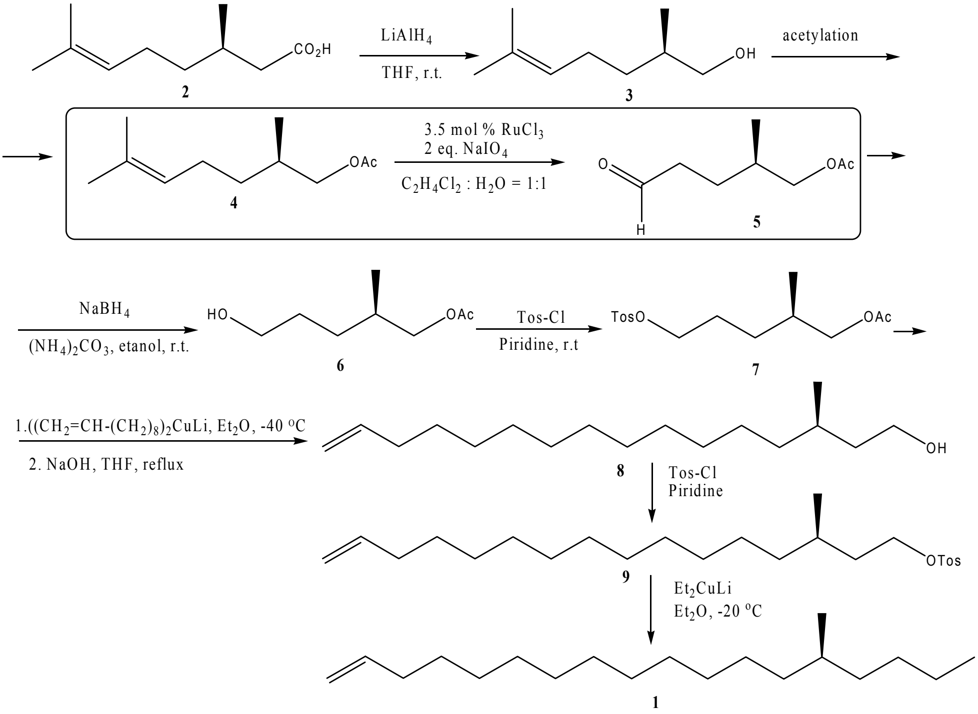

Scheme 1

To obtain aldehyde **5** from the olefin **4**, K. Mori *et al.* have used the ozonization of the olefin followed by a reductive workup[3] (ozone was bubbled through the stirred and cooled mixture at -70 °C), the compound **5** being obtained in 60 % yield. For the sake of safety and convenience, a great deal of efforts have been directed at developing alternative methods to cleave olefins to aldehydes, especially in a catalytic manner. D. Yang and C. Zhang have developed three ruthenium-based catalytic oxidation methods for the cleavage of a wide range of olefins to aldehydes[8]. The oxidative cleavage of olefin **4** to aldehyde **5** involved the use of ruthenium trichloride as catalyst (3.5 mol %), sodium periodate as terminal oxidant and two immiscible liquid phases, *i. e.*, 1,2-dichloroethane and water, as the solvent system. The yield of **5** was 53 % after purification by column chromatography. This new protocol represents a very useful alternative for the ozonolysis of olefins followed by a reductive workup, since $RuCl_3$ is easy to handle, is not expensive and the reaction proceeded under mild conditions at room temperature.

Having the key derivative **7** in hand, the next step was the synthesis of **8** by treatment of **7** with di(9-decenyl)-cuprate and the resulting product was submitted to alkaline hydrolysis to give **8** in 60 % yield. The second-elongation was made by treatment of the tosylate **9** with lithium diethylcuprate yielding (S)-**1**.

CONCLUSIONS

In summary, we prepared (14S)-methyloctadec-1-ene **1**, the overall yield for the all steps being 28%. All the data recorded for our synthetic sample of **1** matched those reported in the literature[3].

EXPERIMENTAL SECTION

^{1}H-NMR (500 MHz) spectra were recorded at *rt* in C_6D_6 on a Bruker 500 MHz spectrometer, using the solvent line as reference. Electron impact (70 eV) mass spectra were obtained on Hewlett-Packard MD 5972 GC-MS instrument. GC analyses were performed on a Hewlett-Packard HP 5890 gas chromatograph. A HP-5MS capillary column (30 m x 0.25 mm x 0.33 µm) and helium gas were used for separations.

General procedure for the oxidative cleavage of 4:

To a stirred mixture of olefin **4** (5 mmol, 1.0 g) and $RuCl_3$ (0.175 mmol, 3.5 mol%, 36.3 mg) in 1,2-dichloroethane (25 ml) and distilled water (25 ml) was added in portions $NaIO_4$ (10 mmol, 2.14 g) over a period of 5 min. at room temperature. The color turned from black to yellow immediately. The reaction was monitored by TLC. After completion in 8 h, the reaction mixture was quenched with saturated aqueous solution of $Na_2S_2O_3$, and the two layers were separated. The aqueous layer was extracted with EtOAc three times. The combined organic layer was washed with water and brine, respectively, dried over anh. $MgSO_4$, filtered, and concentrated. The residue was purified by column chromatography (EtOAc : *n*-hexane = 2 :3) to give the desired aldehyde **5** as a colorless oil (0.5 g, 53%). ^{1}H NMR (500 MHz, C_6D_6, δ ppm): 0.68 (d, 3 H, J = 6.5 Hz, 3-CH_3), 1.08-1.47 (m, 7 H), 1.81 (s, 3 H, -COCH_3), 4.01-4.10 (m, 2 H, -CH_2-O-), 9.38 (s, 1 H, C*H*O); ^{13}C NMR (125 MHz, C_6D_6, δ ppm): 18.79, 20.34, 28.50, 29.26, 35.20, 41.09, 62.24, 169.94, 200.37; GC: R_t = 19.56 min; MS: *m/z* 129 (2 %) $[M – COCH_3]^+$, 43 (100 %) $[COCH_3]^+$.

REFERENCES

1. Sugie H., Tamaki Y., Sato R., Kumakura M., *Appl. Entomol. and Zool.*, **1984**, *19*, 323.
2. Kato M., Mori K., *Agr. Biol. Chem.*, **1985**, *49*, 2479.
3. Kato M., Mori K., *Liebigs Ann. Chem.*, **1985,** 2083.

4. Sonnet, P. E., Proveaux A. T., Adamek T., Sugie H., Sato R., Tamaki Y., *J. Chem. Ecol.*, **1987**, *13*, 547.
5. Yamamoto A., Fukumoto T., *Agric. Biol. Chem.*, **1989**, *53*, 1183.
6. Kharisov R. Ya, Latypova E. R., Talipov R. F., Muslukhov R. R., Ishmuratov G. Yu., Tolstikov G. A, *Russ. Chem. Bull., Int. Ed.,* **2003**, *52*, 2267.
7. Reyes E., Vicario J. L., Carrillo L., Badia D., Uria U., Iza A., *J. Org. Chem.*, **2006**, *71*, 7763.
8. Yang D., Zhang C., *J. Org. Chem.*, **2001**, *66*, 4814.

STUDIA UNIVERSITATIS BABEŞ-BOLYAI, CHEMIA, LIV, 2, 2009

MICROWAVE-ASSISTED SYNTHESIS OF PHENOTHIAZINE SULFOXIDE DERIVATIVES

LUIZA GĂINĂ, MIHAI SURDUCAN, CASTELIA CRISTEA* AND LUMINIȚA SILAGHI-DUMITRESCU

ABSTRACT: Microwave assisted oxidation of 10-alkyl-phenothiazine derivatives with copper(II) nitrate selectively generated phenothiazine-sulfoxides in very short reaction times (1-2 minutes). Best results were obtained by dry media procedure using silica gel solid support, a fact which opens a path for environmentally safe procedures envisaged by green chemistry. The structure of the products was assigned by IR and high resolution NMR spectroscopy.

Keywords: *10-alkyl-phenothiazine-sulfoxides*, *copper(II) nitrate oxidizing agent*, *Microwave assisted organic synthesis (MAOS)*

INTRODUCTION

Various oxidation products of phenothiazine were obtained when a wide range of chemical oxidants were employed (hydrogen peroxide, potassium permanganate, nitric acid, potassium hypochlorite, chromic anhydride, sodium nitrite, etc. [1]. As shown in scheme 1, the phenazathionium cation formed by the loss of 2 electrons and a proton from the parent heterocycle may be considered as a key intermediate in the formation of oxidized products. Formal hydration of the cation quinoid structure by addition of water may proceed at C-3, at S or at N, thus yielding 3H-phenothiazin-3-one **1**, phenothiazine 5-oxide **2** and phenothiazine nitroxyl **3** respectively [2].

Hydrogen peroxide was extensively used as an effective reagent for the synthesis of phenothiazine-5-oxide **2** derivatives, but the excess amounts of this reagent produces phenothiazine 5,5-dioxide derivatives [3-5].

Phenothiazine 5-oxide **2**, was obtained selectively and in good yields in the presence of alkyl-hydroperoxides [6], but poor yields were observed when electron withdrawing substituents were attached to the heterocyclic substrate. N-alkyl- phenothiazine-5-oxide derivatives were also successfully prepared using *m*-chloroperbenzoic acid [7].

---

* *Universitatea Babeş-Bolyai, Facultatea de Chimie şi Inginerie Chimică, Str. Kogălniceanu, Nr. 1, RO-400084 Cluj-Napoca,Romania, castelia@chem.ubbcluj.ro*

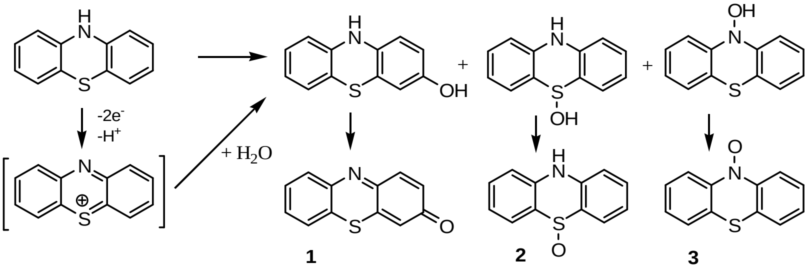

Scheme 1.

Nitric acid can be used as an oxidizing agent for phenothiazine sulfoxide preparation [7,8], but competitive substitution may occur in position 3 of the phenothiazine substrate. Catalytic autooxidation of N-alkyl-phenothiazine derivatives in the presence of nitroxides (NO_2, $NOBF_4$) or HNO_2 selectively generates phenothiazine-5-oxide derivatives [9]. Compounds containing pyrazolines, enones and oxo functional groups attached to phenothiazine core unit, were selectively transformed into sulfoxides by the effect of ultrasound-promoted oxidation with copper(II) nitrate [10]; this method generated high yields of sulfoxides (sometimes reaching 95%), irrespective of the ring substituents, in relatively short reaction times.

The aim of this work was to test the efficiency of microwave assisted organic synthesis (*MAOS*) techniques in the preparation of phenothiazine sulfoxides by the oxidation of phenothiazine substrates with copper(II) nitrate and to compare this technique with the previously reported ultrasound-promoted oxidation, having in view that *MAOS* technique may afford certain advantages such as shorter reaction times and sometimes higher reaction selectivity [11,12]. An increasing need for less hazardous reaction conditions and environmentally safe procedures, or green chemistry, guided the chemical synthesis towards solvent free reactions approach, highly reproducible under *MAOS* techniques.

RESULTS AND DISCUSSIONS

In order to ensure a high reproducibility of our experiments the technique applied is based on microwave power processing of materials using a microwave installation *Synthos 3000* equipped with temperature and pressure sensors, built-in magnetic stirrer, cooling mechanisms, power control and software operation.

According to the sample preparation, several methods have been developed for operating microwave-assisted syntheses: reactions in the presence of solvent (in solution phase or polymer-supported solid phase), or solvent-free syntheses (which fall into three categories: reactions with neat reactants, reactions under phase transfer catalysis and reaction mixtures adsorbed onto inorganic supports). Microwave-assisted selective oxidation of sulfides to sulfoxides and sulfones was studied by Varma and co-workers, who employed different oxidants on supported mediums in solvent free reaction environments (such as wet silica-supported sodium periodate [13], or copper(II)nitrate on clay-hidrogen peroxide [14]).

Oxidation with copper(II) nitrate was applied to several 10-alkyl-phenothiazines and found that S-oxidation took place selectively resulting in sulfoxides irrespective of the ring substituents (scheme 2). On the effect of the "*in situ*" generated nitrogen-dioxide [15] oxidation of heterocyclic sulfur atom occurred, leading to sulfoxides in good to high yields. The reaction can be induced by conductive heating, ultrasounds promoted or microwave assisted.

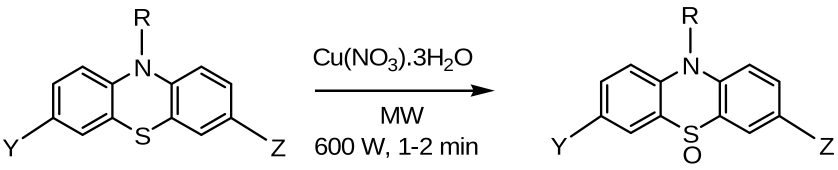

4 R= -Me, Y= Z = -H
5 R= -Me, Y= H Z= -CHO
6 R= -Me, Y= Z= -CO-CH_3

Scheme 2

Under thermal procedure, 10-methyl phenothiazine afforded 78% yield of 10-methyl-phenothiazine-5-oxide after 3 hours at 40 ^oC, but sonication accelerated the oxidation in such a way that 90% yields were obtained after 45 minutes of sonication at room temperature [10]. A direct comparison between the microwave assisted and the ultrasound promoted oxidation reaction can be considered by using the same reaction mixture and changing the source of energy. Two microwave-assisted methods were selected for the sample preparation: i) synthesis in the presence of solvent and ii) solvent free synthesis using reaction mixture adsorbed onto inorganic supports. Table 1 summarizes the results obtained in the microwave assisted oxidation of 10-alkylphenothiazine derivatives with copper(II) nitrate, in comparison with sonication data.

Dichloromethane solvent employed in the sonication experiments is a low microwave absorbing solvent (dielectric loss value 0.382 [16]) and moderate reaction yields were obtained when this solvent was employed in the microwave assisted oxidation (Table 1).

Table 1. Microwave assisted *versus* sonication data obtained for the oxidation of 10-alkylphenothiazine derivatives with copper(II) nitrate.

Cpd.	MAOS					Sonication [10]	
	Power [W]	DCM solution		SiO_2 solid support			
		T [min]	Yield [%]	T [min]	Yield [%]	T[min]	Yield [%]
4	600	2	65	1	90	60	95
5	600	2	35	1	60	60	90
6	600	2	43	4	60	60	85
7	600	2	33			60	86
8	600	2	23			60	70
9	600	2	42			60	80

The oxidation of phenothiazine derivatives was also performed in dry media conditions using adsorbed reagents on solid support, a procedure which reduces the amount of solvent used and minimize potentially hazardous reactions (dichloromethane and chloroform can generate highly toxic products HCl, CO, CO_2 and phosgene, due to prolonged exposure to high temperatures). Two different support materials were tested: alumina (which can act as a base) and silica gel (which can act as an acid). *MAOS* on solid support required only 1 minute of irradiation to yield 90% phenothiazine-sulfoxide on silicagel. On the contrary, phenothiazine-5-oxide derivatives were not obtained when Al_2O_3 was employed as solid support.

In compound **6** the formyl group was not affected by oxidation in the *MAOS* conditions employed. Satisfactory results were obtained for the oxidation of 10-methyl-3,7-diacetyl-phenothiazine, which may be considered as a substrate resistant to oxidation. 10-Alkyl-phenothiazinyl-enones were subjected to the same oxidizing conditions (scheme 3) and S-oxidation occurred in lower yields in the case of *MAOS* as compared to sonication.

7 R= -Me, Ar= *m*-NO_2-C_6H_4
8 R= -Me, Ar= *p*-OMe-C_6H_4
9 R= -Me, Ar= 2-$C_{10}H_7$

Scheme 3

Structural assignments of sulfoxides **4-10** were based on FTIR and ^{1}H-NMR spectra. In the IR spectrum of **4-10** a very intense absorption band due to SO stretching vibration (ν_{SO}) appears situated at 1020-1025 cm^{-1}. The electron withdrawing SO group induced an important deshielding upon neighboring atoms, mainly proton and carbon atoms in positions 4,6 of the heterocyclic structure (for example in the structure of compound **4,** $\delta_{H4,6}$=8.58 ppm).

10*H*-phenothiazin-5-oxide could not be obtained by microwave assisted oxidation of 10*H*-phenothiazine with $Cu(NO_3)_2$, neither in DCM solution, nor in solvent free conditions.

CONCLUSIONS

The oxidation with copper(II) nitrate represents an advantageous method of preparation for 10-alkyl-phenothiazine-sulfoxides, due to its chemo-selectivity and potential to produce sulfoxides in high yields. Comparable results were obtained when sonication and microwave assisted synthesis were applied. Advantages of *MAOS* lie on very short reaction times (1-2 minutes). Best results were obtained by *MAOS* on silica gel solid support, a fact which opens a path for environmentally safe procedures envisaged by green chemistry.

EXPERIMENTAL SECTION

Microwave installation *Synthos 3000 Anton Paar*
300 MHz *Brucker* NMR spectrometer
Brucker Vector 22 FT-IR spectrometer
Reagents from *Merck* were used.
TLC was used to monitor the reaction progress (Merck silica gel F 254 plates).

General procedure for microwave assisted oxidation

i) in dichloromethane solution

The 10-alkyl-phenothiazine derivative (1 mmol**)** and $Cu(NO_3)_2x3H_2O$ (0.726 g, 3 mmol) were dissolved in DCM (20 cm^3). The reaction mixture was irradiated for 1-2 min (table 1) using power settings 600W. The reaction was monitored by TLC. After completion, the reaction medium was filtered and the solid was washed with DCM (2 x 20 cm^3). After evaporation the residue obtained was purified by column chromatography on silica using DCM-MeOH (15-1) as eluent and re-crystallised from EtOH.

ii) on silica gel solid support

The 10-alkyl-phenothiazine derivative (1 mmol**)** was dissolved in DCM (20 cm^3), 1g silica gel was added and the solvent was evaporated to dryness under vacuum. The solid product was mixed with $Cu(NO_3)_2x3H_2O$ (3 mmol). The reaction mixture was irradiated for 1-2 min (table 1) using power setting 600W. The reaction product was extracted in DCM. After evaporation the residue obtained was purified by column chromatography on silica gel using DCM-MeOH (15-1) as eluent and re-crystallised from EtOH.

10-Methyl-10*H*-phenothiazine-5-oxide 4
White powder; mp 187-189 °C (lit.: 193 °C [17])
IR (cm^{1}): 2085, 1584, 1457, 1261, 1020, 765
^{1}H-RMN, $CDCl_3$: δ(ppm) =3.79 (s, 3H); 7.27 (*t*, 2H); 7.40 (*d*, 2H); 7.64 (*t*, 2H); 7.95 (*d*, 2H).

3-Formyl-10-methyl-10*H*-phenothiazine-5-oxide 5
Yellow powder; (0.232 g, 90%); mp 205-207 °C; (lit. : 207-208 °C)
IR (cm^{1}): 2090, 1682, 1605, 1462, 1260, 1046, 1025, 764, 751
^{1}H-RMN, $CDCl_3$: δ(ppm) =3.80 (*s*, 3H); 7.34 (*t*, 1H); 7.46 (*m*, 2H); 7.65 (*t*, 1H); 7.94 (*d*, 1H); 8.08 (*d*, 1H); 8.39 (s, 1H); 9.97 (s, 1H).

3,7-Diacetyl-10-ethyl-10*H*-phenothiazine-5-oxide 6
Yellow powder; (0.278 g, 85%); mp 259-262 °C;
IR (cm^{1}): 2085, 1674, 1589, 1479, 1249, 1024, 826.
^{1}H-RMN, $CDCl_3$: δ(ppm) =2.68 (s, 6H); 4.45 (s, 3H); 7.58 (*d*, 2H); 8.29 (*d*, 2H); 8.58 (*s*, 2H).

(*E*)-10-Methyl-3-[1-(3-nitrophenyl)-1-oxo-2-propen-3-yl]-10*H*-phenothiazine-5-oxide 7
Yellow powder; (0.348 g, 86%); 201 -204 °C
IR (cm^{1}): 1656, 1586, 1466, 1218, 1021, 813, 754.
^{1}H-RMN, $CDCl_3$: δ(ppm) =3.80 (s, 3H); 7.29 (m, 3H), 7.54 (d, 1H), 7.64 (m, 1H), 7.7 (t, 1H), 7.9 (m, 3H), 8.22 (s, 1H), 8.6 (d, 2H), 8.81 (s, 1H).

(*E*)-10-Methyl-3-[1-(4-methoxyphenyl)-1-oxo-2-propen-3-yl]-10*H*-phenothiazine-5-oxide 8
Yellow powder; (0.272 g, 70%); 237 -241 °C;
IR (cm^{1}): 1654, 1602, 1585, 1463, 1259, 102o, 834, 805.
^{1}H-RMN, $CDCl_3$: δ(ppm) =3.78 (s, 3H); 3.90 (s, 3H); 6.99 (d, 2H); 7.31 (d, 1H); 7.4 (m, 2H); 7.56 (d, 1H); 7.65 (t, 1H), 7.83(m, 2H), 7.96 (d, 1H); 8.06 (d, 2H), 8.21 (s, 1H).

(*E*)-10-Methyl-3[1-(2-naphthyl)-1-oxo-2-propen-3-yl]-10*H*-phenothiazine-5-oxide 9
White powder; (0.327 g, 80%); 225-226 °C
IR (cm^{1}): 1654, 1586, 1465, 1261, 1020, 810, 747
^{1}H-RMN, $CDCl_3$: δ(ppm) =3.78 (s, 3H); 7.33 (t, 1H); 7.41 (m, 2H); 7.66 (t, 1H); 7.73 (d, 1H); 7.9 (d, 2H), 7.96 (m, 6H), 8.13 (d, 1H); 8.30 (s, 1H), 8.60 (s, 1H).

ACKNOWLEDGEMENTS

Financial support from Romanian Ministry of Education and Research for grant ID 564 is greatly acknowledged.

REFERENCES

1. S. P. Massie, *Chem. Rev*. **1954,** *54*, 797.
2. P. Hanson, *Advances in Heterocyclic Chemistry*, Ed. A. R. Katritzky, A. J. Boulton, Academic Press, **1980**, *27*, 110.
3. H. Gilman, R. K. Ingham, J. F. Champaigne, J. W. Diehl, R. O. Ranck, *J. Org. Chem*. **1954**, *19*, 560.
4. A. C. Schmaltz, A. Burger, *J. Am. Chem. Soc*. **1954**, *76*, 5455.
5. E. A. Nodiff, H. L. Sarma, T. Kohno, F. Schnierle, M. Mori, A. A. Manian, *J. Heterocycl. Chem*. **1971**, *8*, 321.
6. C. Bodea, I. A. Silberg, *Studii Cercet. Chimie (Cluj),* **1963**, *14*, 317.
7. M. Tosa, C. Paizs, C. Majdik, L. Poppe, P. Kolonitz, I. A. Silberg, L. Novak, F. D. Irimie, *Het. Commun*. **2001,** *7*, 277.
8. H. Gilman, R. D. Nelson, *J. Am. Chem. Soc*. **1953,** 75, 5422.
9. E. Bosch, J. K. Kochi, *J. Chem. Soc. Perkin Trans I*, **1995**, *8*, 1057.
10. L. Găină, A. Csámpai, G. Túrós, T. Lovász, V. Zsoldos-Mády, I. A. Silberg and P. Sohár, *Org. & Biomol. Chem*. **2006**, *4*, 4375.
11. O. Kappe, *Angew. Chem. Int. Ed*., **2004,** *43*, 6250**.**
12. P. Lidstrom, J. Tierney, B. Wathey and J Westman., *Tetrahedron,* **2001,** *57*, 9225.
13. R. S. Varma, R. K. Saini, H. M. Meshram, *Tetrahedron Lett*. **1997**, 38, 6525.
14. R. S. Varma, R. Dahiya, *Tetrahedron Lett*. **1998,** *39*, 1307.
15. E. Bosch, J. K. Kochi, *Res. Chem. Intermed*., **1993**, 16**,** 811; b.) E. Bosch, J. K. Kochi *J. Chem. Soc. Perkin Trans 1*. **1995**, 1057.
16. L. H. Britany „Microwave Synthesis Chemistry at the speed of light" CEM Publishing **2002**, chapter 2, pag. 35.
17. R. B. Barnes, R. C. Gore, R. W. Stafford, V. Z. Williams, *Anal. Chem*. **1948**, *20*, 402.

STUDIA UNIVERSITATIS BABEŞ-BOLYAI, CHEMIA, LIV, 2, 2009

EVALUATION OF SOME AMINO ACIDS AS BRONZE CORROSION INHIBITORS IN AQUEOUS SOLUTION

SIMONA VARVARA[a], MARIA POPA[a], GABRIEL RUSTOIU[b], ROXANA BOSTAN[a], LIANA MUREŞAN[c]

ABSTRACT. A comparative study of the efficiency of two innoxious amino acids derivatives (DL alanine and DL cysteine) on bronze corrosion in 0.2 g/L $NaHCO_3$ +0.2 g/L Na_2SO_4 aqueous solution (pH 5), was studied by electrochemical impedance spectroscopy and polarization measurements.

The two amino acids are non-hazardous towards human beings or the environment and are intended to be used as corrosion inhibitors in the stabilization treatments of the Bronze Age archaeological artefacts belonging to the National Museum of Union in Alba Iulia (Romania). Consequently, the composition of the contemporary bronze samples used in the corrosion testing was chosen close to that of several Bronze Age artefacts (XIIth century B.C.) discovered in Transylvania (Romania) after a preliminary investigation by X-ray fluorescence spectrometry.

The electrochemical investigations showed that the two innoxious amino acids have fairly good inhibiting properties for bronze corrosion, acting mainly as cathodic inhibitors. Their inhibition action could be attributed to the ability of the amino acids to adsorb on the bronze surface and to form an organic layer which protects the metal from corrosion. In the investigated experimental conditions, the best protection of bronze was obtained in the presence of 0.1 mM cysteine (90%). The impedance measurements revealed that the inhibitor effectiveness of the optimal concentrations of amino acids is time-dependent.

Keywords: *bronze, corrosion, non toxic corrosion inhibitors, amino acids*

INTRODUCTION

The conservation and preservation of the cultural heritage is one of the main concerns within Europe today. Among the family of ancient and historical metals, bronzes artefacts that represent a considerable part of the archaeological findings, have been largely studied [1-3], because of their complex degradation phenomena, taking place in the long time span.

---

[a] *"1 Decembrie 1918" University, Science Faculty, Str. Nicolae Iorga, Nr. 11-13, RO-510009 Alba-Iulia, Romania, svarvara@uab.ro*

[b] *National Museum of Union, Str. Mihai Viteazul, Nr. 12, RO-510009 Alba Iulia, Romania*

[c] *"Babes-Bolyai" University, Faculty of Chemistry and Chemical Engineering, Str. Kogalniceanu, Nr. 1, RO-400084 Cluj-Napoca, limur@chem.ubbcluj.ro*

Generally, upon excavation, the sudden change of environment, and sometimes the exposure to a more aggressive condition like polluted urban atmosphere induces the restarting of corrosion [1-6]. Consequently, in order to preserve the archaeological artefacts from corrosion, suitable treatments with coating substances are required. To this regard, in the late fifties and early sixties of the last century, a range of organic corrosion inhibitors, mainly nitrogen and sulphur-containing organic heterocyclic compounds, developed for industry, were tested as corrosion inhibitors of copper and bronze historical objects [7-12]. Among them, benzotriazole (BTA) has been widely accepted in the consolidation of the ancient copper and bronze artefacts being considered as the most efficient corrosion inhibitor over a wide temperature and pH range. Although, recent studies showed that BTA is highly toxic [12], being a cancerigen compound that cannot be degraded.

Therefore, in line with the environment protection regulations, the new trend in industry, as well as, in the conservation–restoration practice is nowadays orientated toward finding new environmentally friendly inhibitors, compounds with good inhibition efficiency of bronze corrosion, but with low risk of pollution [10-13].

When studying the cultural heritage objects, due to their unique nature and value, the evaluation of the efficiency exerted by the new proposed inhibitors for the protection of the authentic artefacts is much complicated and requires a special experimental methodology [14]. Thus, it is considered inappropriate to apply the novel anticorrosive treatments directly on the metallic surface without a preliminary screening, because the new inhibitors might irreversibly damage the ancient object either after the first treatment, or in time. Therefore, test procedures based on non-archaeological materials having a similar composition to the ancient ones are required. In this way, the effects of the new corrosion inhibitors could be studied without damaging the authentic artefacts.

In this context, the present work focuses on a preliminary investigation of the inhibiting behaviour of two amino-acids (cysteine and alanine) on bronze corrosion in an aerated solution of 0.2 g/L Na_2SO_4 + 0.2 g/L $NaHCO_3$ (pH=5) by potentiodynamic polarization (Stern-Geary interpretation) and electrochemical impedance spectroscopy. These substances are nor toxic, neither noxious towards human beings or the environment and have already been reported as efficient corrosion inhibitors of copper in acidic and neutral solutions [13, 15-16]. They are intended to be used as corrosion inhibitors in the stabilization treatments applied on the Bronze Age archaeological artefacts belonging to the National Museum of Union in Alba Iulia (Romania).

The composition of the non-archaeological bronze used as working electrode in the corrosion testing was selected after a preliminary investigation on the chemical composition of several authentic Bronze Age artefacts discovered in Transylvania (Romania).

RESULTS AND DISCUSSION

Polarisation curves

The anodic and cathodic polarisation curves for bronze corrosion after 1-hour immersion in the corrosive solution in the absence and in the presence of various concentrations of amino acids are presented in Figure 1.

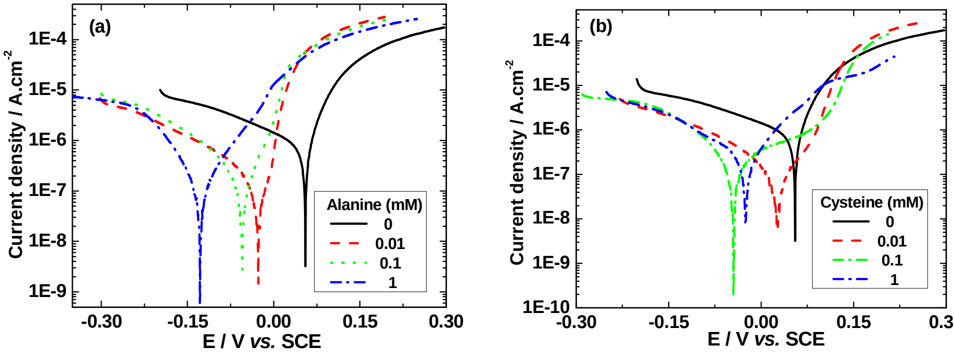

Figure 1. Polarisation curves for bronze in 0.2 g/L Na_2SO_4 + 0.2 g/L $NaHCO_3$ (pH=5) in the absence and in the presence of different concentrations of amino acids: (a) alanine; (b) cysteine. Scan rate, 10 mV/min.

As can be seen in Figure 1 and Table 1, the addition of the two amino acids gives rise to a decrease of the cathodic current densities as compared to the blank solution, in the whole applied potential range. Moreover, a shift of the corrosion potential towards more negative values was put on evidence both, in the presence of alanine and cysteine. This effect is more pronounced as the inhibitors concentration increases and suggests that the two organic compounds act mainly as cathodic-type inhibitors for bronze corrosion in 0.2 g/L Na_2SO_4 + 0.2 g/L $NaHCO_3$ (pH=5) solution.

The electrochemical corrosion kinetic parameters, *i.e.* corrosion potential (E_{corr}), cathodic activation coefficients (b_c, b_a) and corrosion current density (i_{corr}) were evaluated according to the equation:

$$i = i_{corr}\{\exp[b_a(E - E_{corr})] - \exp[b_c(E - E_{corr})]\} \qquad (1)$$

The values of the corrosion parameters in the absence and in the presence of different concentrations of amino acids calculated from the polarization curves are presented in Table 1.

In all cases, the correlation factor R^2 varies between 0.9896 and 0.9989 indicating a good fitting result.

The significant change of the cathodic Tafel coefficients in the presence of the amino acids as compared with the b_c value obtained in inhibitor-free solution suggests that the two organic compounds affect mainly the cathodic reduction of the oxygen, which is in good agreement with the shift of the corrosion potential in the cathodic domain. However, a slight influence of the amino acids on the anodic dissolution of the copper could also be observed.

Table 1. Corrosion parameters for bronze in 0.2 g/L Na_2SO_4 + 0.2 g/L $NaHCO_3$ (pH=5) without and with the addition of different concentrations of amino acids

Inhibitor conc.(mM)	**E_{corr} (mV/SCE)**	**i_{corr} (μA/cm^2)**	**b_a (V^{-1})**	**- b_c (V^{-1})**	**IE (%)**
0	47.80±0.4	1.26±0.03	39.44±0.29	7.68±0.23	-
Alanine 0.01	-24.57±0.4	0.23±0.030	37.50±5.17	11.44±2.13	81.75
0.1	-50.05±0.3	0.17±0.004	39.78±0.67	22.05±0.28	86.51
1	-116.55±0.1	0.31±0.001	27.08±0.36	20.93±0.11	75.40
Cysteine 0.01	36.02±0.6	0.14±0.002	35.23±0.85	17.08±0.21	88.89
0.1	-40.09±0.4	0.12±0.004	14.65±0.20	22.97±0.33	90.47
1	-25.01±0.2	0.26±0.004	28.33±0.14	16.64±0.16	79.36

The significant change of the cathodic Tafel coefficients in the presence of the amino acids as compared with the b_c value obtained in inhibitor-free solution suggests that the two organic compounds affect mainly the cathodic reduction of the oxygen, which is in good agreement with the shift of the corrosion potential in the cathodic domain. However, a slight influence of the amino acids on the anodic dissolution of the copper could also be observed (Table 1).

The corrosion inhibition efficiency (IE) at different concentrations of amino acids was calculated according to following equation [10]:

$$\mathrm{IE}(\%) = 100 \cdot \frac{\mathrm{i}^{0}_{\mathrm{corr}} - \mathrm{i}_{\mathrm{corr}}}{\mathrm{i}_{\mathrm{corr}}} \qquad (2)$$

where $\mathrm{i}^{0}_{\mathrm{corr}}$ and $\mathrm{i}_{\mathrm{corr}}$ are the values of the corrosion current densities in absence and in presence of the inhibitor, respectively.

The values of inhibition efficiency presented in Table 1 reveal that the investigated amino acids have inhibiting properties on bronze corrosion. A possible explanation for the inhibiting behaviour of the two amino acids could be found in their ability to adsorb on the bronze surface and to form an organic layer that protects the metal from corrosion.

The inhibition efficiencies increase as the inhibitors concentration increases and reach the maximum values in the presence of 0.1 mM alanine (86.95%) and 0.1 mM cysteine (90.47%). The further increase of the amino acids concentration in the corrosive solution leads to a decrease of their inhibition efficiency. This phenomenon is consistent with the results already reported for the copper corrosion in the presence of cysteine in neutral and acidic chloride solutions [15] and could be attributed to the saturation of the metallic surface with inhibitor molecules at a certain concentration.

Among the two amino acids, cysteine shows the best inhibition efficiency of the bronze corrosion in 0.2 g/L Na_2SO_4 + 0.2 g/L $NaHCO_3$ (pH=5) corrosive medium, which could be due to the presence of S in the molecular formula of this amino acid.

Electrochemical impedance spectroscopy measurements

In order to obtain further information about the kinetics of bronze corrosion in the presence of amino acids, the electrochemical process was examined by electrochemical impedance spectroscopy (EIS).

Figure 2 shows the impedance diagrams of bronze recorded at the open circuit potential after 1-hour immersion in electrolytes containing various concentrations of amino acids. The high frequency part of impedance spectra is displayed with an enlarged scale in the inserts.

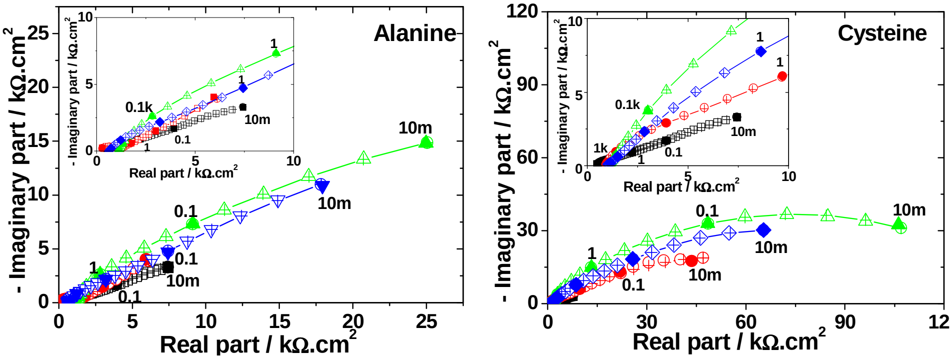

Figure 2. Nyquist plots of bronze electrode in 0.2 g/L Na_2SO_4 + 0.2 g/L $NaHCO_3$ (pH=5) solution, in the absence (□) and in the presence of different concentrations of amino acids: (○) 0.01; (△) 0.1; (◊) 1 mM. The symbol (—+—) corresponds to the simulated spectra. Frequencies are expressed in Hz.

It can be noticed that the impedance spectra of bronze recorded in the absence and in the presence of different concentrations of amino acids exhibit a capacitive behaviour in the whole frequency domain. The significant increase of impedance modulus in presence of the organic compounds proves the inhibition effect exerted by the two innoxious organic compounds on the bronze corrosion.

According to a.c. circuit theory [17], the impedance plots obtained for a given electrochemical system could be described by an equivalent electrical circuit involving different components (resistors, capacitors, inductors) which are associated with different phenomena from the reaction mechanism. The fitting of the experimental data to this pure electronic model allows checking the validity of the proposed mechanistic model and the calculation of the numerical values corresponding to physical and chemical phenomena involved in the electrochemical system under investigation [15].

As mentioned in a previous paper [10], although not clearly seen in Figure 2, the impedance data obtained for bronze corrosion in the absence of any inhibitors could be described by two R-C ladder circuits, which allows a suitable computer fitting of the experimental data. As a result, the (2RC) equivalent circuit from Figure 3a was adopted to carry out the non-linear regression calculation with a Simplex method.

In the presence of the amino acids, three capacitive loops, though badly separated each other are necessary for computer fitting of experimental data with an (3RC) electrical equivalent circuit (Figure 3b).

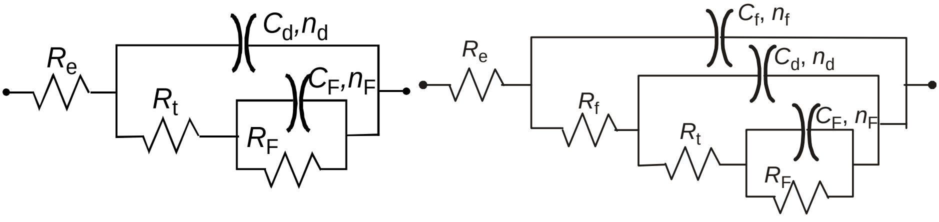

(a) **(b)**

Figure 3. Equivalent electrical circuits used for computer fitting of the experimental data: (a) 2RC and (b) 3RC

In the circuits from Figure 3, R_e represents the electrolyte resistance; the *high frequency elements* (R_f and C_f) are related to the dielectric character of the corrosion products (C_f) due to formation of a thin surface layer that is reinforced in the presence of the inhibitors and by the ionic conduction through its pores (R_f); the *medium frequency contribution* (R_t and C_d) corresponds to the charge transfer resistance and to the double layer capacitance at the bronze/electrolyte interface, while the *low frequency contribution* (R_F and C_F) symbolizes the faradic resistance and faradic capacitance due to an oxidation - reduction process taking place at the electrode surface, probable involving the corrosion products. The parameters n_d, n_f, and n_F are coefficients representing the depressed characteristic of the three capacitive loops in the Nyquist diagrams.

A comparison of the experimental and calculated impedance spectra presented in Figure 2 shows that the used equivalent electrical circuits reproduce correctly the experimental results obtained in the absence and in the presence of amino acids, respectively.

The values of the impedance parameters calculated by non-linear regression of the impedance data in the absence and in the presence of different concentrations of amino acids are presented in Table 2.

Table 2. The results of non-linear regression of the impedance spectra presented in Figure 2

Inhibitors conc. (mM)	**R_e (kΩcm^2)**	**R_f (kΩcm^2)**	**C_f (μF/cm^2)**	**R_t (kΩcm^2)**	**C_d (μF/cm^2)**	**R_F (kΩcm^2)**	**C_F (μF/cm^2)**	**R_p (kΩcm^2)**	**IE (%)**
0	0.46	-	-	3.34	36.84	12.66	1652.63	16.01	-
Alanine									
0.01	1.03	2.70	11.35	4.59	32.49	42.11	210.23	49.40	67.60
0.1	1.08	3.20	7.08	6.93	3.34	76.04	92.83	86.17	81.42
1	0.60	0.14	0.28	4.82	3.98	70.26	180.00	75.22	78.72
Cysteine									
0.01	0.89	0.76	1.02	21.40	13.79	77.07	40.81	99.23	83.86
0.1	1.08	1.53	0.94	42.55	1.95	126.71	31.44	170.79	90.63
1	0.92	0.55	1.99	30.72	11.05	95.21	120.17	126.48	87.34

$^*R_p = R_f + R_t + R_F$

The inhibition efficiency (IE) of the amino acids was calculated from the polarization resistance values, as follows:

$$\mathrm{IE}(\%) = 100 \cdot \frac{R_p^0 - R_p}{R_p} \tag{3}$$

where R_p and R^0_p are the polarisation resistances in electrolytes with and without amino acids, respectively.

As expected, the film resistance R_f increases and attains the maximum values in the presence of 0.1 mM alanine and 0.1 mM cysteine. In the same time, the C_f values decreases proving that the surface film formed in presence of these optimum concentrations of amino acids is probably thicker and less permeable. The decreases of the R_t values observed at higher concentrations of the amino acids suggests that the surface layer formed in the presence of the inhibitors is less protective.

Furthermore, the R_t increases and C_d decrease in the presence of the amino acids as compared with the values obtained in the absence of the inhibitors. The decreases of the C_d values in the presence of the amino acids could be due to a smaller area of the electrode directly in contact with the electrolyte under the corrosion product layer or to a less conducting nature of this film. The variation of the R_F and C_F values in the presence of the corrosion inhibitors assess also the stability of the surface film.

The values of the polarisation resistance R_p, calculated as the sum (R_f + R_t + R_F) from the resistances values determined by the regression calculation (Table 2) show that the corrosion rate significantly decreases in the presence of the amino acids. This effect should be related to the inhibiting effect of the amino acids on the corrosion process, due to their adsorption on the bronze surface, forming a blocking barrier to corrosion process. The highest values of the R_p and, consequently, the maximum inhibition efficiency values were obtained in the presence of the optimal concentration of amino acids (0.1 mM alanine and 0.1 mM cysteine).

The inhibition efficiencies, calculated from ac impedance results, show the same trend as those estimated from the polarisation measurements. In the investigated experimental conditions, cysteine has proved to be the best corrosion inhibitor of bronze.

The better inhibition efficiency exhibited by cysteine compared to alanine could be explained if we take into consideration that the molecular structure of cysteine contains, apart from the amino group, a -SH group that also has a strong adsorption affinity for copper and plays an key role in the inhibition process [13, 15-16]. Consequently, cysteine can be adsorbed on the bronze surface as bidentate ligands, in which the coordination is taking place through both the amino- and mercapto- groups.

Since the corrosion process is time-dependent, the inhibiting effect exerted by the amino acids on bronze, during long-time exposure in the corrosive media was also studied.

Nyquist plots of bronze recorded after different times of immersion in the electrolytes with or without the optimum concentration of amino acids are shown in Figure 4.

By comparing the impedance spectra obtained at different immersion times in the presence of 0.1 mM alanine, it was found that the impedance increases with the immersion time up to maximum in 48 hours, and then slowly decreases with further increases of the immersion time up to 132 hours. The decrease of the inhibition efficiency at long exposure times may be due to a deterioration of the protective layer formed in the presence of alanine on the bronze surface.

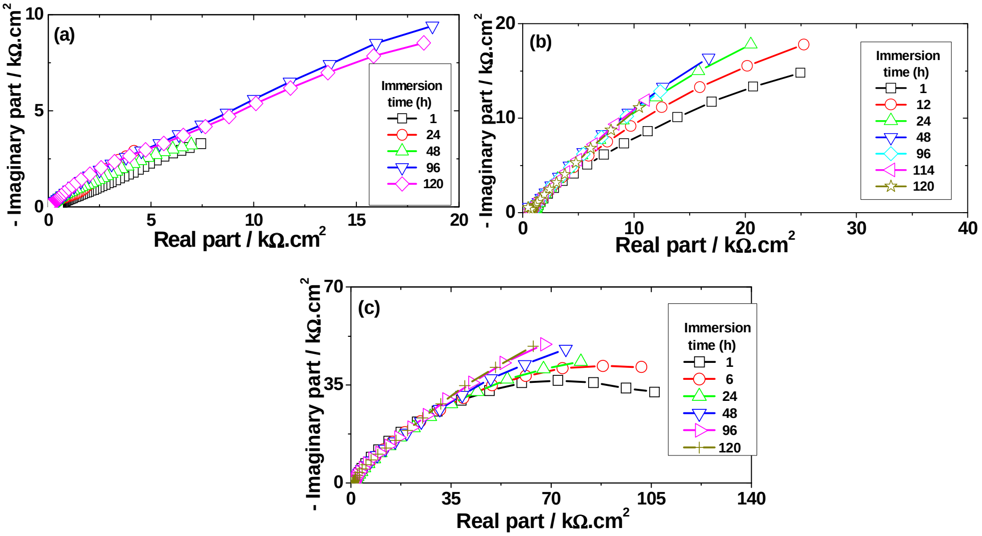

Figure 4. EIS evolution of bronze in 0.2 g/L Na_2SO_4 + 0.2 g/L $NaHCO_3$ (pH=5) solution in the absence (a) and in the presence of the optimal concentration of amino acids: (b) 0.1 mM alanine; (c) 0.1 mM cysteine.

In the presence of 0.1 mM cysteine, the impedance continuously increases and attains a maximum value in 48 hours, which tends to remain nearly constant with further increases of the immersion time up to 120 hours.

CONCLUSIONS

The electrochemical measurements showed that the investigated innoxious amino acids have fairly good inhibition properties on contemporary bronze corrosion, which makes them potential candidates for the protection of the archaeological bronzes. The investigated amino acids mainly act as cathodic inhibitors by decreasing the corrosion current and shifting the corrosion potential towards more negative values.

In the impedance diagrams, the inhibiting effect of the amino acids results in a significant increase of the impedance modulus in the whole frequency domain, and also in the appearance of the third time constant due to the formation of a protective film between the corrosion products and amino acids molecules.

In the investigated experimental conditions, disregarding its concentration in the corrosive solution, cysteine has proved to be a better inhibitor of bronze corrosion compared to alanine. The improved inhibition effect of cysteine was ascribed to the involvement of the mercapto group that allows a stronger adsorption of the organic molecule as bidentate ligands through the -SH and $-NH_2$ groups.

The variation of the impedance during long time measurements suggests that the protective effectiveness of the optimal concentrations of amino acids on bronze corrosion process is time-dependent.

The effects exerted by the two innoxious amino acids on the surface of bronze covered with artificially created patina will be presented in a future paper, giving additional data on the protectiveness action of the amino acids as corrosion inhibitors of the genuine artefacts belonging to the Bronze Age and discovered in the archaeological settlements from Transylvania.

EXPERIMENTAL SECTION

First, the composition of the non-archaeological bronze used as working electrode in the corrosion testing was selected after a preliminary investigation on the chemical composition of several authentic Bronze Age artefacts. Then, the influence of the non-toxic organic inhibitors (alanine and cysteine) on bronze corrosion in aqueous solution was investigated.

Archaeological Transylvanian bronze artefacts

The examined authentic artefacts belong to the collection of the National Union Museum at Alba Iulia, Romania. As can be seen in Figure 5, the artefacts consist in tools (sickles and scrapers) and jewellery (pendants) datable back to Late Bronze Age (XIIth century B.C.) and were discovered at Noslac – “La Manastire” (Alba County) archaeological settlement in Transylvania (Romania).

Figure 5. Examples of authentic bronze artefacts datable back to Late Bronze Age

The chemical composition of the archaeological artefacts was determined using a Quant' X ARL X-ray fluorescence spectrometer (Thermo Scientific, USA) and the results are presented in Table 3.

Table 3. Alloy composition of Transylvanian archaeological artefacts (wt-%)

Sample	**Cu**	**Sn**	**Sb**	**As**	**Zn**	**Fe**	**Pb**	**Si**	**Ni**	**Total**
S1	92.73	5.09	0.49	0.37	0.07	0.05	0.13	0.60	0.47	100
S2	88.38	9.62	0.53	0.29	0.11	-	0.08	0.61	0.38	100
S3	90.74	6.91	0.62	0.40	0.09	0.06	0.05	0.70	0.43	100
S4	90.28	7.03	0.63	0.58	0.11	-	0.15	0.75	0.47	100
S5	90.94	7.76	0.11	0.07	0.12	-	-	0.75	0.25	100
S6	87.91	9.75	0.51	0.38	0.10	-	-	0.92	0.43	100
S7	86.96	10.19	0.73	0.18	0.08	0.54	0.08	0.83	0.41	100
S8	87.82	9.59	0.83	0.52	0.08	-	0.04	0.70	0.42	100
S9	87.03	10.69	0.24	0.17	0.11	0.47	0.02	0.84	0.43	100
S10	88.12	9.61	0.48	0.35	0.09	0.25	0.11	0.63	0.44	100
S11	94.91	2.08	0.60	0.86	0.07	0.17	0.01	0.66	0.64	100
S12	86.80	9.78	0.48	0.58	-	0.06	0.08	1.62	0.60	100
S13	91.35	7.19	0.35	0.34	0.07	0.11	0.02	0.04	0.53	100

The investigated authentic Bronze Age artefacts are essentially Cu-Sn binary alloys with small amounts of Sb, As, Fe, Pb, Zn and Si as impurities (Table 3). The Sn content varies between 2.08% and 10.69%, and the mean value within the thirteen archaeological samples examined was to around 6.4%. This result justifies the choice of the modern bronze with the composition presented in Table 4 as working electrode for corrosion testing.

Table 4. Weight composition (%) of the modern bronze used as working electrode

Cu	**Sn**	**Pb**	**Zn**	**Sb**	**Ni**	**Fe**	**As**	**Si**
87.998	6.43	3.25	1.43	0.299	0.252	0.11	0.033	0.198

Reagents

The corrosive medium was an aqueous aerated solution of 0.2 g/L Na_2SO_4 + 0.2 g/L $NaHCO_3$, acidified to pH=5 by addition of dilute H_2SO_4. This electrolyte corresponds to a strong acidic rain in an urban environment.

The two amino acids (DL-alanine and DL-cysteine, Sigma Aldrich) used as corrosion inhibitors were dissolved in the electrolyte solution to the following concentrations: 0.01; 0.1 and 1 mM. The concentration ranges of the amino acids were selected taking into account the results previously reported on the study of copper corrosion in neutral and acidic solutions [13, 15-16].

The molecular structures of the investigated amino acids are shown in scheme 1.

DL - Alanine

DL - Cysteine

Scheme 1. *Molecular structure of the investigated amino acids*

Electrochemical measurements

The investigation of the inhibiting properties of amino acids on bronze corrosion was performed by electrochemical methods using potentiodynamic polarisation and electrochemical impedance spectroscopy.

An electrochemical cell with a three-electrode configuration was used; the working electrode (0.38 cm^2) was made of contemporary bronze with the composition presented in Table 4; a large platinum grid and a saturated calomel electrode (SCE) were used as counter and reference electrodes, respectively. Prior to use, the bronze surface was mechanically polished using grit paper of 600 and 1200 and rinsed thoroughly with distilled water.

Electrochemical experiments were performed using a PAR model 2273 potentiostat controlled by a PC computer.

Anodic and cathodic polarization curves were recorded in a potential range of $E = E_{corr} \pm 200$ mV with a scan rate of 10 mV/min.

Electrochemical impedance measurements were carried out at the open circuit potential after 1-hour immersion of the bronze electrode in the corrosive solution. The impedance spectra were acquired in the frequency range 100 kHz to 10 mHz at 10 points per hertz decade with an AC voltage amplitude of ±10 mV. The impedance data were then analyzed with software based on a Simplex parameter regression.

ACKNOWLEDGMENTS

The authors gratefully acknowledge CNCSIS for financial support under the project PNCDI II - Idei, code 17/2009.

REFERENCES

1. L. Robbiola, “Caracterisation de l’alteration de bronzes archeologiques enfouis a partir d’un corpus d’objet de l’Age du Bronze. Mecanisme de corrosion”, Thesis, Universite Paris VI, **1990**.

2. W. Mourey, “Conservarea antichitatilor metalice: de la sapatura la museu”, Editura Technica, Bucuresti, **1998**.
3. M. Wadsak, I. Constantinides, G. Vittiglio, A. Adriaens, K. Janssens, M. Schreiner, F. C. Adams, P. Brunella, M. Wuttmann, *Mikrochimica Acta*, **2000,** *133*, 159.
4. H. Strandberg, *Atmospheric Environment*, **1998**, *32*, 3511.
5. H. Strandberg, *Atmospheric Environment*, **1998**, *32*, 3521.
6. A. Krätschmer, I. O. Wallinder, C. Leygraf, *Corrosion Science*, **2002**, *44*, 425.
7. V. Otieno-Alego, D. Hallam, A. Viduka, G. Heath, D. Creagh, “Metal 98”, James & James Science Publishers Ltd., London, **1998**, 315.
8. P. Letardi, A. Beccaria, M. Marabelli, G. D’Ercoli, “Metal 98”, James & James Science Publishers Ltd., London, **1998**, 303.
9. L. Muresan, S. Varvara, E. Stupnisek-Lisac, H. Otmacic, K. Marusic, S. Horvat Kurbegovic, L. Robbiola, K. Rahmouni, H. Takenouti, *Electrochimica Acta*, **2007**, *52*, 7770.
10. S. Varvara, L. Muresan, K. Rahmouni, H. Takenouti, *Corrosion Science*, **2008**, *50*, 2596.
11. I. Ignat, S. Varvara, L. Muresan, *Studia Universitatis Babes-Bolyai, Chemia,* **2006**, *L1*, 127.
12. R. Faltermeier, *SSCR Journal*, **1998**, *9*, 1.
13. D.-Q. Zhang, L-X. Gao, G.-D. Zhou, *Journal of Applied Electrochemistry*, **2005** *35*, 1081.
14. D. Jones, “Principles and Prevention of Corrosion Scottish Museums Council factsheet: Caring for metal collections in museums”, Macmillan Publishing Company, New York, **2003**.
15. K. M. Ismail, *Electrochimica Acta*, **2007**, *52*, 7811.
16. K. Bauroni, L. Bazzi, R. Saghi, M. Mihit, B. Hammouti, A. Albourine, S. E. Issami, *Materials Letters*, **2008**, *62*, 3325.
17. A. J. Bard, L. R. Faulkner, “Electrochemical methods. Fundamentals and Applications” (2nd Edition), John Wiley & Sons Publisher, New York, **2001**, chapter 10.

STUDIA UNIVERSITATIS BABEŞ-BOLYAI, CHEMIA, LIV, 2, 2009

STUDY ON THE ELECTRODEPOSITION OF MOLYBDENUM OXIDES ON COPPER SUPPORT

**RADU BANICA[a,b], NICOLAE VASZILCSIN[a],
TEREZIA NYARI[b], GEZA BANDUR[a]**

ABSTRACT. Transition metal oxides (WO_3, MoO_3, V_2O_5) are intensively studied for applications in batteries, catalysis and energy storage. There are several methods for thin films preparation of these materials, including electrodeposition from aqueous electrolyte solutions. In this paper it is studied the electrochemical deposition of molybdenum oxides at different electrodeposition potentials using peroxo-polymolybdate and ammonium molybdate as precursors in a 0.05 M solutions at pH = 2.3 and 5.5. Metallic copper was used as a support. The obtained thin films have been characterized by cyclic voltammetry, optical microscopy and differential scanning calorimetry.

Keywords: *electrodeposition, thin film, cyclic voltammetry.*

INTRODUCTION

Molybdenum oxides are very promising materials for the construction of high power density accumulators for energy storage [1]. In 1987, Auborn and Barberio [2] reported the possible utilisation of MoO_2 as anode material in lithium-based batteries.

The morphological and structural characteristics of the molybdenum oxides prepared by different methods have significant influence on the batteries charging-discharging cycles, stability and lifetime. Nanostructured oxides having high specific surface areas enable a more easy diffusion of lithium ions during the charging-discharging process.

Molybdenum oxides are also useful in the construction of gas sensors for CO detection [3], ion-selective sensors [4] or thin film catalysts for different processes [5, 6].

There are several methods for the preparation of molybdenum oxides thin films, among which are spray-pyrolysis (SP), Metal-Organic Chemical Vapour Deposition (MOCVD), Pulsed Laser Deposition (PLD) [7-9]. In the case of spray-pyrolysis, the precursor (an aqueous solution of molybdenum

---

[a] *University "Politehnica" of Timisoara, Piata Victoriei 2, 300006 Timisoara, Romania*
[b] *National Institute for Research and Development in Electrochemistry and Condensed Matter, Str. Plautius Andronescu 1, 300224 Timisoara, Romania, vaszilcsin@yahoo.com*

pentachloride, ammonium molybdate, etc.) is sprayed in oxidizing atmosphere (air) onto heated glass where it decomposes with the formation of a thin layer of MoO_3 [7]. Oxide layers can also be deposited on conductive supports by electrochemical procedures using aqueous electrolyte solutions of $(NH_4)_6(Mo_7O_{24})$, $Li_6Mo_7O_{24}$, or Na_2MoO_4 [10,11]. If aqueous peroxo-polymolybdate solutions are used, oxide layers with different molybdenum oxidation states can be obtained [12-14].

In a former paper [15], we reported some of our results related to the preparation of molybdenum oxides thin films by a comparative study concerning their electrochemical deposition on platinum and copper. In the present work, new experimental results on electrodeposition of molybdenum oxides on copper are presented, with the aim to complete the characteristics of deposited layers.

RESULTS AND DISCUSSION

Dissolution of molybdenum

According to ref. [13], the reactions taking place during the dissolution of the Mo powder in H_2O_2 (diluted aqueous solution; pH < 3) are:

$$2Mo_{(s)} + 10[H_2O_2] \rightarrow [Mo_2O_3(O_2)_4(H_2O)_2]^{2-} + 2[H_3O^+] + 5H_2O \quad (1)$$

$$2[Mo_2O_3(O_2)_4(H_2O)_2]^{2-} + 2[H_3O^+] \leftrightarrow [Mo_4O_9(O_2)_4]^{2-} + 4[H_2O_2] + 3H_2O \quad (2)$$

As illustrated by Eq. (1), H_2O_2 acts both as an oxidizing agent and as ligand. At pH < 3, in solutions with low peroxide amounts and containing higher molybdate concentration, the initially formed peroxomolybdate species can polymerize as it is shown in - Eq. (2).

Cyclic voltammetry

In order to establish the potential range, inside which stable thin oxide layers can be obtained by potentiostatic cycling, voltammograms have been registered in the working solutions.

In Figure 1 the voltammogram obtained by scanning the potential from +200 mV to –900 mV vs. Ag/AgCl, with a rate of 10 mVs^{-1}, is presented. The peak with the maximum value at around -100 mV vs. Ag/AgCl is due to the reduction of Mo(VI) ions adsorbed at the electrode surface as a complex species. In the same time, in the close vicinity of the electrode, the solution color becomes blue – proving the Mo(VI) reduction to Mo(V).

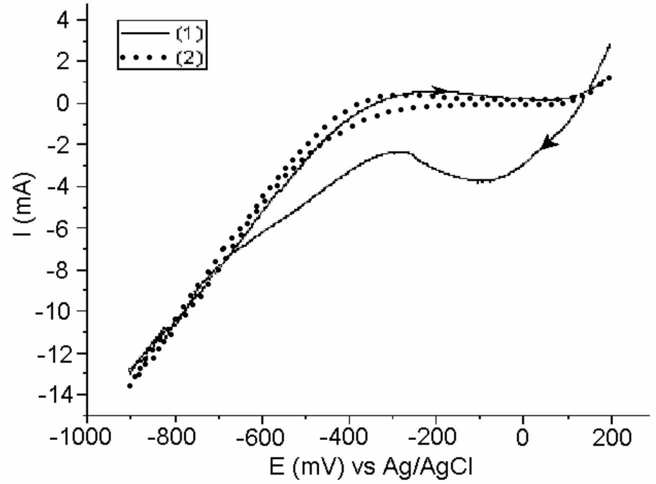

Figure 1. Cyclic voltammograms obtained for peroxo-polymolybdate solution on copper support (surface area 1 cm^2). Continuous line–cycle 1; dashed line–cycle 2.

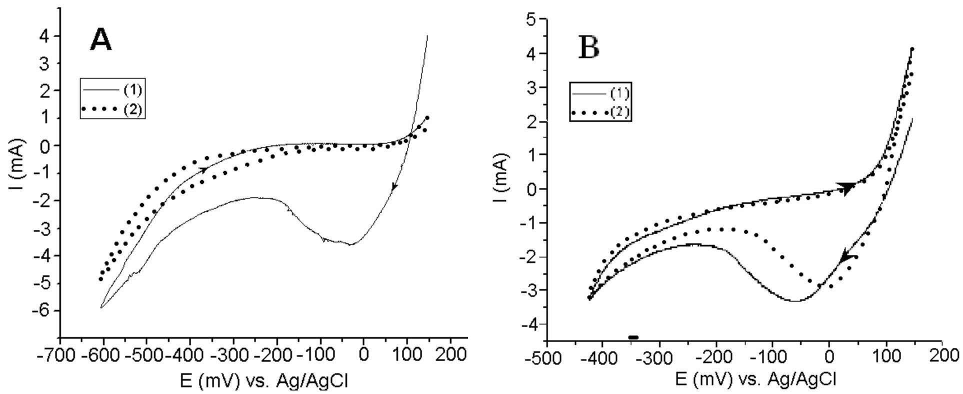

Figure 2. Cyclic voltammograms obtained using peroxo-polymolybdate as precursor solution. The potential was scanned between +0.15 and – 0.60 V *vs.* Ag/AgCl (A), respectively, between +0.15 and - 0.42 V *vs.* Ag/AgCl,KCl_{sat} (B).

At a potential value around -250 mV, a Mo(VI) diffusion limiting current appears. At potentials more negative than -350 mV, the cathodic current rises due to H_3O^+ ions discharge; this process occurs simultaneously with the metal ions reduction.

The potential, at which theoretically the hydrogen evolution is possible, at the actual value of pH, is – 0.33 V *vs.* Ag/AgCl,KCl_{sat}. At a potential value around -650 mV, the reduction curve slope increases, due to the formation of a molybdenum oxide layer on the cathode surface. In the second cycle (dashed line), the current observed is that corresponding to hydrogen evolution. This fact is due to the formation of a stable oxide layer that confers passivity to the cathode surface. The formation of this layer is probably influenced also by the fact that alkalinity of the medium in the close vicinity of the interface increases.

Taking into account that in the diffusion layer the molybdenum concentration diminishes and the HO^- ions concentration increases (due to H_3O^+ ions discharging), in the proximity of the charge transfer surface there may coexist the following species [13]:

$[Mo_2O_3(O_2)_4(H_2O)_2]^{2-}$ pH < 5 and (H_2O_2):Mo = 2 : 1 ; $C_{Mo} < 10$ mM

$[Mo_4O_9(O_2)_4]^{2-}$ pH < 5 and (H_2O_2):Mo = 2 : 1 ; $C_{Mo} < 10$ mM

$[Mo_7O_{23}(O_2)]^{6-}$, $[Mo_7O_{22}(O_2)_2]^{6-}$ pH ~ 4 at low $C_{H_2O_2}$

Figure 2 shows the cyclic voltammograms recorded using the same precursor solution, but different ranges of potential scanning, in order to determine the least negative potential for which the layer becomes stable in the working solution. It has been observed that the stability of the oxide layers deposited on copper by potentiostatic cycling depends on the minimum value of the potential attained during the scanning.

If the cathode potential is more negative than –0.55 V *vs.* Ag/AgCl,KCl_{sat}, one can obtain a stable oxide layer (Figure 1 and 2 A). For potentials more positive than the above value, at each cycle, one can observe the Mo(VI) reduction without the formation of a stable oxide layer (Figure 2B).

Because the working solution is acid and oxidant at the same time, the copper support may be dissolved with the formation of Cu^{2+} ions. Consequently, the anodic current observed at potentials more positive than +100 mV *vs.* Ag/AgCl,KCl_{sat} was attributed to copper oxidation. The copper ions as formed will be again reduced to metallic copper, which can be integrated in the deposited oxide layer.

The polarization curves obtained in solution 2 using copper as substrate were presented in a previous paper [14].

Optical microscopy and Differential Scanning Calorimetry (DSC) study

Micrographs for layers deposited by cyclic voltammetry (3 cycles) in the potential range of -600 ÷ -610 mV *vs.* SCE using solution 1, are presented in Figure 3. The potential scanning rate was 50µV/s. In all cases, the micrographs have been registered after a heat treatment of the samples.

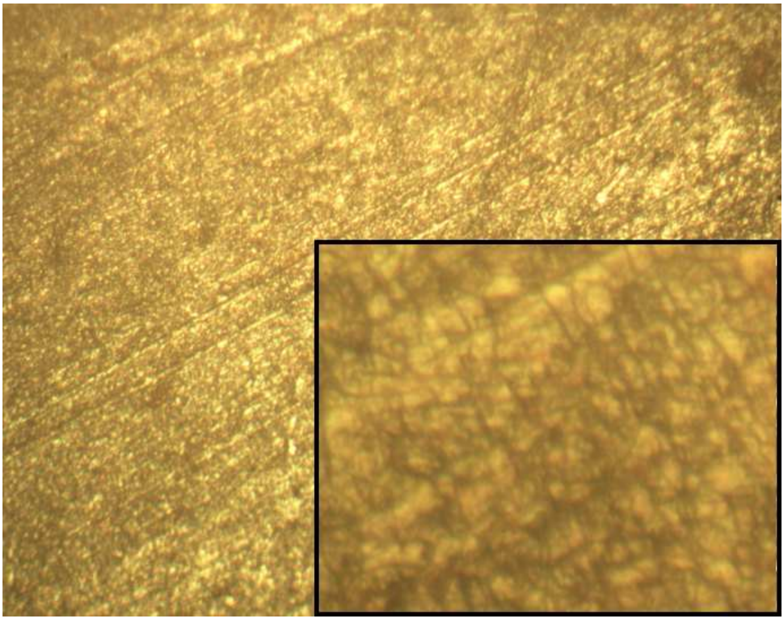

Figure 3. Micrographs of the layers deposited on copper support by cyclic voltammetry and heat-treated; potential range of -600 ÷ -610 mV *vs.* SCE.

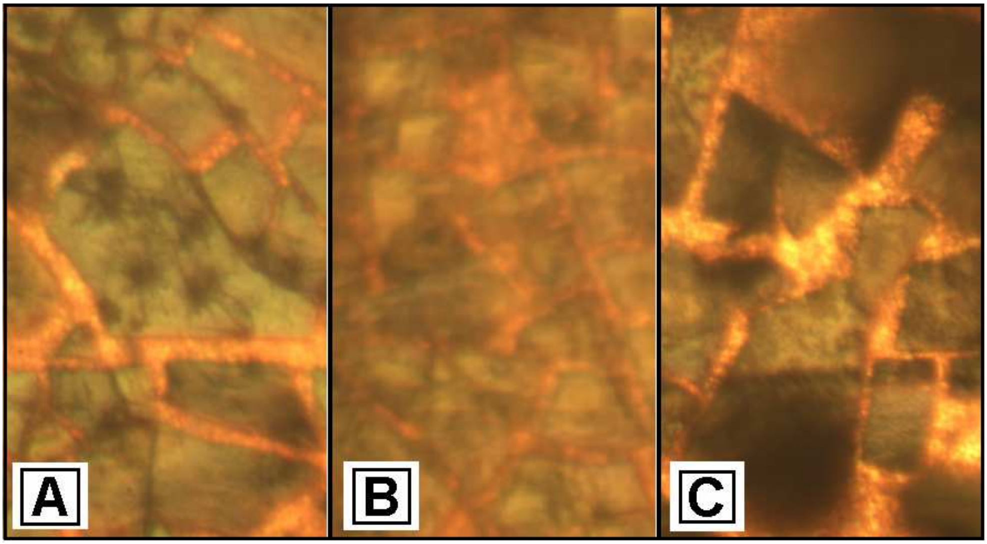

Figure 4. Micrographs of the layers deposited on polished (mirror-like) copper support by cyclic voltammetry and heat-treated; potential range -700 ÷ -710 mV (A) ; -800 ÷ -810 mV (B) ; -900 ÷ -910 mV (C) *vs.* SCE.

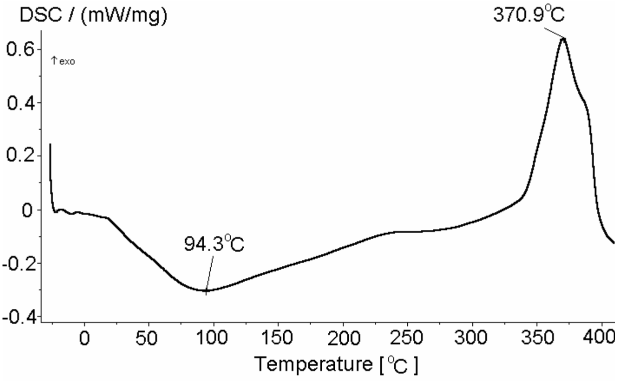

Figure 5. DSC curve of the powder (resulted from scraping away thin films deposited on copper support). Temperature range: -25 ÷ 420 ºC.

It has been observed that the most adherent layers obtained after the heat treatment are those deposited at the most positive potentials. At potentials above -700 mV *vs.* SCE, the deposited layers show multiple cracks and a poor adherence (Figure 4 A-C).

In the DCS curve (Figure 5) one can observe the presence of two important peaks related to two opposite thermal effects: one endothermic, in the 20 – 240ºC range, followed by a strong exothermal process at temperatures above 340ºC with a maximum at about 370ºC. The endothermic process is attributed to the gradual elimination by a physical route of water from the oxide layer up to about 100ºC, followed by the dehydration of the molybdenum hydroxy-oxides up to 240ºC. The exothermal process may be due to the crystallization of the amorphous molybdenum oxide. This supposition is sustained by the mass-loss obtained by TG – DTG analysis and also by the XRD spectra obtained on samples heat treated in inert environment at different temperatures [15].

Our experimental data are in good agreement with those reported in the literature [16], where amorphous films of molybdenum hydroxy-oxide with Mo(IV) oxidation state, containing significant amounts of water, were electrodeposited on TCO (Transparent Conducting Oxide) using ammonium molybdate as precursor.

CONCLUSIONS

Thin films of molybdenum hydroxy-oxides can be electrodeposited on metallic copper using both diluted peroxo-polymolybdate and ammonium molybdate aqueous solutions as precursors. When peroxo-polymolybdate solution is used, stable layers can be deposited only for potentials more negative than –550 mV *vs.* Ag/AgCl,KCl_{sat}. The optical microscopy investigation of the thin films, heat treated at 350ºC in inert atmosphere, reveal the formation of multiple cracks in the oxide layer, which can be due to the shrinkage induced by water elimination. The so deposited films are amorphous in both cases. The hydroxy-oxide deposited from molybdate solution contains water and crystallization occurs by heat treatment at temperatures above 340ºC.

EXPERIMENTAL SECTION

Reagents and solutions

The experimental procedures used for the electrodeposition of molybdenum oxides thin films on copper are described hereinafter.

In the first step, two solutions are prepared (denoted “solution 1” and “solution 2”), as follows:

Solution 1: 0.05 M Mo(VI) concentration has been obtained by dissolving metal powder (Mo 99% , Carlo Erba) in 10 mL 30% H_2O_2, by continuous cooling. The so obtained yellow solution was completed to 250 mL with bidistilled water.

After storing for 24 h at room temperature in the dark, the concentration of H_2O_2 has been determined by titration with $KMnO_4$ 0.02 M in a strong acid medium. Hydrogen peroxide was added until the optimum value 1:1 of H_2O_2 : Mo ratio [13]. The pH solution was 2.3.

Solution 2: an appropriate quantity of $(NH_4)_6Mo_7O_{24}\cdot4H_2O$, 98% (Reactivul) was dissolved in bidistilled water resulting a solution with concentration 0.05 M and pH 5.5.

Electrodes and electrolysis cell

An electrolysis cell with 250 mL capacity has been used. $Ag/AgCl,KCl_{sat}$ was used as a reference electrode. High purity graphite (20 x 80 x 10 mm) was used as a counter electrode.

As working electrode Cu (foil 99.98%, Sigma–Aldrich) with a surface of 1 cm^2 has been used. The smooth Cu electrode has been prepared by polishing with different abrasive papers and then with alumina 50 nm (Buehler).

Thin films characterisation

The most adherent thin films deposited on Cu have been subjected to heat treatment at atmospheric pressure at 350ºC for 1 h in high purity argon (99.999 %, Linde Gas – Romania). The temperature was raised with a rate of 15 ºC/min.

Thin films were electrodeposited by cyclic voltammetry within a very narrow potential domain (10 mV) and using the same peroxo-polymolybdate solution. In these cases the support was metallic copper (4 cm^2), polished mirror-like. SCE was used as reference electrode. The so obtained thin layers have been heat treated under the same conditions and then studied by optical microscopy. From solution 2, oxide layers were electrodeposited on copper support for 2800 s, at a potential of –650 mV *vs.* Ag/AgCl,KCl$_{sat}$. After deposition, these films were washed with distilled water and scraped away from the copper support.

Differential Scanning Calorimetry (DSC) analysis (Netzsch DSC 204) was performed on samples prepared by scraping away the thin films from the copper support. Sample mass was 5.2 mg and nitrogen was used as inert atmosphere. The temperature increasing rate was 5 K min^{-1}.

REFERENCES

1. M. Winter, J.O. Besenhard, M.E. Spahr and P. Novak, *Advanced Materials*, **1998**, *10*, 725.
2. J.J. Auborn and Y. L. Barberio, *J. Electrochem. Soc.*, **1987**, *134*, 638.
3. M. Ferroni, V. Guidi, G. Martinelli, P. Nelli, M. Sacerdoti and G. Sberveglieri, *Thin Solid Films*, **1997**, *307*, 148.
4. L. Tian, L. Liu, L. Chen, N. Lu and H. Xu, *Sensors and Actuators B: Chemical*, **2005**, *105*, 484.
5. S.T. Oyama and W. Zhang, *J. Am. Chem.Soc.*, **1996**, *118*, 7173.
6. W. Wen, J. Liu, W. Michael, M. Nebojsa, H. Jonathan and R. José, *Catalysis Letter.*, **2007**, *113*, 1.
7. L. Boudaoud, N. Benramdane, R. Desfeux, B. Khelifa and C. Mathieu , *Catalysis Today*, **2006**, *113*, 230.
8. K. Gesheva,A. Szekeres and T. Ivanova, *Solar Energy Materials and Solar Cells*, **2003**, *76*, 563.
9. R.M. Guerrero, J.R.V. Garcia, V. Santes and E. Gomez, *J. Alloys and Comp.*, **2007**, *434*, 701.
10. R. Banica, N. Vaszilcsin, T. Nyari, P.Barvinschi and R. Lazau, *Annals of West University of Timisoara, Series of Chemistry*, **2007**, *16*, 17.
11. X. B. Wang, G. Hu, F. B. Liu and J. S. Dong, *Acta Chimica Sinica*, **1996**, *54*, 603.
12. T.M. McEvoy and K.J. Stevenson, *Anal. Chim.Acta*, **2003**, *496*, 39.
13. T.M. Todd, Electrochemical Synthesis and Nanoscale Characterization of Polymorphous Molybdenum Oxide, Dissertation, *University of Texas at Austin*, **2003**, pp. 16–18.
14. T.M. McEvoy and K.J. Stevenson, *J. Materi. Research*, **2004**, *19*, 429.
15. R. Banica, P. Barvinschi, N. Vaszilcsin and T. Nyari, *J.Alloys and Comp.*, **2008**, DOI: 10.1016/ j. jallcom. 2008. 08. 119
16. S.R. Patil, D.M. Uplane and S.P. Patil, *Applied Surface Science*, **2006**, *252*, 8050.

STUDIA UNIVERSITATIS BABEŞ-BOLYAI, CHEMIA, LIV, 2, 2009

N-ALKYLATION OF ACRIDONE BY MEANS OF MICROWAVE IRRADIATIONS WITHOUT SOLVENT

CERASELLA INDOLEAN[a,*], LUIZA GĂINĂ[a] AND MAJDIK CORNELIA[a]

ABSTRACT. Using as solid support reagent KF absorbed on Al_2O_3, the *N*-alkylation of acridone under microwaves irradiation conditions has been realized. The identity of the resulting *N*-alkyl acridones was assigned on the basis of comparative literature melting points and ^{1}H–NMR spectra. Our yields, ranging between 90–96%, were similar or even higher with respect to those already reported in the literature.

Keywords: *N-acridones, microwaves irradiation, KF/Al_2O_2 catalyst, solid support.*

INTRODUCTION

N-Akylacridones are compounds of interest in organic synthesis and pharmaceutical chemistry [1, 2]. Their preparation was previously achieved by using phase transfer catalysis [3, 4], starting from acridone in reaction with various alkyl halides. In contrast with the reported results in the above classical acridone's *N*-alkylation conditions, the application of microwaves irradiation methodology, *e.g.* by using a conventional microwaves oven, in the presence of phase transfer catalysis and of $NaOH/K_2CO_3$ absorbed on Al_2O_3 is known to give better results [5]. Thus, under microwaves irradiation, some authors [5] found that the yields largely depend on the strength of base.

Taking into account this observation, we attempted at seeing whether the preparation of *N*-akylacridones could be improved in the presence of KF, as solid support reagent, absorbed on Al_2O_3 [6]. It is already known that, in these conditions, K_3AlF_6 is formed as a result of KF reaction with alumina, F^- ions being responsible for the catalytic activity of KF/Al_2O_3 system rather than O^{2-} ions which are active sites on $NaOH/K_2CO_3$ absorbed on Al_2O_3 [7].

RESULTS AND DISCUSSION

The reactions were carried out in a microwave synthesis system, by simple mixing the acridone with alkylbromides adsorbed on KF/Al_2O_3 (Scheme 1).

---

[a] *"Babeş-Bolyai" University, Department of Chemistry, 11 Arany Janos st., RO-400028 Cluj-Napoca, Romania,* cella@chem.ubbcluj.ro

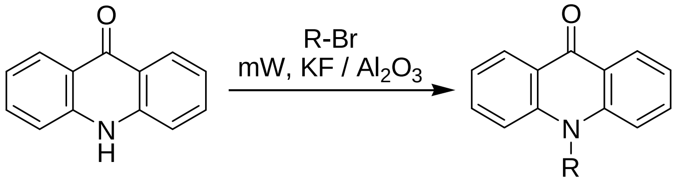

1-6

1: R = Me; **2**: R = Et; **3**: R = *n*-Pr
4: R = *n*-Bu; **5**: R = $(CH_2)_2CH(CH_3)_2$
6: R = Bn

Scheme 1.

The results of our experiments are shown in **Table 1**.

Table1. Preparation of *N*-alkylacridones **1-6** using microwave irradiation and KF/Al_2O_3 as solid support

Compd.	Molar ratio Acridone : alkylbromide	Micro-wave power (W)	Irradiation time (min.)	Yield (%) (lit.)	M.p. (^{0}C) (lit.)
1	1 : 5	300	3.0	90 (73 [5])	200-201 (210-202[4])
2	1 : 2 - 5	300	2.0	95 (81[5])	159 (158-160[4])
3	1 : 5	400	4.0	94 (88[5])	130-131 (131-132[4])
4	1 : 5	400	3.5	96 (91[5])	98-99 (97-98[4])
5	1 : 2	600	4.0	92 (91[5])	83-64 (84-86[4])
6	1 : 1.5	300	3.5	95 (89[5])	178-180 (180-181[4])

The structure of *N*-alkylacridones **1-6** were confirmed based on melting points (Table 1) and their ^{1}H – NMR data (Table 2).

Table 2. Relevant ^{1}H-NMR data of *N*-alkylacridones **1-6**.

Compound	^{1}H-NMR (DMSO-d_6)
1 (R = Me)	3.80 (3H, s); 7.23-7.26 (2H, m); 7.53-7.58 (4H, m); 8.40 (2H, d).
2 (R = Et)	1.47 (3H, t); 4.46 (2H, q); 7.20- 7.23 (2H, m); 7.60 – 7.66 (4H, m); 8.39 (2H, d).
3 (R = *n*-Pr)	1.17 (3H, t), 1.94 (2H, q), 4.32 (2H, t); 7.20-7.23 (2H, m), 7.62-7.67 (4H, m); 8.40 (2H, d).
4 (R = *n*-Bu)	1.03 (3H, t); 1.57-1.59 (2H, m); 1.78-1.96(2H, m); 4.42 (2H, t); 7.24-7.29 (2H, m); 7.63 – 7.68 (4H, m); 8.41 (2H, d).
5 [R = $(CH_2)_2$-$CH(CH_3)_2$]	0.87 (6H, d); 1.46–1.48 (2H, m); 1.74 – 1.76 (1H, m); 4.59 (2H, s); 7.23-7.27 (2H, m); 7.56-7.60 (4H, m); 8.40 (2H, d).
6 (R = Bn)	5.61 (2H, s); 7.18-7.71 (11H, m); 8.42 (2H, d).

CONCLUSIONS

We succeeded to improve the *N*-alkylation methodology of acridone, using microwave irradiation. Indeed, in comparison with the earlier reported Wang and coworkers' protocol [5], our reactions occurred with the same or even better yields without the presence of a phase transfer catalyst.

EXPERIMENTAL SECTION

M.p. are uncorrected. For *N*-alkylation reactions, a microwave synthesis system Synthos 3000, Anton Par was used. ^{1}H-NMR spectra were recorded on a NMR Bruker Avance 300 spectrometer operating at 300 MHz and 75 MHz for ^{1}H and ^{13}C nuclei respectively. No $SiMe_4$ was added, chemical shifts were measured against the solvent peak.

GENERAL PROCEDURE FOR *N*-ALKLATION OF ACRIDONE

A mixture of acridone (0.98 g, 5 mmol), alkyl bromide (7.5-25 mmol) and 4 g of solid support (KF/Al_2O_3) were irradiated for the indicated time and power, as listed in Table 1. Subsequently, the reaction mixtures were cooled at room temperature and the crude products were purified by column chromatography on silica gel, using petroleum ether-ethyl acetate-dichloromethane as eluent.

REFERENCES

1. T. Long-Su, K. A. Watanabe, WO 9216509; cf. Chem. Abstr.*,* **1992**, *118*, 38775i.
2. R. J. Butlin, D. Glaver, EP 471516; cf. Chem. Abstr. **1991**, *116*, 235461r.
3. J. P. Galy, J. Elguero, E. J. Vincent, *Synthesis*, **1979**, 944.
4. H. Nishi, H. Kohno, T. Kano, *Bull. Chem. Soc. Jpn,* **1981**, *54*, 1897.
5. C. Wang, T. Hang, H. Zhang, *Synth. Commun*. **2003**, *33*, 451.
6. H. Kabashima, H. Tsuji, S. Nakata, Y, Tanaka, H. Hattori, *Appl. Catal.A: Gen.* **2000***,194-195*, 227.
7. T. Baba, *Catal. Survey Jpn*., **2000, *4*,** 17.

STUDIA UNIVERSITATIS BABEŞ-BOLYAI, CHEMIA, LIV, 2, 2009

THE STUDY OF HEAVY METALS TRANSFER FACTORS ON DIFFERENT TYPES OF AQUATIC VEGETATION

LILIANA TEODOROF, CRISTINA NASTASE, IRINA ANUTI[a]

ABSTRACT. In this study, there were selected two sample types: sediments and three types of aquatic vegetation from Danube Delta Biosphere Reserve: *Scirpo- Phragmitetum*, *Typha angustofila* and *Stratiotetum aloides*. The samples were taken during 2008, from may to august. For the aquatic vegetations the humidity, the total carbon and the heavy metals (Cd, Mn, Ni, Pb, Zn) concentrations in the dry samples were measured. For the sediments the heavy metals concentrations were measured. Accumulation factor ratios of aquatic vegetations were calculated, and the three species were compared. The bioaccumulation ratios of *S. aloides* were higher comparing with *T. angustofila* and *S. phragmitetum for* nickel, lead and manganese. The study of the humidity and total organic carbon proves the fact that the *T. angustofila* is an important viable source of biocombustible (minimum humidity, maximum content of carbon), than *S. phragmitetum* (medium humidity, medium content of carbon) and *S. aloides* (maximum humidity and minimum content of carbon).

Keywords: *heavy metals, total carbon, humidity, Scirpo-Phragmitetum, S. aloides , T. angustofila, Danube Delta*

INTRODUCTION

Due to their different capacity to retain heavy metals, three types of aquatic vegetation were selected. Heavy metals like cadmium and lead were insolubilized as sulphides or hydroxides in large amounts pH-dependent in the sediment and finally deposited in the rhizomes and partially in the above aerial parts of the plants [4].

Plants can attenuate water flow, bind sediment, and directly accumulate metals. By these actions plants affect metal mobility.

Because of their acute toxic effects, heavy metals should be removed from the environment using cost-effective and appropriate methods, or should be converted into less-toxic forms. Phytoremediation means the use of green plants to reduce, remove, degrade or immobilize environmental toxins. [6] [8] [11] [12]

---

[a] *Danube Delta National Institute for Research and Development, Str. Babadag, Nr.1.RO 820112, Tulcea, Romania, liliteodorof@indd.tim.ro*

In Danube Delta Biosphere Reserve, the dominant vegetation is the one specific for the swamps, as reed (*S. phragmitetum*) and rush (*T. angustofila*), which are helophila species. [1] The covering vegetation, under which have been developed peat deposits, is represented by *S. phragmitetum* association with tall reed (3–5m) in the areas characterized by an active circulation of fresh waters. The reed being located along the channels reduces the erosion of the river banks and helps in retaining of the sediments from flood water. The reed works as a self–driven system, optimizing the physical, chemical and microbiological processes which occur naturally in wet areas. Reed, like other plants which grow in the wet areas, conveys the atmospheric oxygen along the plant, through roots, in order to survive in the flooded soil.

The atmospheric oxygen transfer creates both aerobe and anaerobe conditions, which allows to an extraordinary variety of bacteria and fungi to grow. These are using organic pollutants as food source, reducing their concentration both in water and in soil [4]. The organic matter from water and soil are not only retained in reed but are also decayed there to harmless compounds. Other pollutants, heavy metals, are transformed from noxious ionic compounds and retained in soil by complexing chemical reactions [9]. In the last years, the aquatic vegetations (reed and rush) has been used in constructed wetlands for the treatment of industrial wastewaters containing metals. [6] [7]

S. aloides belongs to aquatic vegetation, it can be found in the shallow lakes, in the small pools located in rush-beds, in channels and in the banks of channels and brooks. Stratiotes is an underwater water plant species also known as “water soldiers”. A characteristic of the genus is the habit of the plants rising to the surface at flowering time. The plant appears to be associated with calcareous waters and there is a suggestion that changing levels of calcium carbonate on the leaves may explain the floating and submerging behavior.

The Dunavăț/Dranov region (19000ha) is one such peat area, lying as it does between two more or less parallel water courses: the Dunavăț Danube Branch in the north-west and the Dranov creek in the south-east. The Holbina/Dunavăț is situated in the Dunavăț/Dranov region and consists of three former fish-farm basins [5].

The aims of this study were to: (1) to compare the total humidity of reed, rush and stratiotes, (2) to compare the total organic carbon concentrations in the three types of aquatic vegetations, (3) to compare the the total heavy metals concentrations in the selected aquatic vegetations, (4) to evaluate the accumulations ratios oh heavy metals in reed, rush and stratiotes.

RESULTS AND DISCUSION

The pollutants in aquatic system are removed through a combination of biological, physical, and chemical processes including assimilation by plant tissue, microbiological transformations, sedimentation, precipitation, and adsorption to sediment particles. [2]

The study of heavy metals accumulation, proves that the inorganic pollutants have a different rate of accumulation in the aquatic vegetation

Tables 2 and 3 show the maximum, minimum, average, median and standard deviations values of the 25-th measurements of selected indicators for each sample type (sediment and aquatic vegetation from Dunavat and Holbina respectively), calculated using the excel interface.

In a totally ordered set, all elements are mutually comparable, so such a set can have at most one minimal element and at most one maximal element. Then, due to mutual comparability, the minimal element will also be the least element and the maximal element will also be the greatest element. Thus in a totally ordered set we can simply use the terms minimum and maximum. *T. angustofila* has the lowest minimum humidity value and the highest minimum total organic carbon value. In opposite, *S. aloides* has the highest minimum humidity value and the lowest total organic carbon value. The same trend was observed with the maximum calculated values, for humidity and the total carbon.

An average or central tendency of a data set refers to a measure of the "middle" or "expected" value of the data set. The humidity average has values between 40.671% and 93.076%. The *S. aloides* samples had the maximum value for humidity and the minimum values were found in the *T. angustofila* samples.

It was necessary to evaluate the content of organic carbon, because in the Danube Delta Biosphere Reserve it is a high quantity of aquatic vegetation, a possible source for the biocombustible. The maximum concentration of organic carbon it was determined in the *S. phragmitetum* and *T. angustofila* samples.

The average of heavy metals concentrations, expressed in mg/kg of dry substances, were represented in figure 1. The *S. aloides* samples accumulated the maximum heavy metals, with no exception. (Figure 1)

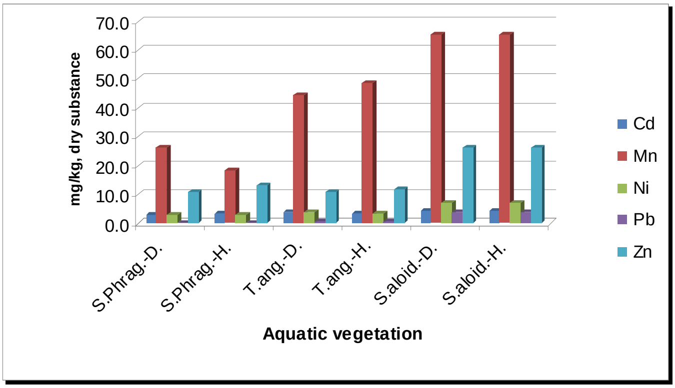

Figure 1. Total heavy metals medium concentrations in aquatic vegetation (D=Dunavat, H=Holbina)

A **median** is described as the number separating the higher half of a sample, a population, from the lower half. The *median* of a finite list of numbers can be found by arranging all the observations from lowest value to highest value and picking the middle one. If there is an even number of observations, the median is not unique, so one often takes the mean of the two middle values. At most half the population has values less than the *median* and at most half have values greater than the median. If both groups contain less than half the population, then some of the population is exactly equal to the median. The general distribution of the median is the same like the average, with the maximum values calculated in *S. aloides* .

In general, for all selected heavy metals, at Holbina and Dunavat, the calculated standard deviations have the lowest values (<1). A low **standard deviation** indicates that the data points tend to be very close to the average.

For the humidity and the total organic carbon, for the three type of aquatic vegetation, the standard deviations have high values. A high standard deviation indicates that the data are “spread out” over a large range of values.

As we can see, the both selected sampling points (Holbina and Dunavat) have the same general variation tendency of the statistical selected parameters: minimum, maximum, average, median, standard deviations. This can be explained by the fact the Danube Delta lakes are opened water, with channels and branches that assure the general input and output of the water.

Bioaccumulation factors which express the ratio of the metal concentration in the biological material to the metal concentration in soil or external solution were evaluated.[13], [3] It was found that the mobility within the chamomile plants decreased in the following order: Cd > Ni > Pb.

Tabel 1. Bioaccumulation factors in different aquatic vegetation

Sampling points	Sample type	BAF_{Cd}	BAF_{Mn}	BAF_{Ni}	BAF_{Pb}	BAF_{Zn}
Dunavat	*S.Phragmitetum*	0.823	0.074	0.082	0.010	0.283
	T. angustofila	1.779	0.254	0.125	0.018	0.281
	S. aloides	1.651	0.213	0.251	0.357	1.125
Holbina	*S.Phragmitetum*	1.039	0.050	0.085	0.009	0.361
	T. angustofila	1.150	0.221	0.102	0.017	0.320
	S. aloides	1.168	0.214	0.260	0.432	0.989

The bioaccumulation factor was calculated after the medium values of metals concentrations from aquatic vegetation and sediments, expressed in mg/kg of dry substance. By analyzing the values of bioaccumulation factors, we can observe the same general trend: $\mathbf{BAF_{Cd} > BAF_{Zn} > BAF_{Ni} > BAF_{Pb} > BAF_{Mn}}$. The calculated values of bioaccumulations factors are in interrelation with science literature. [13], [3]

Table 2. The minimum, maximum, average, standard deviation values of selected indicators from Dunavat area

Sample type	Parameter	Humidity	TOC	Cd		Mn		Ni		Pb		Zn	
		b	b	a	b	a	b	a	b	a	b	a	b
		%	mg/kg^1	mg/kg^1	mg/kg^1	mg/kg^1	mg/kg^1	mg/kg^1	mg/kg^1	mg/kg^1	mg/kg^1	mg/kg^1	mg/kg^1
S.Phragmitetum	**Min. value**	63.652	65.995	2.542	2.028	350.796	24.194	30.116	1.998	14.575	0.062	32.501	4.324
	Max. value	86.635	84.625	4.843	3.893	356.854	27.451	32.204	3.658	14.923	0.318	44.730	15.701
	Average	74.231	77.254	3.691	2.859	353.725	26.128	31.358	2.565	14.770	0.147	38.036	10.539
	Median	73.654	77.625	3.783	2.887	354.195	26.225	31.489	2.461	14.781	0.110	37.766	10.369
	Std. dev	4.801	5.171	0.647	0.501	1.663	0.793	0.618	0.376	0.102	0.077	2.820	2.617
T. angustofila	**Min. value**	30.401	71.464	1.025	2.544	326.014	41.238	28.421	3.124	14.603	0.177	35.640	8.154
	Max. value	56.481	86.426	3.887	5.122	335.120	48.946	30.984	4.547	14.795	0.365	40.950	12.521
	Average	40.671	78.666	2.526	3.750	331.177	44.224	30.056	3.750	14.712	0.258	37.951	10.625
	Median	40.164	79.456	2.630	3.764	331.687	44.075	30.034	3.678	14.728	0.241	37.917	10.514
	Std. dev	6.276	3.988	0.786	0.661	2.635	2.018	0.667	0.375	0.052	0.052	1.291	1.105
S. aloides	**Min. value**	86.464	38.481	2.368	3.980	306.490	65.221	27.752	6.944	10.962	3.902	23.199	26.100
	Max. value	97.004	63.461	2.435	3.999	306.858	65.417	27.804	6.978	11.008	3.937	23.239	26.139
	Average	93.076	52.388	2.418	3.992	306.687	65.287	27.771	6.962	10.980	3.923	23.223	26.116
	Median	93.161	52.164	2.420	3.992	306.701	65.259	27.770	6.962	10.983	3.928	23.230	26.115
	Std. dev	2.701	5.709	0.012	0.005	0.107	0.059	0.012	0.009	0.013	0.011	0.013	0.011

a=sediment sample
b=aquatic vegetation sample
^{1}=dry substance

Table 3. The minimum, maximum, average, standard deviation values of selected indicators from Holbina area

Sample type	Parameter	Humidity	TOC	Cd		Mn		Ni		Pb		Zn	
		b	b	a	b	a	b	a	b	a	b	a	b
		%	mg/kg^1	mg/kg^1	mg/kg^1	mg/kg^1	mg/kg^1	mg/kg^1	mg/kg^1	mg/kg^1	mg/kg^1	mg/kg^1	mg/kg^1
S.Phragmitetum	**Min. value**	59.043	54.461	2.097	2.448	358.134	15.337	30.712	2.028	14.615	0.065	34.053	10.968
	Max. value	79.024	73.325	4.325	4.254	367.890	22.364	32.387	3.554	14.920	0.263	38.173	14.335
	Average	71.826	64.285	3.388	3.240	363.627	18.341	31.580	2.675	14.836	0.131	35.835	12.890
	Median	73.365	63.645	3.503	3.122	363.757	18.654	31.667	2.684	14.859	0.114	35.906	12.857
	Std. dev	5.171	5.250	0.680	0.553	2.118	1.671	0.370	0.324	0.081	0.056	0.992	0.876
T. angustofila	**Min. value**	52.164	60.134	0.902	2.014	321.353	42.532	29.448	2.294	14.516	0.119	34.788	8.964
	Max. value	82.655	80.716	4.861	5.222	334.005	52.686	31.895	4.311	14.864	0.421	40.151	14.298
	Average	71.202	70.612	3.499	3.150	326.055	48.496	30.743	3.125	14.681	0.254	36.953	11.758
	Median	72.467	70.964	3.612	3.114	325.792	48.822	30.763	3.245	14.676	0.255	36.833	11.642
	Std. dev	8.249	5.886	0.968	0.790	3.207	2.473	0.654	0.481	0.079	0.069	1.436	1.344
S. aloides	**Min. value**	68.264	39.630	3.314	3.900	305.589	65.231	26.765	6.942	9.044	3.907	26.391	26.101
	Max. value	89.474	52.326	3.533	4.018	305.822	65.338	26.793	6.966	9.096	3.928	26.420	26.129
	Average	80.144	46.532	3.416	3.988	305.671	65.282	26.776	6.958	9.070	3.919	26.404	26.116
	Median	80.461	47.552	3.412	3.992	305.654	65.286	26.774	6.958	9.078	3.920	26.404	26.114
	Std. dev	6.589	3.449	0.038	0.021	0.065	0.036	0.008	0.006	0.018	0.006	0.008	0.007

a=sediment sample
b=aquatic vegetation sample
^{1}=dry substance

For all the heavy metals are made the flow charts and the calibration curves.

The coefficient R^2, for the calibration curves has the value 0.9994 (for cadmium), and 0.9997 (for lead) that represent a very good correlation between the intensity and the standards concentrations. (Figure 2 and Figure 3).

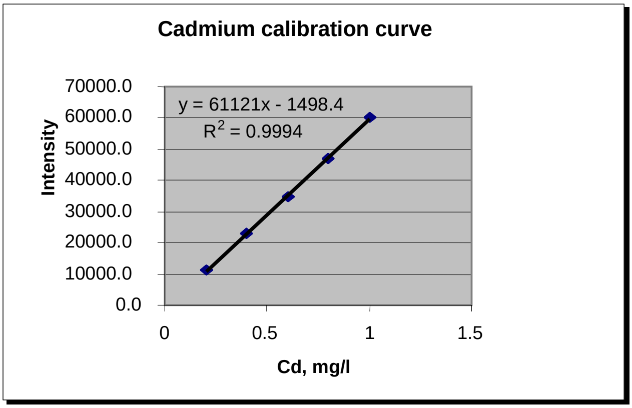

Figure 2. Calibration curve of cadmium

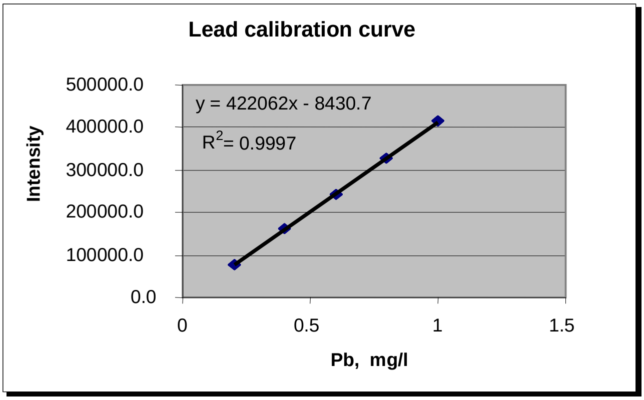

Figure 3. Calibration curve of lead

The quality control chart of cadmium was made in 2008, using a 0.6 ppm certified reference material PerkinElmer, according with a special procedure developed in our laboratory. The readings of 0.6 ppm standard at every cadmium samples measurements, assure a high quality control of analysis.

EXPERIMENTAL SECTION

In the field there were ten sampling points represented by aquatic vegetation and sediment samples. The samples are representative for Holbina Dunavat area. (Figure 4)

The aquatic vegetation samples (*S.phragmitetum*, *T. angustofila*, *S. aloides*) were taken with a reaper. Each sample is composed by the stems. The area where the samples were taken was 1 square meter. For each sample the humidity is determined by measurement and drying to the air oven, to 80 ^{0}C, until constant weight.

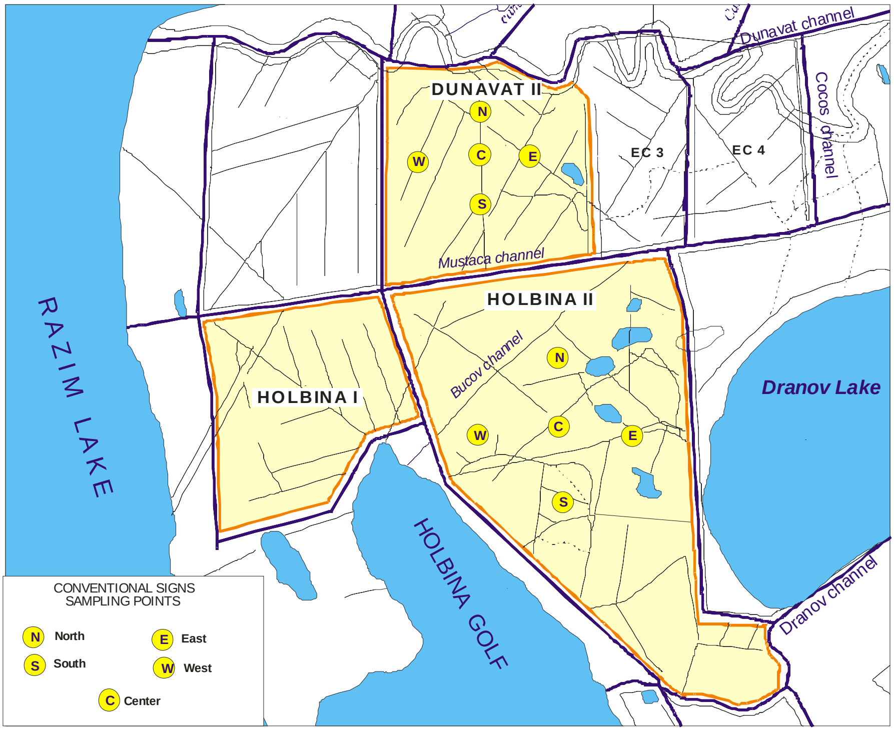

Figure 4. Sampling points of Holbina Dunavat area

The representative sample was obtained by the hashing of all the stems and the mixture until the homogenization.

The sediment samples are sampling according with SR ISO 5667 -12: September 2001- Water quality – Sampling, Part 12: Guidance on sampling of bottom sediments with dredge. The sediment samples were dried at room temperature, for avoid losing organic micro pollutant.

To obtain sub samples approaching 20g, it is made a pretreatment to a portion from the sample air-dried, grind fine and sprinkle through a sieve with meshes of 150 µm.

Reagents

All reagents used, have high chemical purity, and are Merck. The reagents used for organic carbon determination are: potassium bichromate, ($K_2Cr_2O_{7,}$ 1N), sulphuric acid (H_2SO_4 98%), Mohr salt (iron and ammonium double sulphate ($FeSO_4(NH_4)_2SO_4.6H_20$, 0.2N), ortho-phosphoric acid (H_3PO_4, 85%), biphenyl amine (colour indicator). For the heavy metals extraction we use nitric acid (HNO_3, 63%), and hydrogen peroxyde (H_2O_2), mainly used to increase the oxidizing effect of HNO_3 to destroy matrix residues.

Calibration solutions

The calibration curves were made using the Perkin Elmer Pure Plus Atomic Spectroscopy Standard, certified reference material 10 µg/ml, Multi-element ICP-MS calibration STD.3, matrix 5% HNO_3 The calibration curves are in five points and linear. Using the excell interface, it was calculated for each calibration curves, the equations and the coefficients R^2.

Instruments

Microwave digestion, necessary for heavy metals determination, according with EPA 3051/1994 - – Microwave assisted acid digestion of sediments, sludge, soil and plants for the determination of selected elements (Ag, Al, As, B, Ba, Be, Ca, Cd, Co, Cr, Cu, Fe, Hg, K, Mg, Mn, Mo, Na, Ni, Pb, Sb, Se, Sr, Tl, V, Zn); US EPA 3015/1994 – Microwave assisted acid digestion of aqueous samples and extracts.

Inductively coupled plasma – mass spectrometry (ICP-MS) is applicable to the determination of small concentrations of a large number of elements. When dissolved constituents are required, samples must be filtrated and acid-preserved before the analysis.

Acid digestion prior to filtration and analysis is required for groundwater, aqueous samples, industrial wastes, soils, sludge, sediments and other solid wastes [8].

The method measures ions produced by a radio-frequency inductively coupled plasma. Analyte species originating in a liquid are nebulized and the resulting aerosols are transported by argon gas into the plasma torch. The ions produced are entrained in the plasma gas and introduced, by means of an interface into a mass spectrometer. The ions produced in the plasma are sorted according to their mass-to-charge ratios and quantified with a channel electron multiplier. The analysis were made in the standard conditions of the instrument, without DRC.

Cell Gas A adjusts the flow rate of the first reaction cell gas. Cell Gas A (ml/min) specifies the flow rate in ml/min at which Cell Gas A flows into the reaction cell. The flow rate is controlled by a mass flow controller.

In the table bellow are represented the intrument experimental condition.

Table 4. Instrument experimental condition

Optimization Data		**Summary**		
Current value	**Description**	**Analyte**	**Mass**	**Meas. Intens. Mean**
0.91	Nebulizer Gas Flow [NEB]	Mg	24.0	37376.1
1.20	Auxiliary Gas Flow	In	114.9	30.9
15.00	Plasa Gas Flow	U	238.1	27.9
6.00	Lens Voltage	> Ce	139.9	88.5
1100.00	ICP RF Power	CeO	155.9	4.1
-1600.00	Analog Stage Voltage	> Ba	137.9	5264.9
750.00	Pulse Stage Voltage	Ba^{++}	69.0	175.6
0.00	Quadrupole Rod Offset Std [QRO]	220	220.0	0.8
-15.00	Cell Rod Offset Std [CRO]	8.5	8.5	1.1
15.00	Discriminator Threshold			
-13.00	Cell Path Voltage Std [CPV]			

The optimisation solution used, was ELAN 6100Setup /Stab./ Masscal. Solution. The optimisation solution contains the elements: Mg, Cu, Rh, Cd, In, Ba, Ce, Pb, U. The labeled concentrations are 10 ppb for each element. For one point, the measure time is about 3 minutes.

Sample preparation

The vegetation samples were dried until the constant mass, at 80^0C +/- 5^0 C. [10] The difference between the plant mass before and after drying process is a measure of drying substance and of water. In the humidity computing, the content of dry substance and water (humidity) are expressed in percentage, according with SR ISO 6496:2001: Fodders. The determination of humidity and other volatile substances.

A wet-oxidation technique is used for determining organic carbon in plant material. The oxidation is carried out by heating the plant sample with a mixture of potassium dichromate, sulphuric, and phosphoric acids for 10–15 min. The organic carbon is oxidation by chromic anhydride in excess, in the presence of sulphuric acid, at 100^0C temperature in 30 minutes. The excess of chromic anhydride are titrated with a Mohr salt 0.2N, in the presence of an oxido-reducing indicator. The content of organic carbon is computing after the chromic anhydride consuming for its oxidation. [14]

For the heavy metals determination, in quartz vessels are weighed to the analytical balance 0.25 -0.5 g of aquatic vegetation, in the 80 ml quartz digestion vessel, than added 5 ml nitric acids and 2 ml hydrogen peroxide.

After 15 minutes of pre-reaction time, the vessels are hermetic closed with the protective caps, are putting in the protective casings and put into the rotor of microwave oven.

The digest power program is presented in the table bellow.

Table 5. The digest program for aquatic vegetation

Phase	Power [W]	Ramp [min]	Hold [min]
1	1200	5.5	4.5
2	1400	0	5

After program and the cooling time end, the rotor is draw out, the digestion vessel are opened and the content is removed in graduated flask and dilute to 100 ml.

0.1 -0.2 g of well-mixed sediment samples are weighed to the analytical balance in the quartz digestion vessels and than added 10 ml concentrated nitric acid. If an intense reaction occurs, is allowed the reaction to stop before capping the vessel, after the pre-reaction, are putting in the protective casings and put into the rotor of microwave unit.

The digest power program is presented in the table bellow.

Table 6. The digest program for sediment

Phase	Power [W]	Ramp [min]	Hold [min]
1.	600	5.30	0
2.	1200	4.30	20

At the end of the microwave program, allow the vessels to cool for at least 10 minutes before removing them from the microwave unit. If the digested sample contains particulates which may clog nebulizer or interfere with injection of the sample into the instrument, the sample may be centrifuged, allowed to settle, or filtered, and then diluted in 100 ml graduated flask to 100 ml with distilled water and than analyzed to ICP-MS.

CONCLUSIONS

The study of the humidity and total organic carbon proves the fact that the *T. angustofila* is an important viable source of biocombustible (minimum humidity, maximum content of carbon).

The aquatic vegetation represents a real and a cheaper depolutting source for heavy metals and the nutrients, the major pollutants of the Danube River**.**

The *S. aloides* accumulated the maximum heavy metals, with no exception.

The bioaccumulation factor has the biggest values for cadmium and the minimum values for manganese.

The heavy metals calibration curves and flow charts assure high accuracy of measurements.

The future studies will be focused on the heavy metal accumulation in different morphological parts of aquatic vegetation, like roots, submerged stems, aerial stems, buds and rhizomes.

ACKNOWLEDGMENTS

The authors would like to thank to all the technical staff involved in developing of this project.

REFERENCES

1. M.J.G. Archer, R.A.Caldwell, *Journal Water, Air, & Soil Pollution*, **2004**, *157*, 257.
2. H. Brix, “The Use of aquatic macrophytes in water-pollution control, Wetland management, restoration and applications”, Centro Onternacional de altos estudios agronomicosmediterraneos, Instituto agronomico mediterraneo de Zaragoza 2002, Ambio Vol. 18, No2, **1989**, 100-107.
3. J.Cohen, P Cohen., S.G. West,. L.S. Aiken, “Applied multiple regression/ correlation analysis for the behavioral sciences”, Hillsdale, N.J: Lawrence Erlbaum Associates, **2003** (3rd ed.).
4. G Daeschlein., H Below., A Kramer, “Wastewater treatment and microbiologic hygienization with constructed wetlands and reed beds”, Institut für Hygiene der Ernst-Moritz-Arndt-Universität Greifswald, **2004**, www.oceans-esu.com.
5. H.J. Drost, D.Bos, M.Tudor, “Research for ecological restoration in the Dunavăț/ Dranov region, Danube Delta”*,* Riza-werkdocument, **2002**, nr. 188.
6. F. Duman, C Mehmet, S. Goksal, *Ecotoxicology,* **2007**, *16*, 457.
7. J.S. Dunbabin, K.H. Bowmer, *Sci Total Environ*, **1992**, *111*, 151.
8. Å. Fritioff, “Metal accumulation by plants evaluation of the use of plants in storm water treatment”, Doctoral Thesis in Plant, Physiology, Department of Botany, Stockholm University, SWEDEN, **2005.**
9. P Gastescu, R Stiuca, “Delta Dunarii, Rezervatie a Biosferei”, Editura Dobrogea **2006**, 197-202.

10. L. González, M.González-Vilar, “Handbook of Plant Ecophysiology Techniques, **2001**, 207-212.
11. I. Raskin, U. Kramer, R.D. Smith, D.E. Salt, *Rev. Plan Physiol*, **1997**, 114,1253.
12. D.E. Salt, R.D.Smith, *Ann Rev Plant Physiol* **, 1998**, *49*, 643.
13. I. Salamon, P.Labun, M.Skoula, M. Fabian, *Acta Hort. (ISHS)* **2007**, *749*, 231.
14. K.Shaw, *Eur. J. Soil Sci.***, 1959**,*10,* 316.
15.****SW US EPA Test Methods SW 846, **1992**, American Public Health Association, 18 th edition, 1-305.

STUDIA UNIVERSITATIS BABEŞ-BOLYAI, CHEMIA, LIV, 2, 2009

INVESTIGATION OF UNDERGROUND GAS PIPELINES CORROSION BY OPTICAL AND X-RAYS DIFFRACTION METHODS

ELEONORA MARIA RUS[a], CRISTIAN CALIN[b] AND IOAN BALDEA[a]

ABSTRACT. This work aims to determine the corrosion behavior of the buried gas pipelines (OLT 35 and OL 37 carbon steel) in salty and swampy soils by optical methods.

The aspect of the corroded surface and the nature of corrosion products were studied by metallographic microscopy and by X-ray diffraction. By analyzing the metallographic microscopy for OLT 35 corrosion in soils, one can observe that salty soil is more aggressive than swampy soils. The X-ray diffraction method shows that all types of soil contain the two phases of trivalent iron oxides, in beta and gamma hydrated form.

Keywords*: carbon steel, buried metallic pipelines, underground corrosion, surface analysis, X-ray diffraction, metallographic microscopy.*

INTRODUCTION

Underground metal structures are usually expected to have a long working life, often 50 to 100 years. Before such a network is put in place, the risk of corrosion and the need for corrosion protection measures should be estimated.

In principle, stainless steels should be in the passive state in soils, but the presence of water and aggressive chemical species such as chloride ions, sulfates and as well as various types of bacteria and stray current, can cause localized corrosion [1-4].

The soil is a corrosive environment that has special characteristics from one place to another because of the variable humidity, the different percent of dissolved salts, various pH, the presence of microorganisms, the variable quantity of oxygen and the presence of stray currents [5-7].

---

[a] *Babeş-Bolyai University, Faculty of Chemistry and Chemical Engineering,11 Arany Janos Str. Cluj-Napoca, RO-400084,Romania, norus@chem.ubbcluj.ro*

[b] *S.C.Distrigaz-Nord S.A. Targu-Mures, 95. Decebal Str, Cluj-Napoca, Romania, cristian.calin@distrigaznord.ro*

The pH value of soil is determined by the contents of carbonic acid, minerals (and/or their leaching), organic or inorganic acids (e.g. produced by microbial activity), and by industrial wastes or acid rain. The pH value of soil moisture also affects the solubility of the corrosion products [8-10].

Since corrosion is associated with electrochemical reaction the soil resistivity is a broad indicator of its corrosivity. The soil resistivity is widely used and generally considered to be the dominant parameter in the absence of micro-biological activity [1,5].

The most important factor of corrosion is the duration of steel surface exposure to water (wetting phase) and the presence of corrosion-stimulating agents in the moist zone. If the duration of exposure and the environment are known, it is possible to estimate the corrosion rate.

Electrochemical and optical methods are well suited for the study of corrosion phenomena because they allow one to simulate the corrosive effect of the environment [11]. Low carbon steel OLT-35, has been undertaken for corrosion study in swampy and salty soils and compared to other carbon steel for general usage as OL-37.

Metallographic investigation and surface analysis were made in order to evaluate the type of the corrosive attack .

RESULTS AND DISCUSSION

The chemical composition of the studied steels is given in Table1.

Table1. The content of various elements in the alloys

Steel type	***Weight %***					
	C	Si	Mn	P	S	Fe
OLT-35	0.17	<0.35	<0.40	<0.05	<0.05	Up to 100 %
OL-37	0.22	0.07	0.56	0.055	0.055	Up to 100 %

Some characteristics and the provenience of used soils are contained in table 2.

Table 2. Some characteristics of used soils

Soil type	***Provenience***	***pH***	***Conductivity (mS)***
Normal (ordinary)	Cluj-Napoca rail station zone	6.5	0.6
Salty	Ocna Dej, salt mine zone	6.7	3.5
Marshy	Cluj-Napoca Intre Lacuri district	7.0	10.2

1. Metallographic microscopy

This method analyzes corroded surfaces, after smoothing and polishing. It allows the observation of the corrosion effects in the depth of the metallic wall. Two types of carbon steel samples, the OLT 35 and OL 37, were undertaken, were buried into aggressive soils for 36 months and analyzed after such exposure. From figure 1 can be observed both the oxide layers formed and the surfaces attacked by corrosion (macroscopic observation) of OLT 35 and OL 37 steels, in swampy and salty soil.

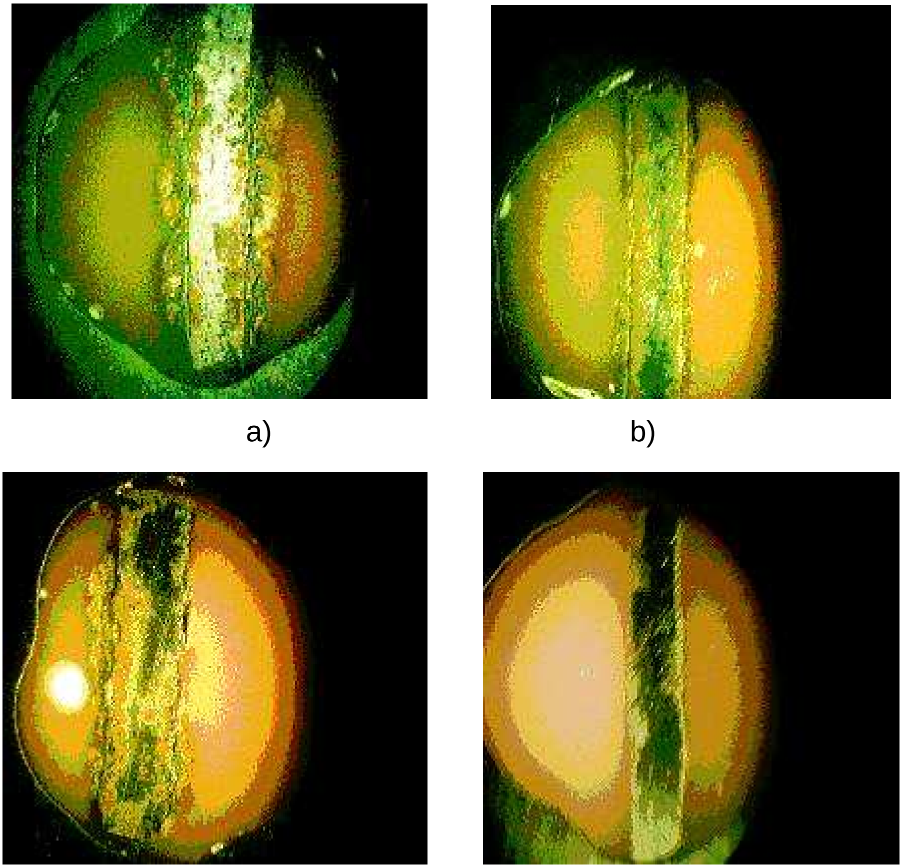

a) b)

c) d)

Figure 1. The aspect of samples surfaces comprised in resin after smoothing and polishing: OLT 35/swampy soil *ex situ* (a); OL 37/ swampy soil *ex situ* (b); OLT 35/salty soil *in situ* (c); OLT 35/salty soil *ex situ* (d). (X 63)

The metallographic microscopy is presented in figures 2 and 3 and the main observations are summarized in table 3.

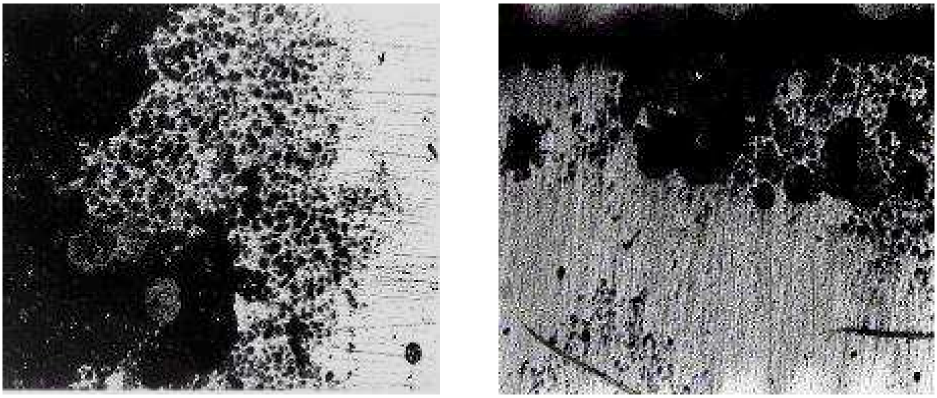

a) b)

Figure 2. Micrographs of the corroded surface in swampy soil *ex situ* : OLT 35 (a) and OL 37 (b). (X 63)

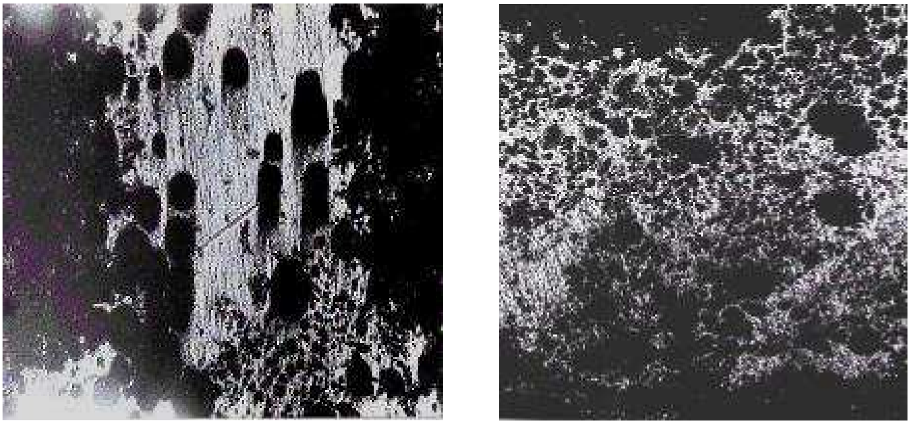

a) b)

Figure 3. Micrographs of the corroded surface of the OLT 35 in salty soil: *in situ* (a) and *ex situ* (b) (X 63)

Table 3. Observations noticed on the metallographic microscope

Steel type	Aggressive environment	Observations
OLT 35	***Salty soil*** *in situ*	- the thickness of the corrosion products layers is between 0.2 mm and 2.6 mm; - localized corrosion; - the most aggressive environment analyzed, on both sides of the sample, most of the surfaces are attacked by corrosion in the plagues form;
	Salty soil *ex situ*	- the thickness of the steel layers is approximately 0.2 mm; - the generalized corrosion, removed by smoothing, reveals localized attacks
	Swampy soil *ex situ*	- the thickness of the corrosion products layers is between 0.1 and 2.5 mm - localized corrosion; unlike the salty soil in which the pitting were of large and medium sizes, part of them are united in plagues; - the aggressivity of this type of soil is lower then that of the salty soil;
OL 37	***Swampy soil*** *ex situ*	- the thickness of the corrosion products layers is between 0.2 and 0.6 mm - localized corrosion with pitting of medium dimensions forming plagues;

2. Optical microscopy

This investigation aims to analyze the corrosion products structures formed at the interface soil/metal. The method allows getting a sight in the depth of the corrosion products layers. The representative images of the corrosion products formed during the exposure are presented in figures 4 and 5. The characteristics of the corrosion products are presented in the table 4.

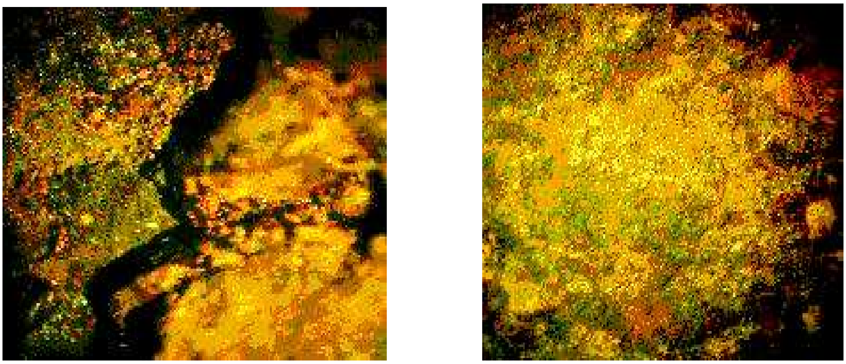

a) b)

Figure 4. The structure of the corrosion products formed in salty soil *in situ* on: OLT 35(a) and OL 37 steels(b) (X 50).

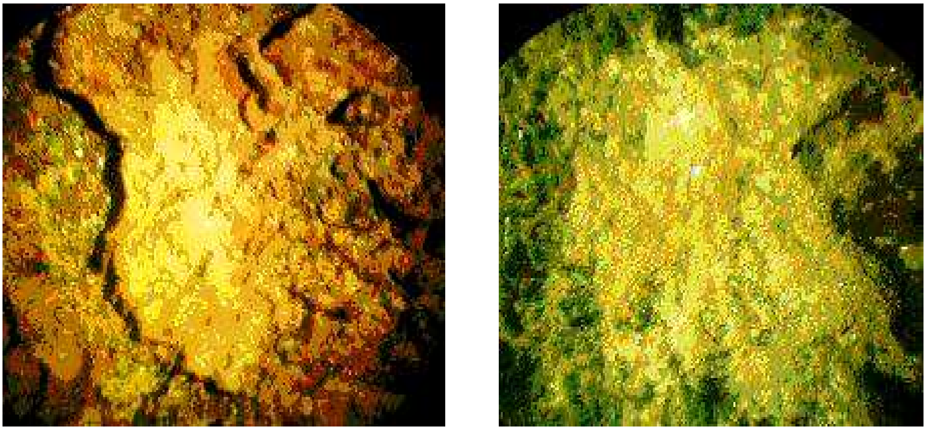

a) b)

Figure 5. The structure of the corrosion products formed in swampy soil *in situ* on : OLT 35 (a) and OL 37 steels (b) (X 50).

Table 4. The characteristics of the corrosion products formed on steels in different aggressive soils

Steel / electrolyte	***Characteristics of the formed corrosion products***
OLT 35 pipe / salty soil *in situ*	- porous product cakes of orange and red- brown colour, voluminous, quite thick, adherent, alternating with formations of different forms and thin layers; - it is observed the appearance of shiny formations, of black color; it does not appear in cases of other types of soil. The corrosion products contain, Fe_3O_4 or iron sulfides: FeS, FeS_2
OL 37 blade / salty soil *in situ*	- product cakes less porous, of red -brown color, less voluminous, more present on the edges of the sample, without conglomerates, smaller thicknesses then in the pipes case;
OLT 35 pipe / swampy soil *in situ*	- product cakes situated in the centre of the sample, red -brown color, smaller thickness then the one form the salty soil, bigger in the centre of the sample, with conglomerates of smaller dimensions on the edges, with smaller inclusions of black color (possible Fe_3O_4, FeS, FeS_2) on the edges of the sample; - the products are thinner then the ones in salty soil *in situ* and thicker than those *ex situ;*

3. X-rays diffraction

This study aims to make a qualitative and semi-quantitative phase analyses of the corrosion products. The diffractogramms of the corrosion products resulted form the corrosion of OLT 35/salty soil and OLT 35/swampy soil are presented in figures 6 and 7. The compounds identified in each type of soils are presented in table 5.

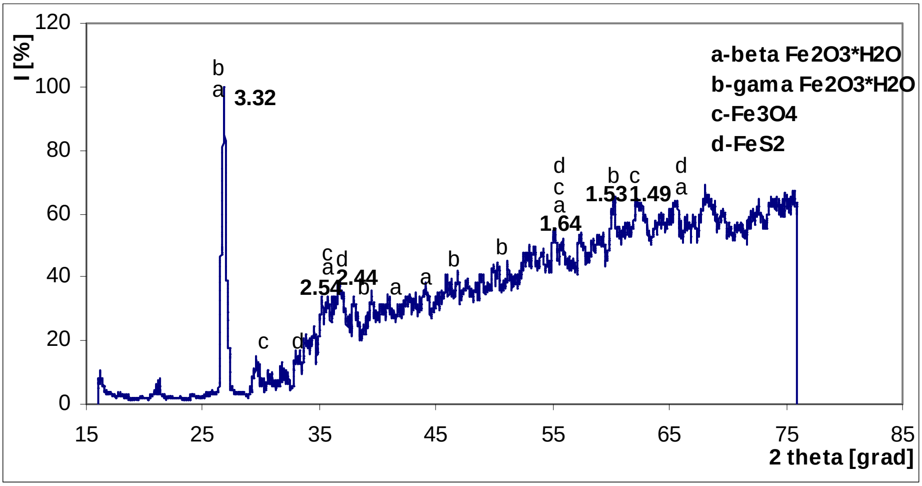

Figure 6. The diffractogramm obtained for the corrosion products from OLT 35/salty soil

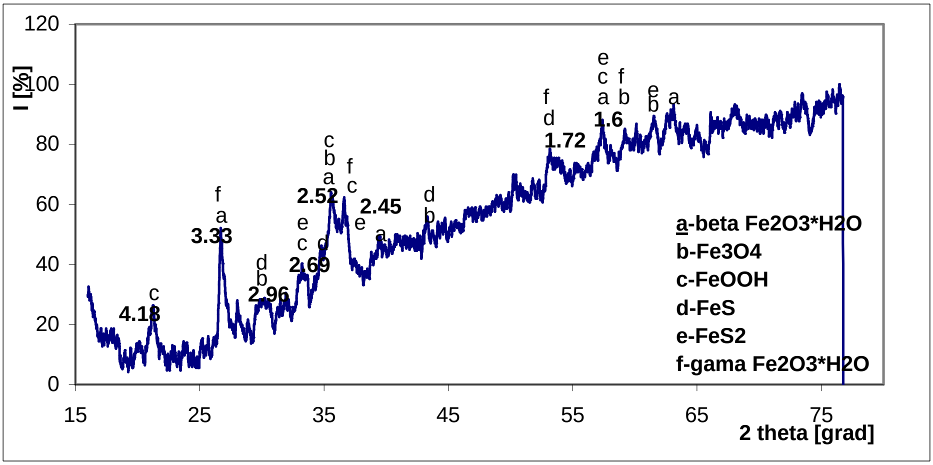

Figure 7. The diffractogramm obtained for the corrosion products from OLT 35/swampy soil.

The higher aggressiveness of swampy soil is confirmed by the various types of corrosion products. It can be observed that some of them are common for all types of soils: β-$Fe_2O_3*H_2O$; γ-$Fe_2O_3*H_2O$;

Table 5. The phase's component of the corrosion products.

OLT 35/ salty soil		***OLT 35/ swampy soil***	
Identified phases	*Mass composition %*	*Identified phases*	*Mass composition %*
β-Fe_2O_3*H_2O	43.03	β-Fe_2O_3*H_2O	22.9
γ-Fe_2O_3*H_2O	43.03	γ-Fe_2O_3*H_2O	22.9
Fe_3O_4	8.19	FeOOH	19.1
FeS_2	5.73	Fe_3O_4	19.1
		FeS	7.1
		FeS_2	8.74

CONCLUSIONS

The most aggressive non sterilized soil for OLT 35 carbon steel is the swampy soil, followed by the salty soil and normal soils. This fact is confirmed by the higher localized attack of the metallic surface, which is covered by corrosion defects (pitting and plague type with higher depth and diameters). The OLT 35 carbon steel is more affected as compared to OL 37 carbon steel in swampy soil. This test shows that in swampy soils, this material is not very useful to make pipes.

For selection purposes, it is recommended to consider corrosion resistance of buried stainless steels according to soil resisitivity and pH. Specific stainless steel grade must be carefully selected according to soil conditions.

By the determinations through diffraction with X-rays, it was put in evidence that all types of soil contain the two phases of trivalent iron rust, in beta and gamma form hydrated with one water molecule. The swampy soil contains two phases of sulfides that confirms the increased aggressivity by high chemical and bacteriological charge. After analyzing the products of corrosion, in the case of the steel OLT 35, in salty soil, the thickness of the corrosion products layers is higher than in the case of the OL 37 steel, which confirms that OLT 35 is more sensitive to corrosion in salty environments than OL 37.

Taking into consideration the relative high corrosion susceptibility in such aggressive environments, the OLT 35 carbon steel pipeline buried in soils should therefore be coated and cathodically protected.

EXPERIMENTAL SECTION

1. Metallographic microscopy

For performing the metallographic microscopy, a microscope of Neophot 21 type, made by Carl Zeiss Jena (GDR) has been used, with incorporated camera. In this case the determinations have been realized at a magnification of 63 times. For this purpose, the samples have been processed by smoothing with metallographic paper of different granulations and by polishing with felt impregnated in alumina suspension

2. Optical microscopy

A Carl Zeiss Jena binocular microscope, which works by reflection has been used. Unlike the metallographic microscopy, in which it could be analyzed only metallographic slides, in this case any kind of samples can be analyzed The determinations have been performed on the samples taken out from the aggressive environments both in pipe form and in blade form, without smoothing or polishing.

3. Analysis of corrosion products by X-rays diffraction

The phases analysis has been performed by an X-rays diffractometer of DRON 3 type (made in USSR).

The corrosion products samples were powder. The phases were identified by comparing with both American (ASTM) and Russian standards. The angles of the maximum diffraction and their intensity were measured on the diffractogramms. Relative intensities, I/I_1 and the interplanes distance, d were computed by means of Bragg relation.

REFERENCES

1. A. Benmoussa and M. Hadjel, *J.Corrosion Sci.Eng.,* **2005**, *7,* 17.
2. Eleonora Maria Rus, I. Bâldea and C.Călin, *Studia Univ. Babes-Bolyai, Chemia*, **2007**, *3* 121.
3. I.Lingvay and N. Secreteanu, « Coroziunea retelelor de transport si distributie a gazelor naturale », Bucuresti, Ed. ICPE Bucuresti, **2000**.
4. D.Funk and G.Schoneich, “Corrosion and corrosion protection of buried high-pressure gas pipelines”,*4th International Conference CEOCOR’97*, 3-5 sept.,Vienna, **1997**, *S.* A1-A17.
5. M. C. Li, Z. Han, H.C.Liu and C.N. Cao, *Corrosion,* **2001**, *57, 913.*
6. Rim-rukeh, Akpofure Awatefe and J. Kehinde, *J.App. Sci. Research,* **2006**, 2, 466.
7. Benmoussa , M. Hadjel and M. Traisnel, *Materials and Corrosion,* **2006**, *57,* 771.
8. Eleonora Maria Rus, I. Bâldea and C. Călin, *Studia Univ. Babes-Bolyai, Chemia*, **2007**, *3,* 137.
9. C. Calin, I. Baldea, I.Lingvay, Eleonora Maria. Rus and G. Rus, “Corrosion behaviour of OLT 35 steel in neutral soils”***,*** *The 15th International Corrosion Congress-Frontiers in Corrosion Science and Technology*, September, 15-21, Granada, Spain, **2002**, CD.

10. C. Calin, I. Baldea and Eleonora Maria Rus, “Determination the corrosion rate and corrosion prevention for underground metallic structures”*, The 3rd International Conference - Study and Control of Corrosion in the Perspective of Sustainable Development of Urban Distribution Grid*, July 1-3, Petrosani, Romania, **2004**, 91.
11. C. Calin, I. Baldea and Eleonora Maria Rus, “Analysis of underground gas pipelines corrosion by optical methods. Corrosion control and its efficiency”*, The 4th International Conference URB-CORR- Study and Control of Corrosion in the Perspective of Sustainable Development of Urban Distribution Grid*, Sibiu, Romania, June, 9-11, **2005**, 182.

STUDIA UNIVERSITATIS BABEŞ-BOLYAI, CHEMIA, LIV, 2, 2009

DON'T GAMBLE WITH PHYSICAL PROPERTIES OF POLYMERS

ANTON A. KISS[a], ALEXANDRE C. DIMIAN[b], PIET D. IEDEMA[b]

ABSTRACT. This study investigates several possible thermodynamic options (Sanchez-Lacombe, SAFT, Flory-Huggins, Soave-Redlich-Kwong) available in designing polymerization systems. Various results are predicted by these models with respect to monomer-polymer separation and polymer properties. These results show that it is essential to choose the proper thermodynamic model in order to get reliable results from simulation. The low density polyethylene (LDPE) process is presented as an industrial case study.

Keywords: *polymerization systems, property model polymers, LDPE*

INTRODUCTION

Process system engineers use computer simulations to perform a variety of tasks, ranging from calculations of mass and energy balances to rating, sizing, optimization, dynamics modeling and performance evaluation of process alternatives that could reduce investment and operating costs. Nowadays, due to significantly improved computing power, an engineer can relatively quickly set up the basic simulation specifications (including the physical properties), process conditions and define a complex flowsheet. However, note that the solid base of any process modeling and simulation is represented by the physical properties models. Missing or inadequate physical properties can undermine the accuracy of a model or even prevent one from performing the simulation. Finding good values for inadequate or missing physical property parameters is the key to a successful simulation. Nevertheless, this depends strongly upon choosing the right estimation methods – issue already recognized in the world of chemical processes modeling by the axiom "*garbage in, garbage out*" which means that the simulation results have the same quality as the input data / parameters [1].

---

[a] *AkzoNobel, Research and Technology Center, Velperweg 76, 6824 BM, Arnhem, The Netherlands, tony.kiss@akzonobel.com*
[b] *University of Amsterdam, Nieuwe Achtergracht 166, 1018 WV Amsterdam, The Netherlands, a.c.dimian@uva.nl, p.d.iedema@uva.nl*

This article investigates the properties models most used in polymerization systems, by performing regressions and parameters fitting, and show by an industrial LDPE case study that different results are predicted with respect to monomer-polymer separation and polymer properties.

PROBLEM STATEMENT

In any polymerization system there is a separation of the polymer from monomer, which is recycled in case of incomplete conversion. Although the monomer-polymer separation may appear easy, this is not a trivial task because mixtures of small molecules and long-chain polymers are involved [2]. Therefore it is of utmost importance to opt for the suitable method in order to get reliable and meaningful results from the simulation.

The problem is how to select the right property model for which reliable parameters can be calculated, when insufficient experimental data is available. To solve this problem we investigate the most used properties models (e.g. Sanchez-Lacombe, SAFT, Flory-Huggins, Poly-SRK) available in polymerization systems, perform regression and parameter fitting, and show – by an industrial relevenat case study – that different results are predicted with respect to monomer-polymer separation and polymer properties. The property models used in this work describe with good accuracy the behavior of both conventional molecules and polymer chains.

As both conventional molecules and polymers are present in the process, the key physical properties of all types of molecules must be predicted with acceptable accuracy by the models used. A major advantage of using equation-of-state (EOS) is that pure-component parameters of many conventional molecules encountered in polymer processes are already available in literature [3,4]. Nevertheless there is a need to estimate somehow the binary interaction parameters for these models. Note that if the binary parameters are not fitted to experimental data all the models tested revealed unsatisfactory performance.

RESULTS AND DISCUSSION

In this work the high-pressure low-density poly-ethylene (HP-LDPE) system was selected as case study [5,6]. The flowsheet of this process as well as the most important specifications are shown in Figure 1. Ethylene is fed at 100℃ and 2025 bar to the mixing section, wh ere the recycle is added. The mixed stream is heated in a pre-heater where the temperature increases to 170℃. The heated stream is passed then through the tubular polymerization reactor (6 cm diameter and 940 m length).

The initiator (benzoyl peroxide) is fed at two different locations: reactor inlet and half of the reactor length. The reaction mixture leaves the reactor and goes to the high-pressure separation (HPS) flash operated at 250 bar. Here, about 95% of the monomer is separated and sent to the recycle mixer. The second flash is the low-pressure separator (LPS) that makes the final separation at 2 bar. The rest of the monomer is sent to the recycle mixer, while the LDPE is recovered at the bottom, at purity higher than 99%. The high- and low-pressure recycles of monomer are mixed, and then re-compressed at the same pressure as the fresh ethylene stream. The recycle is then mixed with fresh ethylene and fed again to the reactor.

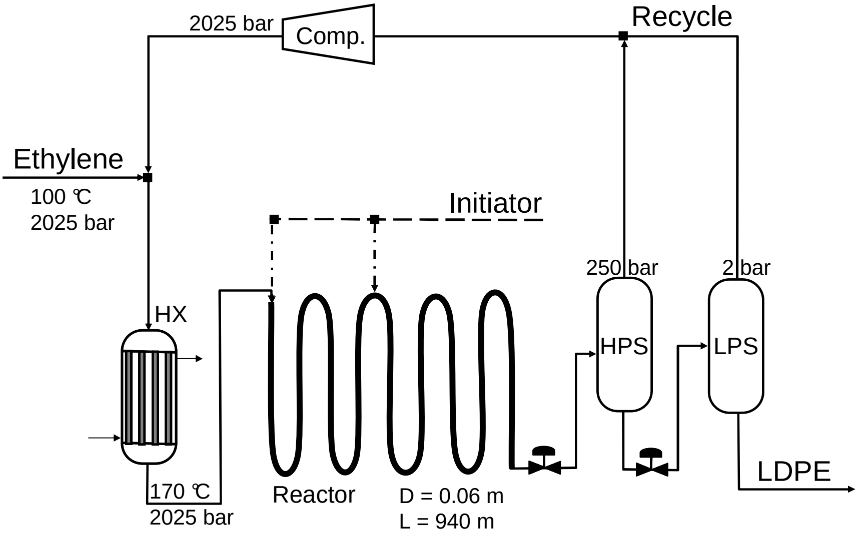

Figure 1. Flowsheet of the high-pressure LDPE process.

Experimental data was used to calculate the model parameters. The parameters should be segment-based or scalable for the size of the polymer. This condition is necessary because the size of the polymer changes in the process, and the model used must be able to accommodate this fact. Different results are predicted by the EOS models with respect to monomer-polymer separation and polymer properties. This has a major impact on the results of the simulation of a certain design. The results presented in this work for the LDPE system are an effective starting point in approaching other polymerization systems as well. Note that all calculations, including an industrial reactor simulations, were rigorously performed using the state-of-the-art software Aspen Polymers Plus that is a layered product built on top of AspenTech AspenPlus [7,8].

Note that each EOS properties model has exclusive characteristics that affect the results of modeling the pure monomer and polymer mixture behavior. Out of the four EOS models used, Sanchez-Lacombe and Poly-SRK EOS produced the best acceptable fit of the data. Both models are capable of predicting properties at both high and low-pressure, and give accurate results especially for high temperatures.

Table 1 lists the TPXY binary vapor-liquid equilibrium (VLE) data of the mixture ethylene-polyethylene (with number average molecular weight MW_n = 31700, and weight average MW = 247800) that have been used for regression [9]. The model parameters were calculated by regressing the experimental data.

Table 1. TPXY binary VLE data of the mixture ethylene-polyethylene

Temp. / K	Pressure / KPa	X, Ethylene	X, PE	Y, Ethylene	Y, PE
399.15	455.8	0.0018	0.9982	1	0
399.15	790.30	0.0037	0.9963	1	0
399.15	1135	0.0055	0.9945	1	0
399.15	1479	0.0075	0.9925	1	0
399.15	1824	0.0107	0.9893	1	0
399.15	2168	0.0136	0.9864	1	0
399.15	2513	0.0158	0.9842	1	0
399.15	2857	0.0175	0.9825	1	0
399.15	3202	0.0198	0.9802	1	0
399.15	3546	0.0221	0.9779	1	0
399.15	3891	0.0242	0.9758	1	0
399.15	4235	0.0255	0.9745	1	0
399.15	4580	0.0285	0.9715	1	0
399.15	4924	0.0305	0.9695	1	0
399.15	5269	0.0330	0.9670	1	0
399.15	5613	0.0359	0.9641	1	0
413.15	455.8	0.0015	0.9985	1	0
413.15	790.3	0.0034	0.9966	1	0
413.15	1135	0.0048	0.9952	1	0
413.15	1479	0.0068	0.9932	1	0
413.15	1824	0.0087	0.9913	1	0
413.15	2168	0.0112	0.9888	1	0
413.15	2513	0.0131	0.9869	1	0
413.15	2857	0.0151	0.9849	1	0
413.15	3202	0.0166	0.9834	1	0
413.15	3546	0.0189	0.9811	1	0
413.15	3891	0.0208	0.9792	1	0
413.15	4235	0.0235	0.9765	1	0
413.15	4580	0.0250	0.975	1	0
413.15	4924	0.0277	0.9723	1	0
413.15	5269	0.0296	0.9704	1	0
413.15	5613	0.0328	0.9672	1	0

Temp. / K	Pressure / KPa	X, Ethylene	X, PE	Y, Ethylene	Y, PE
428.15	455.8	0.0013	0.9987	1	0
428.15	790.30	0.0029	0.9971	1	0
428.15	1135	0.0039	0.9961	1	0
428.15	1479	0.0055	0.9945	1	0
428.15	1824	0.0074	0.9926	1	0
428.15	2168	0.0090	0.991	1	0
428.15	2513	0.0105	0.9895	1	0
428.15	2857	0.012	0.988	1	0
428.15	3202	0.0146	0.9854	1	0
428.15	3546	0.0164	0.9836	1	0
428.15	3891	0.0178	0.9822	1	0
428.15	4235	0.0207	0.9793	1	0
428.15	4580	0.0222	0.9778	1	0
428.15	4924	0.0242	0.9758	1	0
428.15	5269	0.0265	0.9735	1	0
428.15	5613	0.0286	0.9714	1	0

Table 2. Unary parameters for Sanchez-Lacombe EOS

Parameter Name / Element	Symbol	Units	Ethylene	PE
SLTSTR	T *	K	291	673
SLPSTR	P *	bar	3339	4250
SLRSTR	ρ *	Kg / m^3	660	887

Table 3. Binary parameters for Sanchez-Lacombe EOS

Parameter	Comp. i	Comp. j	Value (SI units)	Stand.-dev.
SLKIJ/1 (k_{ij})	PE	Ethylene	-0.09	0
SLETIJ/1 (η_{ij})	PE	Ethylene	-0.4040175	0.00428089

Table 4. Parameters of SAFT model

Parameter Name	Symbol	Ethylene	PE	$C_{14}H_{10}O_4$	$C_8H_{18}O_2$	Water
SAFTM	m	1.464	1133.72	11.993	7.51	1.54
SAFTV	v^{00}	18.157	12.0	12.13	12.30	14.14
SAFTU	u^0/k	212.06	228.36	208.93	206.17	188.86
SFTEPS	e/k	10	10	10	10	1

Table 5. Regressed binary parameters of SAFT model

Parameter	Comp. i	Comp. j	Value (SI units)	Stand.-dev.
SFTKIJ (k_{ij})	PE	Ethylene	0.08563059	0.00256897
SFTLIJ (l_{ij})	PE	Ethylene	0.00128981	0.00011733

Table 6. Mathias-Copeman constants required by the SRK-EOS model

Parameter	Comp. i	Comp. j	Value (SI units)	Stand. Dev.
FHCHI/1	PE	ethylene	5.929	0.657
FHCHI/2	PE	ethylene	-1437.673	272.593

Table 7. Parameters of the SRK-EOS model

Parameter Name / Element	Component	Value (SI units)
$T_{c,i}$	ethylene	303.211224
$P_{c,i}$	ethylene	130.667512
$T_{c,i}$	PE	1545.17701
$P_{c,i}$	PE	32.841247

Parameter Name / Element	Symbol	Ethylene	PE
RKSMCP / 1	$C_{I,1}$	0.656855	1
RKSMCP / 2	$C_{I,2}$	-0.362904	0
RKSMCP / 3	$C_{I,3}$	0.676711	0

For the **Sanchez-Lacombe** EOS the unary parameters (for ethylene and poly-ethylene) shown in table 2 were used. By fitting the experimental data presented in Table 1 the binary parameters (k_{ij} and η_{ij}) of the Sanchez-Lacombe EOS for the binary mixture ethylene-polyethylene have been regressed (Table 3).

The three unary parameters v^{00}, u^0 / k, and m for each component represent the necessary user input to apply ***Statistical Associating Fluid Theory (SAFT)*** to real fluid systems (together with the value of e/k). For fine tuning of mixture phase behaviour, the binary parameters k_{ij} and l_{ij} can be regressed to available phase equilibrium data. The values of these binary parameters are usually close to zero. The SAFT model parameters and their values are listed in Table 4.

The segment energy u^0/k and the segment volume v^{00} are *segmental parameter*s, which suggest that they should remain fairly constant between components in the same homologous series. The third parameter m represents the number of segments on the chain; this implies that m should be proportional to the molecular mass. In the case of normal alkanes, Huang and Radosz proposed the following generalized correlations for the pure-component parameters [10]:

$$m = 0.70402 + 0.046647 \cdot MW \quad (1)$$

$$mv^{00} = 11.888 + 0.55187 \cdot MW \quad (2)$$

$$u^0 / k = 210 - 26.886 \cdot e^{-0.013341 \cdot MW} \quad (3)$$

The unary parameters (m, v^{00} and u^0/k) for the initiators and water were calculated using the above equations. The regressed binary parameters k_{ij} and l_{ij} of the SAFT EOS are presented in Table 5.

The binary parameters α_{ij} and β_{ij} of the ***Flory-Huggins*** activity coefficient model for the binary mixture ethylene-polyethylene have been found by regressing the same set of experimental data. For the unary parameters of ethylene and polyethylene we had to use the default value (one) in our data regression simulation (DRS).

In order to use the polymer ***Soave-Redlich-Kwong (SRK)*** EOS, the pure components parameters needed are the critical constants T_c, P_c and the Mathias-Copeman constants. Tables 6 and 7 present the unary and binary parameters of the models.

Polymers are not supposed to vaporize, and therefore for the critical temperature of the polymers a high value is recommended (typically $T_c >$ 1000 K). For the same reason, a relatively low critical pressure is needed ($P_c < 10^6$ N/m^2). For all of the Mathias-Copeman parameters for oligomers and polymers, zero is recommended due to unavailability of information on polymer vapor pressure.

The identification of the model parameters requires the regression of the parameters $T_{c,i}$ and $P_{c,i}$ (critical temperature and critical pressure respectively) for ethylene and polyethylene. To this end the TPXY binary vapor-liquid-equilibrium data of ethylene-polyethylene, together with the Mathias-Copeman parameters (for ethylene and PE) have been used.

The results of the data regression simulations for all models considered are presented in Figure 2. The lines (solid, short- and long-dashed) represent the regressed equations while the dots represent the experimental values. In all cases, there is a good agreement between the predictive model and the experimental data, both at high and low-pressure and especially at higher temperatures. Yet, note that practically it is almost impossible to get accurate experimental data at supercritical conditions.

Figure 3 shows that different polydispersity (A, B and C) and reactor temperature profiles (D) are predicted by the property models investigated. This has a significant impact on the results of the simulation of a certain polymerization process design. For example, the final polydispersity index predicted by Sanchez-Lacombe and SAFT is ~6 (Figure 3B), while Florry-Huggins and SRK-EOS predict a PDI of ~2.5 (Figure 3A and 3C) – these figures corresponding to different end properties of the LDPE polymer. In terms of temperature the differences can be as high as 100 °C, thus making the design of an efficient reactor cooling system questionable (Figure 3D). The comparison of the simulated results with industrial data for the LDPE processes shows that the SRK-EOS provides the best estimates; hence Poly-SRK EOS should be used for reliable simulations of LDPE.

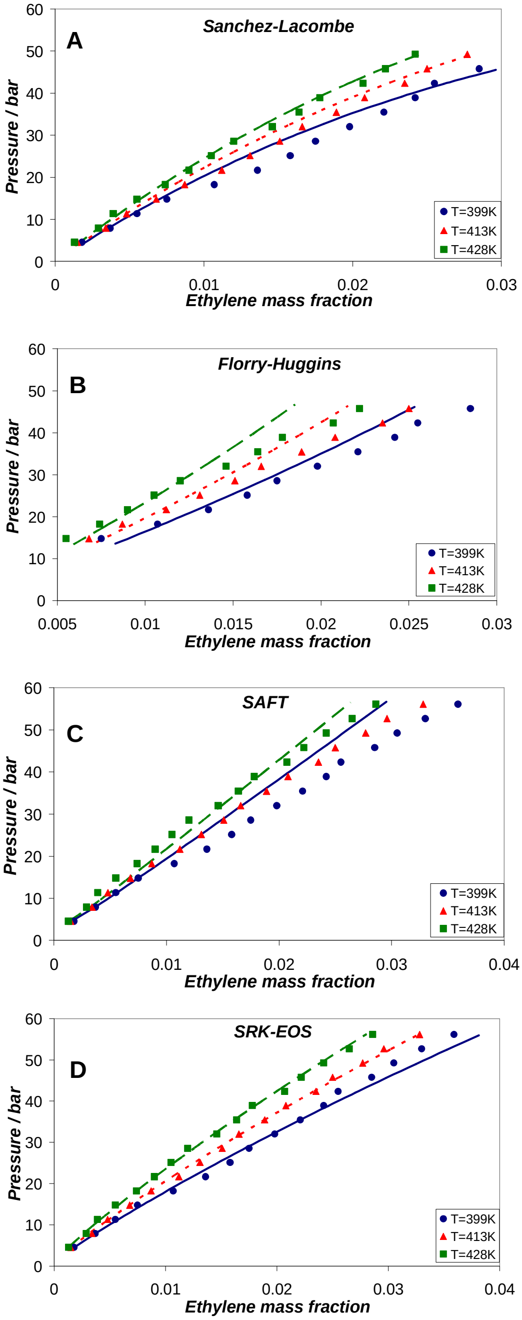

Figure 2. Vapor pressure vs mass fraction of ethylene, regressed and experimental data.

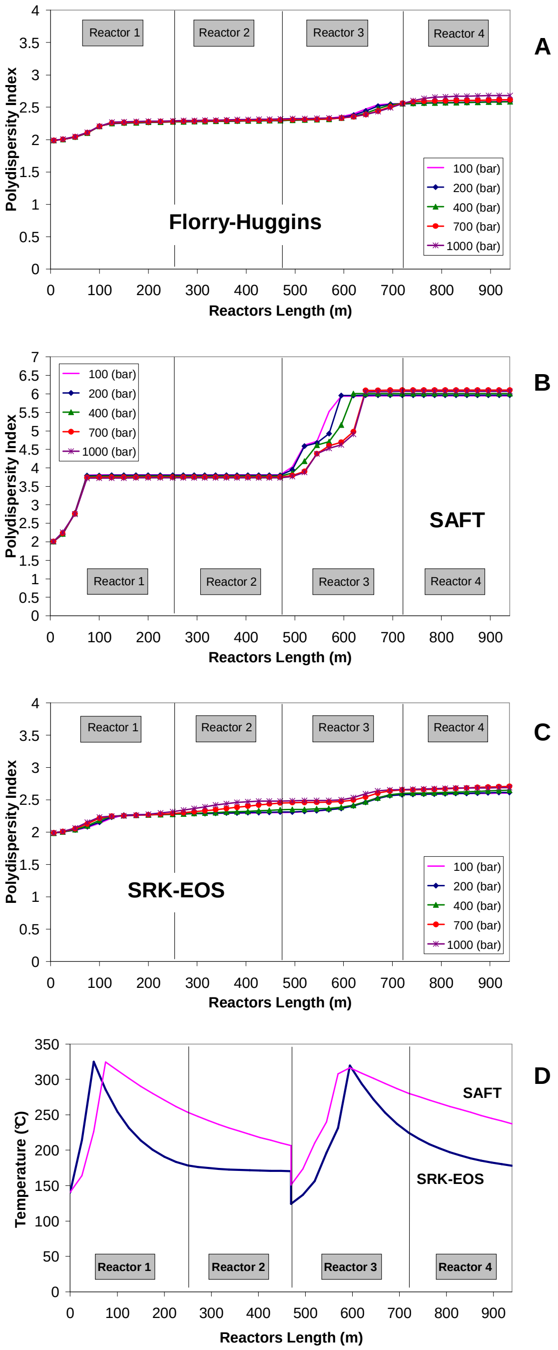

Figure 3. Polydispersity index (PDI) and reactor temperature profiles.

CONCLUSIONS

As both conventional molecules and polymers are present in the process, the key physical properties of all types of molecules must be predicted with acceptable accuracy by the thermodynamic models used.

Using an EOS has the advantage that pure-component parameters of many conventional molecules encountered in polymer processes are already available in literature. Yet, there is a need to estimate the binary interaction parameters for these models. If the binary parameters are not fitted to experimental data all models reveal unsatisfactory performance.

This study shows that all models offer a good fit of the data for the binary mixture ethylene-polyethylene. However, different monomer-polymer properties are predicted by the models investigated in this work. This has a significant impact on the results of the simulation of a certain polymerization process design. For the industrial LDPE case study the predicted reactor profiles have relatively large differences in the polydispersity index and the reaction temperature. Based on the comparison of the simulated results with data from the industrial plant, the Poly-SRK EOS proved to give the most reliable estimates. Note that the results presented in this work can be also used as a starting point in approaching other polymerization systems.

ACKNOWLEDGMENTS

We thank Abdelghani Belkou, as well as Aspen Technology for the excellent technical support.

NOTATION

MW – Weight average molecular weight
MW_n – Number average molecular weight
PDI – Polydispersity index (PDI), $\mathrm{PDI} = \mathrm{MW} / \mathrm{MW}_n$
P – Pressure, bar
P_c – Critical pressure, bar
T – Temperature, K
T_c – Critical temperature, K
X – Mass fraction in liquid phase
Y – Mass fraction in vapor phase
α_{ij}, β_{ij} – Binary interaction parameters (BIP), Flory-Huggins
k_{ij}, η_{ij} – Binary interaction parameters (BIP), Sanchez-Lacombe
k_{ij}, l_{ij} – Binary interaction parameters (BIP), SAFT
ρ – Density, kg / m^3
m – Number of segments on the chain
u^0/k – Segment energy
v^{00} – Segment volume

REFERENCES

1. E. C. Carlson, *Chemical Engineering Progress*, **1996**, *10*, 35.
2. A. A. Kiss, S. P. Agachi, *Hungarian Journal of Industrial Chemistry*, **1999**, *27*, 117.
3. H. Orbey, C. P. Bokis, C. C. Chen, *Industrial and Engineering Chemistry Research*, **1998**, *37*, 1567.
4. H. Orbey, C. P. Bokis, C. C. Chen, *Industrial and Engineering Chemistry Research*, **1998**, *37*, 4481.
5. A. A. Kiss, C. S. Bildea, A. C. Dimian, P. D. Iedema, *Chemical Engineering Science*, **2002**, *57*, 535.
6. A. A. Kiss, C. S. Bildea, A. C. Dimian, P. D. Iedema, *Chemical Engineering Science*, **2003**, *58*, 2973.
7. AspenTech Inc., *Aspen Polymers Plus 2004.1 – User Guide*, vol. 1 and 2, **2004**.
8. AspenTech Inc., *Aspen Polymers Plus 2004.1 – Examples & Applications*, **2004**.
9. W. Hao, H. S. Elbro, P. Alessi, *Chemistry Data Series*, XIV, DECHEMA **1992**.
10. H. H. Stanley, M. Radosz, *Industrial and Engineering Chemistry Research*, **1990**, *29*, 2284.

STUDIA UNIVERSITATIS BABEŞ-BOLYAI, CHEMIA, LIV, 2, 2009

SCREENING AND RESPONSE SURFACE MODELING OF WATER VAPOR ADSORPTION FROM WET AIR IN PACKED BED OF SILICA GEL USING D-OPTIMAL DESIGN

MARIUS SEBASTIAN SECULA*, RODICA DIACONESCU,
STELIAN PETRESCU

ABSTRACT. The experimental design methodology was applied for screening and response surface modeling of adsorption of water vapors from air on a fixed bed of silica gel grains. The variables considered were the air flow rate, temperature, air relative humidity and drying time. The D-optimal design allowed developing a quadratic model as a functional relationship between packed-bed adsorption efficiency and the independent variables. It was found that all factors considered have an important effect in the degradation efficiency of the organic matter**.**

Keywords: *D-optimal design, response surface modeling, air drying; adsorption; fixed bed.*

INTRODUCTION

Mathematical modeling of gas drying by adsorption in fixed bed was approached in a several papers reported in literature [1-9]. Theoretical studies suggested analytical mathematical models available when the process takes place in fixed bed of adsorbent under isotherm regime [1-4] and adiabatic or non-adiabatic regime respectively [5-9]. The suggested models are based on linear and non-linear equilibrium equations, considering the external and internal diffusion. However, due to the assumed hypothesis, the applicability of analytical models is limited, and their correlation rather weak.

The present work presents a preliminary study of applying experimental design screening and modeling at gas drying by adsorption in fixed bed of silica gel under non-isothermal and non-adiabatic conditions. It was decided to use D-optimal design, as this is an effective method for obtaining maximum information with a minimum of experiments, and to determine which factors significantly influence the measured variables. Air flow rate, temperature, air relative humidity and drying time were considered as independent variables,

---

* *"Gh. Asachi" Technical University of Iasi, Faculty of Chemical Engineering and environmental Protection, Department of Chemical Engineering, 71 Bd. Mangeron, Iasi, 700050, Romania, mariussecula@ch.tuiasi.ro*

while packed-bed adsorption efficiency was selected as response. A quarter polynomial model was suggested, tested and validated using experimental data unemployed in the D-optimal design.

RESULTS AND DISCUSSION

Several results obtained at air drying by adsorption in fixed bed of ordered silica gel under various experimental conditions are shown in Figure 1. The normalized concentration of water vapors in air at the output of a packed bed column as determined from psychrometric measurements is plotted as a function of the adsorption time.

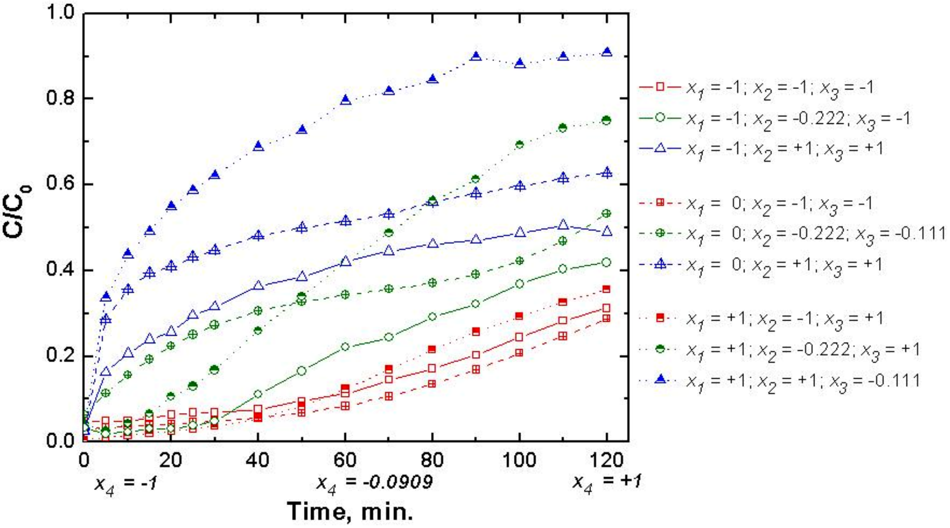

Figure 1. Several breakthrough curves achieved at air drying in fixed bed of silica gel at ranges of flow rate between 0.6 $m^3 \cdot h^{-1}$ and 1.2 $m^3 \cdot h^{-1}$, temperature from 20 to 38 °C and air relative humidity between 40 and 85 %.

The experimental data (Table 7) were analyzed by the Multi Linear Regression (MLR) method [10] to fit the second-order polynomial equation [11]:

$$Y = \beta_0 + \sum_{i=1}^{4} \beta_i \cdot x_i + \sum_{i=1}^{4} \beta_{ii} \cdot x_i^2 + \sum_{i=1}^{3} \sum_{j>i}^{4} \beta_{ij} \cdot x_i \cdot x_j + \varepsilon \tag{1}$$

where β_0, β_i, β_{ii}, and β_{ij} are regression coefficients (β_0 is a constant term, β_i is a liner effect term, β_{ii} is a squared effect term, β_{ij} and is an interaction effect term) and Y is the predicted response value. MLR is based on finding the regression model that minimizes the residual sum of squares of the response.

A D-optimal experimental design generated by the MODDE software with 20 runs and 2 replicates considered (Table 1) was employed for screening and response surface modeling. The algorithm used by this software is the modified Federov algorithm [12] with the Bayesian modification [13]. D-optimal designs select points from the candidate set that maximize the determinant of the coded model matrix *X'X*, which is equivalent to maximizing the volume of *X'X*.

As response for modeling, the packed-bed adsorption efficiency, *Y,* was considered and calculated by the following expression:

$$Y=\frac{1}{\tau_{\exp}}\int_{0}^{\tau_{\exp}}\left(1-\frac{C}{C_0}\right)d\tau \tag{2}$$

where C_0 (kg m^{-3}) is the initial concentration of water vapors in air, C (kg m^{-3}) is the concentration of water vapors in air at the column output; and $\tau_{\exp}$ – adsorption time (min.). The experimental results of the packed bed adsorption efficiency, *Y*, were determined according to planned initial conditions and reported in the last column of Table 1.

Table 1. Experimental design and results of the fractional design.

Run No.	Input variables								Response
	Flow rate, m^3/h	x_1	Temp., °C	x_2	Rel. humid., %	x_3	Time, min.	x_4	Y, non-dimens.
1	0.9	0	20	-1	40	-1	10	-1	0.96673
2	1.2	+1	27	-0.222	40	-1	10	-1	0.96625
3	0.6	-1	38	+1	40	-1	10	-1	0.92096
4	0.6	-1	20	-1	60	-0.111	10	-1	0.95083
5	1.2	+1	38	+1	60	-0.111	10	-1	0.71292
6	1.2	+1	20	-1	85	+1	10	-1	0.98991
7	0.6	-1	27	-0.222	85	+1	10	-1	0.94981
8	0.9	0	38	+1	85	+1	10	-1	0.76118
9	1.2	+1	20	-1	40	-1	60	-0.09	0.96354
10	0.6	-1	27	-0.222	40	-1	60	-0.09	0.91802
11	0.9	0	20	-1	85	+1	60	-0.09	0.95442
12	0.6	-1	20	-1	40	-1	120	+1	0.94049
13	0.6	-1	38	+1	40	-1	120	+1	0.70795
14	1.2	+1	38	+1	40	-1	120	+1	0.36872
15	1.2	+1	20	-1	60	-0.111	120	+1	0.66062
16	0.9	0	27	-0.222	60	-0.111	120	+1	0.67160
17	0.6	-1	20	-1	85	+1	120	+1	0.86288
18	1.2	+1	20	-1	85	+1	120	+1	0.85197
19	0.6	-1	38	+1	85	+1	120	+1	0.61635
20	1.2	+1	38	+1	85	+1	120	+1	0.35360
21	1.2	+1	38	+1	85	+1	120	+1	0.36195
22	1.2	+1	38	+1	85	+1	120	+1	0.34647

Screening is the first stage of an investigation where the goal is just to identify the important factors. The MODDE software allowed determining the coefficients of the second order fitting equation, which was analyzed based on the above-mentioned statistical criteria. In particular, the suitability of the screening model was tested by the ANOVA test. Table 2 summarizes the obtained results.

Table 2. Analysis of variance (ANOVA) for the screening modeling.*

Source of variation	Degrees of freedom	Sum of Squares	Mean Square (Variance)	F-ratio	p-value	Standard Deviation
Total	22	13.9077	0.63217			
Constant	1	12.8246	12.8246			
Regression	14	1.0678	0.07623	34.9544[a]	0.000	0.276176
Residual	7	0.0153	0.00218			0.046713
Lack of Fit (model error)	5	0.0151	0.00303	50.3777[b]	0.020	0.055053
Pure Error (replicate error)	2	0.0001	0.00006			0.007756
Total corrected	21	1.0831	0.05158			0.227104

*$R^2 = 0.9859$; $R^2_{adj} = 0.9577$; $Q^2 = 0.8254$.

[a] F-ratio (regression/residual); $F_{(0.1,\ 14,\ 7)} = 2.64$; $F_{(0.05,\ 14,\ 7)} = 3.53$; $F_{(0.01,\ 14,\ 7)} = 6.36$;

[b] F-ratio (lack of fit/pure error); $F_{(0.1,\ 5,\ 2)} = 9.29$; $F_{(0.05,\ 5,\ 2)} = 19.3$; $F_{(0.01,\ 5,\ 2)} = 99.3$.

In the ANOVA test, the *F*-ratio value obtained for the response is higher than the Fisher's *F*-value corresponding to a probability of 99% ($F_{(0.01,\ 14,\ 7)} = 6.36$), and so one can conclude that the variations that occur in the responses are associated to the model, not to random errors. *F*-ratio value obtained for the lack of fit is lower only than the Fisher's *F*-value at 99% probability ($F_{(0.01,\ 15,\ 2)} = 99.3$), which emphasize a poor model adequacy. The value of R^2 indicates that 98.59% of the response variability is explained by the model.

After the analysis of the second order model correlation and adequacy, the statistically significant variables and/or interactions were identified by means of p-value (< *0.1*). From *p*-values reported for each MLR equation factors, parameters and interactions are considered influent or not. Moreover, for one given parameter, the smallest the *p*-value is, more influent is this parameter onto the model. The scaled and centered coefficients of model fitted are resumed in Table 3. It can be seen that the process variables and interactions that are statistically significant are the flow rate (x_1), its interactions with temperature (x_1*x_2) and time (x_1*x_4), temperature (x_2), its interactions with time (x_2*x_4), time (x_4) and quadratic term of relative humidity (x_3^2) due to these parameters present p-values lower than *0.1* (for *90 %* of statistical meaning).

Table 3. Estimates of the screening model regression for packed-bed adsorption efficiency.

Real variables	Term	Estimate	p-value
Constant	Intercept	0.766762	$1.01464 \cdot 10^{-6}$
Flow rate (M_v)	x_1	-0.061249	$1.31372 \cdot 10^{-3}$
Temperature (T)	x_2	-0.128828	$1.63306 \cdot 10^{-5}$
Relative humidity (u)	x_3	-0.016199	***0.2204*** **(!)**
Time (t)	x_4	-0.116779	$1.98756 \cdot 10^{-5}$
M_v * M_v	x_1^2	0.019252	***0.5106*** **(!)**
T * T	x_2^2	-0.025020	***0.4286*** **(!)**
u * u	x_3^2	0.064716	$6.31456 \cdot 10^{-2}$
t * t	x_4^2	-0.030894	***0.3827*** **(!)**
M_v * T	$x_1 * x_2$	-0.039980	$1.81612 \cdot 10^{-2}$
M_v * u	$x_1 * x_3$	0.011961	***0.3866*** **(!)**
M_v * t	$x_1 * x_4$	-0.040362	$1.61997 \cdot 10^{-2}$
T * u	$x_2 * x_3$	-0.013064	***0.3593*** **(!)**
T * t	$x_2 * x_4$	-0.039177	$1.74276 \cdot 10^{-2}$
u * t	$x_3 * x_4$	0.005222	***0.7027*** **(!)**

In Figure 2 is shown the normal probability plot of effects (double of the absolute values of coefficients) emphasizing the amplitude of the effects influence over the objective function. As can be noticed, all of the insignificant effects, disposed on the linear fit, belong to the insignificant coefficients having p-values higher than *0.1*.

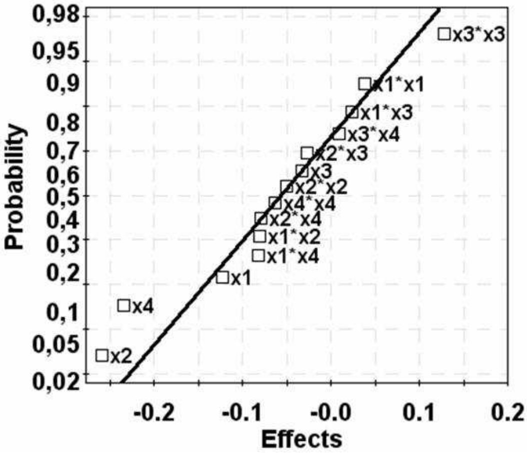

Figure 2. Normal probability plot of effects.

However, removing one by one the terms of the screening model in order of their insignificance it was found that the relative humidity (x_3) becomes significant as listed in Table 4. All the terms left in the model are significant at 99% confidence level excepting the interaction between temperature and time (x_2*x_4) that is significant at 95% confidence level.

After removing the insignificant terms of the screening model, runs number 1 and 18 were also removed due to their high residual values. Thus, the p-values of the remained coefficients became lower stressing their statistical significance, and goodness of fit was much improved as shown in Table 5.

Table 4. Estimates (95% confidence level) of the RSM model regression for packed-bed adsorption efficiency.

Real variables	Term	Estimate	Standard Error	p-value	Confidence interval (±)
Constant	Intercept	0.733285	0.014807	$2.79499 \cdot 10^{-14}$	0.03259
Flow rate (M_v)	x_1	-0.068246	0.006995	$9.45817 \cdot 10^{-7}$	0.01539
Temperature (T)	x_2	-0.131912	0.007338	$1.67252 \cdot 10^{-9}$	0.01615
Relative humidity (u)	x_3	-0.030803	0.007207	$1.31195 \cdot 10^{-3}$	0.01586
Time (t)	x_4	-0.126896	0.007004	$1.53964 \cdot 10^{-9}$	0.01541
u * u	x_3^2	0.068263	0.016960	$1.99944 \cdot 10^{-3}$	0.03733
M_v * T	$x_1 * x_2$	-0.032883	0.007888	$1.56534 \cdot 10^{-3}$	0.01736
M_v * t	$x_1 * x_4$	-0.043390	0.007690	$1.50559 \cdot 10^{-4}$	0.01693
T * t	$x_2 * x_4$	-0.023773	0.008272	$1.51367 \cdot 10^{-2}$	0.01821

The final regression model in terms of coded factors is presented as follows:

$$\begin{aligned}\hat{Y} &= 0.733285 - 0.068246 \cdot x_1 - 0.131912 \cdot x_2 - 0.030803 \cdot x_3 - \\ &- 0.126896 \cdot x_4 - 0.032883 \cdot x_1 \cdot x_2 - 0.04339 \cdot x_1 \cdot x_4 - \\ &- 0.023773 \cdot x_2 \cdot x_4 + 0.068263 \cdot x_3^2\end{aligned} \tag{3}$$

In terms of actual factors, the packed-bed adsorption efficiency is expressed by the following regression equation:

$$\begin{aligned}\hat{Y} &= 1.56311 + 0.296634 \cdot M_v - 0.00057486 \cdot T - 0.0182241 \cdot u + \\ &+ 0.00145229 \cdot t - 0.0121791 \cdot M_v \cdot T - 0.00262967 \cdot M_v \cdot t - \\ &- 0.000048 \cdot T \cdot t + 0.000134841 \cdot u^2\end{aligned} \tag{4}$$

subjected to $0.6 \le M_v \le 1.2$ [$m^3\ h^{-1}$]; $20 \le T \le 38$ [°C]; $40 \le u \le 85$ [%] and $10 \le t \le 120$ [min.].

Table 5. Analysis of variance (ANOVA) for the response surface modeling.*

Source of variation	Degrees of freedom	Sum of Squares	Mean Square (Variance)	F-ratio	p-value	Standard Deviation
Total	20	12.2473	0.61236			
Constant	1	11.2176	11.21760			
Regression	8	1.0214	0.12768	169.19[a]	0.000	0.3573
Residual	11	0.0083	0.00075			0.0275
Lack of Fit (model error)	9	0.0082	0.00091	15.1085[b]	0.064	0.0301
Pure Error (replicate error)	2	0.0001	0.00006			0.0776
Total corrected	19	1.0297	0.05419			0.2328

* $R^2 = 0.9919$; $R^2_{adj} = 0.9861$; $Q^2 = 0.9645$.

[a] F-ratio (regression/residual); $F_{(0.1,\ 8,\ 11)} = 2.295$; $F_{(0.05,\ 8,\ 11)} = 2.935$; $F_{(0.01,\ 8,\ 11)} = 4.275$;

[b] F-ratio (lack of fit/pure error); $F_{(0.1,\ 9,\ 2)} = 59.9$; $F_{(0.05,\ 9,\ 2)} = 241$; $F_{(0.01,\ 9,\ 2)} = 6022$.

After performing the screening step and removing the insignificant coefficients, the determination coefficient (R^2), adjusted-R^2 and especially goodness of prediction (Q^2) underwent an obvious improvement. Considering that R^2 gives overestimation and Q^2 gives underestimation of the goodness of fit and for a model to be acceptable both values should be as close to *1* as possible and ideally not separated by more than 0.3 ($R^2-Q^2<0.3$) [16]. The *F*-test revealed that RSM regression is statistically significant at a confidence level of 99%. According to the analysis of variance the *F*-value of the model (regression) (*Fmodel = 169.19*) was much higher than the tabular *F*-value with the same number of degrees of freedom of two sources of variance ($F_{(0.01,8,11)} = 4.275$), indicating that the differences are highly significant. The *P*-value for lack of fit was *0.064*, indicating that the probability of error for the lack of fit was higher than *0.05* and the model represents the actual relationships of parameters well within the range selected. This is also evident from the fact that the observed and predicted values of the response are very close to each other (Figure 3), clearly indicating that the prediction of experimental data is extremely accurate.

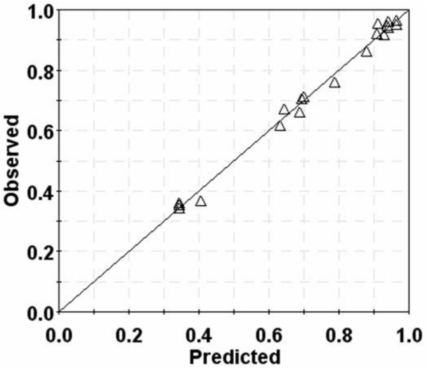

Figure 3. Observed vs. predicted values of the response.

Response surfaces were plotted using MODDE software to emphasize the effects of the significant parameters and their interactions on gas drying. Contour plots, as presented in Figure 4, are very useful to see interaction effects of the significant factors on the responses. These types of plots show effects of two factors on the response at a time. In all the presented figures, the other one factor was kept at the intermediary level.

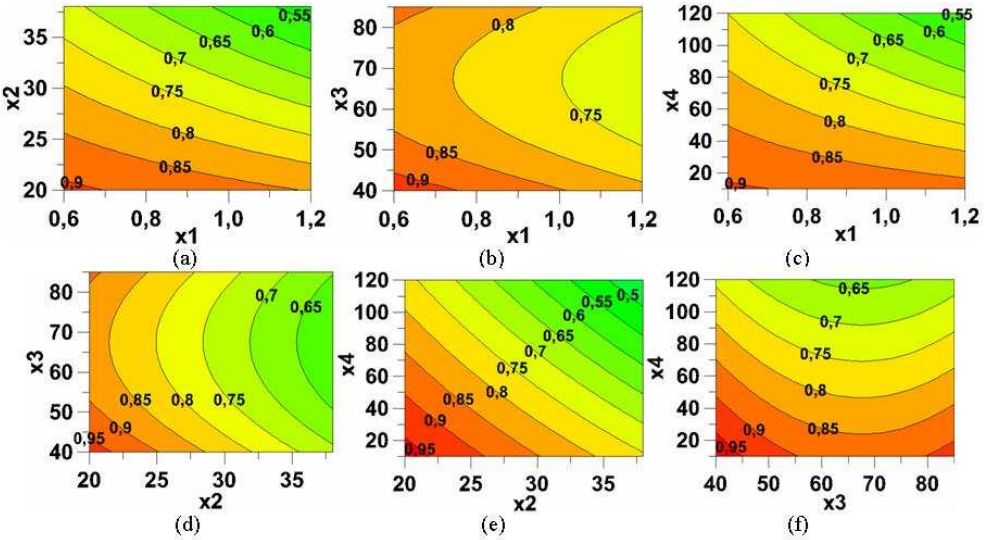

Figure 4. Contour plots of the packed-bed adsorption efficiency as function of (a) flow rate and temperature at an air relative humidity of 60% and 60 min.; (b) flow rate and drying time at 27 ℃ and 60 min; (c) flow rate and drying time at 27 ℃ and 60% air relative humidity; (d) temperature and relative humidity at 0.9 $m^3 \cdot h^{-1}$ and 60 min.; (e) temperature and drying time at 0.9 $m^3 \cdot h^{-1}$ and 60% air relative humidity; (f) air relative humidity and drying time at 0.9 $m^3 \cdot h^{-1}$ and 27 ℃.

As can be seen an increase of the flow rate and/or temperature leads to a diminishing of the fixed-bed adsorption efficiency. Figs. 4c and 4e emphasize the stronger effect of temperature as a function of time compared to the effect of air flow rate. Though the combined effects of air relative humidity and any of the other effects seem to pinpoint a minimum point near the investigated range, one should take into consideration that these interactions have no statistical significance.

To validate the suggested model, confirmatory experiments were carried out. Verification experiments indicate the validity and adequacy of the predicted models (Figure 5).

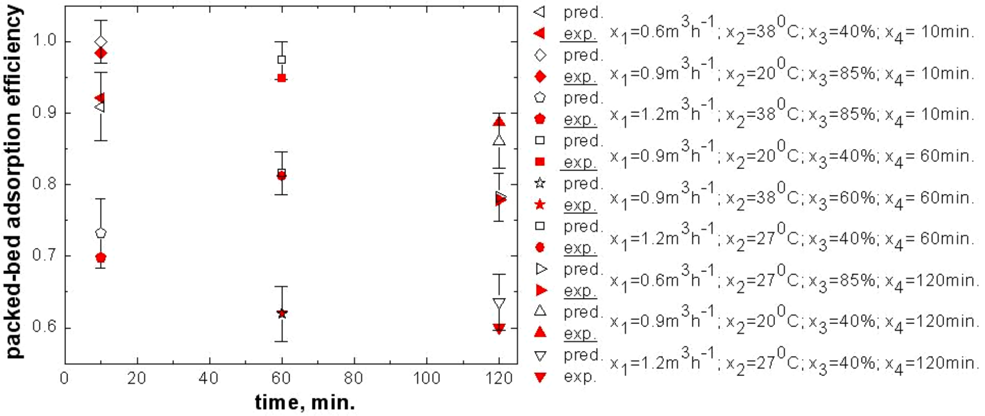

Figure 5. Model validation.

As can be seen, all the considered verification experiments (filled symbols) are placed within the confidence interval of the values predicted (open symbols) by the suggested model.

MODDE software allows one to minimize or maximize the objective function within the investigated ranges of the considered factors. Nevertheless, it was of interest to find the maximum value (Table 6) of packed-bed adsorption efficiency at the longest investigated drying time (120 min.). Beside the predicted value, the experimental one is presented in the table.

Table 6. Optimal conditions of the packed-bed adsorption efficiency at 120 min.*

x_1^*	M_v^*, m^3·h^{-1}	x_2^*	T^*, °C	x_3^*	u^*, %	Y*, Experimental	Y*, Predicted
-1	0.6	-1	20	-1	40	0,9405	0.9399

* Maximum predicted value within the investigated ranges of the considered factors, at the longest drying time.

CONCLUSIONS

In this work is presented the screening and response surface modeling of gas drying by adsorption in packed bed of silica gel using D-optimal design at three levels for four factors.

The use of an experimental design permitted the rapid screening of a large experimental domain for gas drying by adsorption in fixed bed of silica gel. Thus, it was emphasized the order of influence of the four factors considered pinpointing the strong influence over the packed-bed adsorption efficiency of the temperature factor.

The experimental and the predicted values were very close which reflected the correctness and the applicability of RSM. In this case, the value of the determination coefficient (R^2 = 0.9919) indicated that near about negligible of total variations were not explained by the model. The value of the adjusted determination coefficient (adjusted R^2 = 0.9861) was near to 1, showing a high significance of the model.

EXPERIMENTAL SECTION

Experimental Technique

In the experimental investigations was used a laboratory installation consisting in an adsorption column, a wetting air column, a ventilating fan and devices for measuring and controlling temperature and air flow rate. A full description of the experimental installation employed to obtain the data needed in this study can be found in our previous work [15].

The investigations were carried out using as adsorbent material purchased-spherical silica gel grains having a diameter of $2.57 \cdot 10^{-3}$ *m*. Experimental investigations were performed under atmospheric pressure at three initial values of air temperature (*20*, *27* and *38°C*), using wet air as gaseous phase at three values of the air relative humidity (*40*, *60* and *85 %*), and at three values of air flow rate: *0.6*, *0.9* and $1.2\ m^3 \cdot h^{-1}$. Air relative humidity was measured at the input and output of the fixed bed by using a Testo 625 psyhrometer.

The adsorption process was achieved in fixed granular bed of composite materials under dynamic regime and non-isothermal and non-adiabatic conditions. The geometrical parameters of the fixed adsorbent bed were *0.15 m* in height and $2.95 \cdot 10^{-2}$ *m* in diameter.

Experimental Design

A D-optimal experimental design at three levels for four factors was used for screening and response surface modeling (RSM) of gas drying by adsorption in fixed bed of ordered silica gel grains. Screening and RSM were employed to analyze the operating conditions of air flow rate, temperature, relative humidity and drying time. The software of MODDE (Unimetrics, Demo Version 8.02) [16] was used to design and regress the experimental data.

The operating ranges and the levels of the independent variables considered in this study are given in Table 7. For the statistical calculations, the natural variables (denoted as z_i) are converted into dimensionless codified values (x_i) to allow comparison of factors of different natures with different units and to decrease the error in the polynomial fit. This is done using the following relationship:

$$x_i = \frac{z_i - z_i^0}{\Delta z_i}\text{; } i = 1, 2, 3, 4 \qquad (5)$$

where z_i^0 refers to the value of variable *i* in the centre of the domain (i.e., it corresponds to $x_i = 0$) and Δz_i corresponds to the difference of that variable between the maximum level and the centre of the domain.

Table 7. Predictor variables and their coded levels and actual values used in the experimental design.

Source of variation	Symbol	Inferior level	Intermediary level	Superior level
Flow rate, m^3/h	x_1	-1	0	+1
	z_1	0.6	0.9	1.2
Temperature, K	x_2	-1	-0.222	+1
	z_2	20	27	38
Air relative humidity, %	x_3	-1	-0.111	+1
	z_3	40	60	85
Drying time, min.	x_4	-1	-0.0909	+1
	z_4	10	60	120

ACKNOWLEDGMENTS

Financial support for this work was provided by THE NATIONAL UNIVERSITY RESEARCH COUNCIL, Romanian Ministry of Education, Research and Innovation, in the framework of PN-II/IDEI PROGRAM (PN-II-ID-PCE-2007-1**,** Grant No. 63/01.10.2007, Cod 608).

REFERENCES

1. A. Gupta, V. Gaur, N. Verna, *Chem. Eng. Proc*., **2004**, *43*, 9.
2. S.A. Gadre, Ritter, J.A., *Ind. Eng. Chem. Res*., **2002**, *41*, 4353.
3. A. Georgian, K. Kupiec, *Chem. Eng. J.,* **2003**, *92*, 185.
4. A. Goergion, *Chem. Eng. Sci*., **2004**, *59*, 3591.
5. S. Walton, M. Le Van, *Ind. Eng. Chem. Res.*, **2005**, *44*, 7474.
6. K.S. Hwang, J.J. Ho, L.W. Kook, *Chem. Eng. Sci*., **1995**, *50*, 813.
7. K.S. Hwang, C.D. Ki, G.S. Yong, C.S. Yong, *Chem. Eng. Sci*, **1997**, *52*, 1111.
8. G. Jinescu, V. Lavric, C. Iordache, “Mathematical model of bulk separation of gas mixtures by pressure swing adsorption”, 14th Int. Congress Chem. Process Eng. Chisa, Praga, **2000**.
9. J. Delgado, M.A. Uguina, J.L. Sotelo, B. Ruiz, *Separation and Purification Technology*, **2006**, *50*, 192.

10. S. Akhnazarova, V. Kafarov, “Experiment Optimization in Chemistry and Chemical Engineering”, Mir Press, Moscow, **1982**.
11. R.H. Myer, D.C. Montgomery, “Response Surface Methodology”, Wiley, United States, **2002**.
12. R.D. Cook, C.J. Nachtsheim, *Technometrics*, **1980**, *22*, 315.
13. W. DuMouchel, B. Jones, *Technometrics*, **1994**, *36*, 37.
14. L. Eriksson, E. Johansson, N. Kettaneh-Wold, C. Wikström, S. Wold, “Design of experiments, principals and applications”: Umetrics AB, Learnways AB; Stockholm, **2000**.
15. S. Petrescu, L.D. Horoba, I.G. Galben, M.S. Secula, *Rev. Chim*, **2009**, *60*, 18.
16. MODDE 8.02, Umetrics, Box 7960, S-90719 Umea, Sweden. Available from www.umetrics.com.

STUDIA UNIVERSITATIS BABEŞ-BOLYAI, CHEMIA, LIV, 2, 2009

COUNTING NUMBERS OF PERMUTATIONAL ISOMERS OF AN INFINITE FAMILY OF FULLERENES

MARYAM JALALI AND MODJTABA GHORBANI[a]

ABSTRACT. Hetero-fullerenes are fullerene molecules in which one or more carbon atoms are replaced by hetero-atoms such as boron or nitrogen, whose formation is a kind of “on-ball” doping of the fullerene cage. In this paper, the numbers of all $C_{40n-k}X_k$ hetero-fullerenes are computed, where C_{40n} is an infinite family of fullerenes. We apply the computer algebra system GAP to compute the number of permutational isomers of hetero-fullerenes of the C_{80} fullerene with D_{20} point group symmetry.

Keywords: *Fullerene, Hetero-fullerene, Cycle Index, Permutation Group.*

INTRODUCTION

Carbon exists in several allotropic forms in nature. Fullerenes are zero-dimensional nanostructures, discovered experimentally in 1985 [1]. Fullerenes are carbon-cage molecules in which a number of carbon atoms are bonded in a nearly spherical configuration. Let p, h, n and m be the number of pentagons, hexagons, carbon atoms and bonds between them, in a given fullerene F. Since each atom lies in exactly 3 faces and each edge lies in 2 faces, the number of atoms is $n = (5p+6h)/3$, the number of edges is $m = (5p+6h)/2 = 3/2n$ and the number of faces is $f = p + h$. By the Euler’s formula $n - m + f = 2$, one can deduce that $(5p+6h)/3 – (5p+6h)/2 + p + h = 2$, and therefore $p = 12$, $n = 2h + 20$ and $m = 3h + 30$. This implies that such molecules, made entirely of n carbon atoms, have 12 pentagonal and (n/2 – 10) hexagonal faces, while $n \neq 22$ is a natural number equal or greater than 20 [2]. Hetero-fullerenes are fullerene molecules in which one or more carbon atoms are replaced by heteroatoms such as boron or nitrogen, whose formation is a kind of “on-ball” doping of the fullerene cage.

Enumerating molecules is a mind-boggling problem that has fascinated chemists and mathematicians alike for more than a century. Some of the solutions developed were not only valuable to chemists but to mathematicians as well. Indeed, while trying to solve the problem of counting the isomers of

---

[a] *Institute of Nanoscience and Nanotechnology, University of Kashan, Kashan 87317-51167, I. R. Iran, Ghorbani@kashanu.ac.ir*

substituted aromatic compounds, important concepts in graph theory and combinatorics were developed. The terms graph and tree were even coined in a chemistry context. Historically, molecular enumeration has brought a fertile ground of research between Chemistry, Mathematics, and Computer Science. Still today, new concepts and techniques are being developed at the interface of these fields [3].

Detecting symmetry of molecules is a well-studied problem with applications in a large number of areas. Randić [4] and then Balasubramanian [5-7] considered the Euclidean matrix of a chemical graph to find its symmetry. Here the Euclidean matrix of a molecular graph G is a matrix $D(G) = [d_{i,j}]$, where for $i \neq j$, d_{ij} is the Euclidean distance between the nuclei i and j; in this matrix d_{ii} are zero.

Suppose σ is a permutation on n atoms of the molecule under consideration. Then the permutation matrix P_σ is defines as $P_\sigma = [x_{ij}]$, where $x_{ij} = 1$ if $i = \sigma(j)$ and 0 otherwise. It is easy to see that $P_\sigma P\tau = P_{\sigma\tau}$, for any two permutations σ and τ on n objects, and so the set of all n × n permutation matrices is a group isomorphic to the symmetric group S_n on n symbols. It is a well-known fact that a permutation σ of the vertices of a graph G belongs to its automorphism group if it satisfies $P_\sigma^t A P_\sigma = A$, where A is the adjacency matrix of G. On the other hand, it is a well-known fact that for computing the symmetry of a molecule, it is sufficient to solve the matrix equation $P^t E P = E$, where E is the Euclidean matrix of the molecule under consideration and P varies on the set of all permutation matrices with the same dimension as E.

Ashrafi et al. [8-12] introduced some algorithms for computing the symmetry of molecules and applied them to compute the symmetry of some big fullerenes. We note that, to compute the number of isomers of a given fullerene, we need an efficient method for computing symmetry of fullerenes. Fripertinger [13] computed the symmetry of some fullerenes and then applied SYMMETRICA [14] to calculate the number of $C_{60}H_kCl_{60-k}$ molecules.

In this paper we extend our investigation on isomerism of hetero-fullerenes to $C_{40n-k}X_k$ [15]. Throughout this paper, the notation is standard and taken mainly from the standard books of Graph Theory.

RESULTS AND DISCUSSION

Groups are often used to describe the symmetry of objects. This is formalized by the notion of a *group action*. Let G be a group and X a nonempty set. An *action* of G on X is denoted by G_X and X is called a G-set. It induces a group homomorphism φ from G into the symmetric group S_X on X, where $\varphi(g)x = gx$ for all $x \in X$. The orbit of x will be indicated as x^G and defined as the set of all $\varphi(g)x$, $g \in G$. The set of all G-orbits will be denoted by $G\backslash\backslash X := \{x^G \mid x \in X\}$. Suppose g is a permutation of n symbols with exactly $\lambda1$ orbits of size 1, $\lambda2$ orbits of size 2, …, and λn orbits of size n. Then the cyclic type of g is defined as $1^{\lambda1}\, 2^{\lambda2} \ldots n^{\lambda n}$.

Enumeration of chemical isomers can be accomplished by various methods. The Polya-Redfield theorem[16] is a standard method for combinatorial enumeration of graphs, polyhedra, chemical isomers, etc.

Denote by $C_{m,n}$ the set of all functions $f:\{1,2,..,m\}\rightarrow\{x_1,x_2,..,x_n\}$. The action of $p\in S_m$ induced on $C_{m,n}$ is defined by $\hat{p}(f) = fop^{-1},\ f \in C_{m,n}$. Treating the colors $x_1,x_2,..,x_n$ that comprise the range of $f\in C_{m,n}$ as independent variables, the weight of *f* is $W(f)=\prod_i f(i)$. Evidently, $W(f)$ is a monomial of (total) degree *m*. Suppose *G* is a permutation group of degree *m*, $\hat{G}=\{\hat{p}: p\in G\}$, $\hat{p}$ being as above. Let $p_1,p_2,\ldots,p_t$ be the distinct orbits of $\hat{G}$. The weight of p_i is the common value of W(f), $f\in p_i$. The sum of the weights of the orbits is the pattern inventory

$$W_G(x_1,x_2,\ldots,x_n)=\sum_{i=1}^{t} w(p_i).$$

Theorem.1 (Pólya's Theorem[16]**)** If G is a subgroup of S_m then the pattern inventory for the orbits of $C_{m,n}$ modulo $\hat{G}$ is

$$W_G(x_1,x_2,\ldots,x_n)=\frac{1}{|G|}\sum_{p\in G} M_1^{C_1(p)} M_2^{C_2(p)} \ldots M_m^{C_m(p)},$$

where $M_k=x_1^k+x_2^k+\ldots+x_n^k$, the kth power is the sum of x's, and $(C_1(p),\ldots,C_m(p))$ is the cycle type of the permutation p.

We now introduce the notion of cycle index. Let G be a permutation group. The cycle index of G acting on X is the polynomial Z(G, X) over Q in terms of indeterminates x_1, x_2, …, x_t, $t = |X|$, defined by $Z(G, X)=\frac{1}{|G|}\sum_{C\in Conj(G)}|C|\prod_{i=1}^{t} x_i^{C_i(g_c)}$, where Conj(G) is the set of all conjugacy classes C of G with representatives $g_C \in C$.

The dihedral group D_n is the symmetry group of an n-sided regular polygon, of n > 1. These groups are one of the most important classes of finite groups currently applicable in chemistry. One group presentation for D_n is: $\langle x,y \mid x^n = y^2 = e,\ yxy = x^{-1}\rangle$. This means that D_n is generated by a two elements set {x,y} with the condition $x^n = y^2 = e$ and $yxy = x^{-1}$.

In this section, an infinite class $C_{40n}(n \geq 2)$ of fullerene molecules with exactly 40n carbon atoms and symmetry group D_{20} is constructed, as shown in Figure 1. To compute the number of isomers of these fullerenes, we first compute a permutation representation for their symmetry group.

Consider the graph of fullerene C_{40n} (Figure 1). One can see that the generators of this group are as follows:

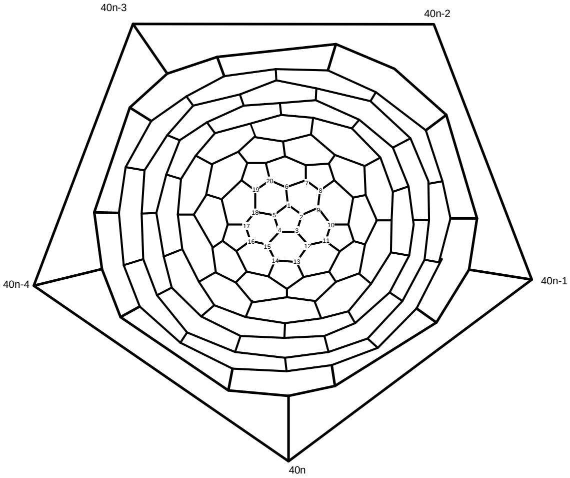

Figure 1. The Schlegel diagram of C_{40n}.

σ=(2,5)(3,4)(7,10)...(10n-10,10n-7)(10n-4,10n-2)(10n-1,10n),

τ=(1,10n-4,3,10n-1,5,10n-3,2,10n,4,10n-2)...(10n-44,10n-36,10n-41,10n-38,10n-43,

10n-39,10n-40,10n-37,10n-42,10n-32).

Since $\sigma^2 = \tau^{10}$ = identity and $\sigma^{-1}\tau\sigma = \tau^{-1}$, the symmetry group G of these fullerenes is isomorphic to the dihedral group of order 20. In Table 1, the cycle types of elements of G are computed.

Table 1. Cycle Types of Elements of C_{40n}.

Fullerene	Cycle type	#Permutations
C_{40n}	1^{40n}	1
	$1^{4n}2^{18n}$	5
	2^{20n}	6
	10^{4n}	4
	5^{8n}	4

Thus the cycle index of G is computed as $Z(G,X) = (x_1^{40n} + 5x_1^{4n}x_2^{18n} + 6x_2^{20n} + 4x_{10}^{4n} + 4x_5^{8n})/20$. From the cycle index one can compute the number of different colourings using k colours via Pólya's theorem by replacing each variable x_i in the cycle index by $1 + x^i$.

In what follows we present a GAP program [17] to compute the number of hetero-fullerenes for $C_{40n-k}X_k$, $n \geq$.

A Gap Program for Counting the Number of Hetero fullerenes for C_{40n} (n≥2)

```
f:=function(n)
            local s,i,f,x,t,tt,g;
              Print("Number of vertices is: ",40*n,"\n");
               x:=Indeterminate(Rationals,"x");
f:=((1+x)^(40*n)+5*((1+x)^(4*n))*((1+x^2)^(18*n))+6*((1+x^2)^(20*
                            n))+4*((1+x^(10 ))^(4*n))+4*((1+x^5)^(8*n)))/20;
g:=((1+x)^(40*n)+4*((1+x^5)^(8*n))+5*((1+x^2)^(20*n)))/10;
t:=CoefficientsOfLaurentPolynomial(f);
               tt:=CoefficientsOfLaurentPolynomial(g);
                    Print("\n");
                       Print("\n");
                        Print("Number of Molecules for Symmetry Group =","\n");
                            for i in t[1] do
                              Print(i,"\n");
                           od;
                     Print("Number of  Molecules for Rotation Group=","\n");
                        for i in tt[1] do
                          Print(i,"\n");
                        od;
              return;
         end;
```

For first, we apply this program to compute the number of hetero-fullerenes for the case n=2 (Table 2).

To investigate the efficiency of this program, we consider the fullerene C_{80}, Figure 2.

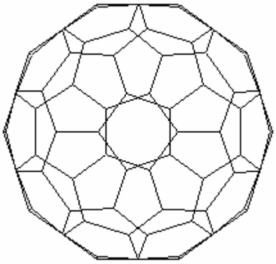

Figure 2. The Fullerene C_{80}

Table 2. Number of $C_{80-k}X_k$ molecules.

k,80-k	Number of $C_{80-k}X_k$ molecules For Symmetry Group	Number of $C_{80-k}X_k$ molecules For Rotational Group
0,80	1	1
1,79	6	8
2,78	186	336
3,77	4194	8216
4,76	79740	158548
5,75	1203782	2404008
6,74	15034806	30054960
7,73	158859426	317671640
8,72	1449480258	2898799410
9,71	11595241522	23190029720
10,70	82325438886	164649540064
11,69	523885533094	1047767706440
12,68	3012337514396	6024666231220
13,67	15756824366962	31513628709080
14,66	75407639879882	150815232429520
15,65	331793540197286	663586981674280
16,64	1347911182335707	2695822151503195
17,63	5074488888801112	10148977366779680
18,62	17760710869067496	35521420920448320
19,61	57956003064041544	115912004662694240
20,60	176765808675933576	353531614645048424
21,59	505045165439887512	1010090326346335520
22,58	1354439305721598168	2708878603630164160
23,57	3415542591867172296	6831085171456838240
24,56	8111913652414445976	16223827285003417560
25,55	18170686570736722680	36341373112150381184
26,54	38437990816963861368	76875981589411644864
27,53	76875981614459748280	153751963166790066848
28,52	145515250904543680112	291030501720170377168
29,51	260923898142211496104	521847796167085497824
30,50	443570626831407097544	887141253504158022032
31,49	715436494844336235640	1430872989490395719840
32,48	1095512132721165787070	2191024265188594496830
33,47	1593472192991913171700	3186944385683154103280
34,46	2202740972661988424780	4405481944959314508640
35,45	2895030992577728759340	5790061984745360652720
36,44	3618788740730127897800	7237577480988390941080
37,43	4303424448373513070740	8606848896243103666160
38,42	4869664507392977231060	9739329014235469036960
39,41	5244254084832211801660	10488508169105968435280
40,40	5375360436990996540520	10750720873402540915720

We now apply the above presented cycle index to compute the number of permutational isomers of fullerenes under consideration (Table 3).

Table 3: Number of $C_{120-k}X_k$ molecules.

k,120-k	Number of $C_{120-k}X_k$ molecules For Symmetry Group	Number of $C_{120-k}X_k$ molecules For Rotational Group
0,120	1	1
1,119	9	12
2,118	405	744
3,117	14259	28084
4,116	412632	822342
5,115	9536367	19057812
6,114	182684265	365291656
7,113	2974542453	5948756892
8,112	42013919853	84026434917
9,111	522832240566	1045659267016
10,110	5803419985974	11606820594744
11,109	58034121398226	116068178638776
12,108	527143096685568	1054285981000812
13,107	4379341982282658	8758683326510712
14,106	33470683765816230	66941365617149616
15,105	236526160473589102	473052315663260312
16,104	1552202918686129347	3104405822819450907
17,103	9495829590389193519	18991659143539682964
18,102	54337247045227281915	108674493995424201624
19, 101	291705220818253169109	583410441409438331052
20,100	1473111364848094865916	2946222729155360589846
21,99	7014816022315509542745	14029632043417445580060
22,98	31566672099131635416015	63133344195549855172920
23,97	134501472419113302461595	269002944832482326122020
24,96	543610117688714575771545	1087220235365315747498985
25,95	2087462851912205617786356	4174925703800125701430752
26,94	7627268112737303829404844	15254536225426119648417888
27,93	26554192688746406631677828	53108385377400459421117936
28,92	88197854287560528641843328	176395708574945913169466616
29,91	279800089463852439888710724	559600178927387106905277168
30,90	848726938040170729207289484	1697453876079767487990657608
31,89	2464045949148508100000172492	4928091898296021941456150544
32,88	6853127796068800101072021819	13706255592135885828862845963
33,87	18275007456182501794269299289	36550014912362162732466449868
34,86	46762519079054030050374396597	93525038158103374720385845224
35,85	114902189737101913734873735291	229804379474196387869171548452
36,84	271296836879265733970689673432	542593673758519711650326477494
37,83	615917143185355131079975284759	1231834286370692349388801702308
38,82	1345292707483796525793076573689	2690585414967565890802955326728
39,81	2828564154196690639872133979477	5657128308393341518178262068764
40,80	5727842412248288296445487967359	11455684824496518670233233886183
41,79	11176277877557617924542986567514	22352555755115154291338498905848
42,78	21022046483977406618721800434458	42044092967954698968798134423376
43,77	38133014552331079868756610116958	76266029104662004841211423177096
44,76	66732775466579362235864741865984	133465550933158515549260065296468
45,75	112704243010222876917676943647006	225408486020445480975135984579752
46,74	183756917951450303496185554644330	367513835902900252412996619222480
47,73	289319402732070625508986408033290	578638805464140804538392558517560
48,72	440006591655024025482027159608535	880013183310047491594999090498335
49,71	646540297942076034597277958373255	1293080595884151389733754799136180
50,70	918087223077747910273484362873443	1836174446155494999379650802722024
51,69	1260119717949849972898410419576157	2520239435899698983128141706551692
52,68	1672081933433454711928110241702728	3344163866866908301016963593337634
53,67	2145312669310847447636010877139601	4290625338621693624396676664419644
54,66	2661776830441236597146467544097383	5323553660882471763161240697200632
55,65	3194132196529483813659635751641043	6388264393058966062990607479134372
56,64	3707474870971722252390899898299397	7414949741943442803545499299939301
57,63	4162778802494565249939680394539240	8325557604989128703646906989049312
58,62	4521639044088924319727997397894440	9043278088177846752565403398800192
59,61	4751552893788361090371095093480184	9503105787576720256120636674233376
60,60	4830745442018167136321641186395224	9661490884036332319521604735649640

CONCLUSIONS

Hetero-fullerenes or fullerene molecules in which one or more carbon atoms are replaced by hetero-atoms such as boron or nitrogen, can be enumerated by applying the Polya's theorem. In this paper, the numbers of all $C_{40n-k}X_k$ hetero-fullerenes were computed, C_{40n} being an infinite family of fullerenes. In this respect, we applied the computer algebra system GAP to compute the number of permutational isomers of hetero-fullerenes of the C_{80} fullerene with D_{20} point group symmetry.

REFERENCES

1. H.W. Kroto, J.R. Heath, S.C. O'Brien, R.F. Curl and R.E. Smalley, *Nature*, **1985**, *318, 162.*
2. P.W. Fowler and D.E. Manolopoulos, "An Atlas of Fullerenes", Oxford Univ. Press, Oxford, **1995**.
3. S. Fujita, "Symmetry and Combinatorial Enumeration in Chemistry", Springer Verlag, Berlin, **1991**.
4. M. Randić, *J. Chem. Phys,* **1974,** *60, 3920.*
5. K. Balasubramanian, *J. Chem. Phys,* **1980***, 72, 665.*
6. K. Balasubramanian, *Int. J. Quantum Chem,* **1982***, 21, 411*.
7. K. Balasubramanian, *Chem. Rev,* **1985**, *85, 599.*
8. A. R. Ashrafi, M. Ghorbani, *MATCH Commun. Math. Comput. Chem.,* **2008**, *60, 359.*
9. M. Ghorbani and A. R. Ashrafi, *J. Comput. Theor. Nanosci.,* **2006**, *3, 803.*
10. A.R. Ashrafi, M. Ghorbani and M. Jalali, *Digest Journal of Nanomaterials and Biostructures,* **2008**, *3(4), 245.*
11. M. Ghorbani, and M. Jalali, *Digest Journal of Nanomaterials and Biostructures,* **2008**, *3(4), 269.*
12. A. R. Ashrafi, M. Jalali, M. Ghorbani and M. V. Diudea, *MATCH Commun. Math. Comput. Chem,* **2008**, *60(3), 905.*
13. H. Fripertinger, *MATCH Commun. Math. Comput. Chem,* **1996**, *33, 121.*
14. SYMMETRICA, A program system devoted to representation theory, invariant theory and combinatorics of finite symmetric groups and related classes of groups, Copyright by "Lehrstuhl II für Mathematik, Universität Bayreuth, 95440 Bayreuth". Distributed via anonymous ftp 132.180.16.20 in dist/SYM.tar.Z.
15. M. Ghorbani and M. Jalali, *Digest Journal of Nanomaterials and Biostructures,* **2008**, *3(4), 269.*
16. G. Pólya, R. C. Read, "Combinatorial Enumeration of Groups and Chemical compounds, Springer, New York", **1987**.
17. The GAP Team, GAP, Groups, Algorithms and Programming, Department of Mathematics, RWTH Aachen, **1995**.